

**Electrochemistry of Tris(tetrachlorocatecholate) Complexes
of Manganese, Iron, and Cobalt**

by

Kristin Alexis Boles

B.S., Cornell University, 2006

A thesis submitted to the
Faculty of the Graduate School of the
University of Colorado in partial fulfillment
of the requirements for the degree of
Doctor of Philosophy
Department of Chemistry

2014

This thesis entitled:
Electrochemistry of Tris(tetrachlorocatecholate) Complexes of Manganese, Iron, and Cobalt
written by Kristin Alexis Boles
has been approved for the Department of Chemistry

Cortlandt G. Pierpont

Wei Zhang

Date _____

The final copy of this thesis has been examined by the signatories, and we find that both the content and the form meet acceptable presentation standards of scholarly work in the above mentioned discipline.

Boles, Kristin Alexis (Ph.D., Chemistry)

Electrochemistry of Tris(tetrachlorocatecholate) Complexes of Manganese, Iron, and Cobalt

Thesis directed by Professor Cortlandt G. Pierpont

Homoleptic first-row transition metal complexes of tetrachloroquinones have been synthesized and characterized. These complexes show unique electrochemical properties, as they have the ability to undergo ligand-based redox chemistry. Mononuclear, tris(tetrachlorocatecholate) complexes of chromium and vanadium have previously been prepared and are well-characterized. Here, the first-row transition metal series is completed by synthesizing and characterizing the manganese, iron, and cobalt analogs.

Synthesis of the tris(tetrachlorocatecholato)manganese(IV) dianion, $[\text{Mn}(\text{Cl}_4\text{Cat})_3]^{2-}$, has previously been described. A synthesis for the mixed-valence bis(tetrachlorocatecholato)tetrachlorosemiquinonacobalt(III) dianion, $[\text{Co}(\text{Cl}_4\text{Cat})_2(\text{Cl}_4\text{SQ})]^{2-}$, is presented, as well as syntheses for tris(tetrachlorosemiquinonato)iron(III), $\text{Fe}(\text{Cl}_4\text{SQ})_3$, and tris(tetrachlorocatecholato)iron(III) trianion, $[\text{Fe}(\text{Cl}_4\text{Cat})_3]^{3-}$. These complexes have been characterized with spectroscopy, X-ray crystallography, and magnetic susceptibility measurements. These confirm mononuclear, homoleptic complexes of Mn^{IV} , *hs*- Fe^{III} , and *ls*- Co^{III} .

These complexes undergo ligand-based redox chemistry, which has been studied using cyclic voltammetry and differential pulse voltammetry. The separation in potential between the ligand-based redox couples has been used to gauge the degree of interligand electron coupling through the metal center, which acts as a bridge for electron transfer. The dianion manganese complex, $[\text{Mn}(\text{Cl}_4\text{Cat})_3]^{2-}$, has complicated electrochemical behavior, with strong solvent dependence. The neutral iron complex $\text{Fe}(\text{Cl}_4\text{SQ})_3$ and the trianion complex $[\text{Fe}(\text{Cl}_4\text{Cat})_3]^{3-}$ have the same electrochemistry, which occurs over a narrow potential range. The iron complexes have unique electrochemical properties, as three distinct oxidation peaks are observed, but only one broad reduction peak at scan rates greater than 10 mV/s, which resolves into three peaks at slower scan

rates. This is observed in multiple solvents. The iron complex redox series, $\text{Fe}^{\text{III}}(\text{Cl}_4\text{SQ})_3 \rightleftharpoons [\text{Fe}^{\text{III}}(\text{Cl}_4\text{Cat})(\text{Cl}_4\text{SQ})_2]^- \rightleftharpoons [\text{Fe}^{\text{III}}(\text{Cl}_4\text{Cat})_2(\text{Cl}_4\text{SQ})]^{2-} \rightleftharpoons [\text{Fe}^{\text{III}}(\text{Cl}_4\text{Cat})_3]^{3-}$, has been characterized using spectroelectrochemistry. The dianion cobalt complex, $[\text{Co}(\text{Cl}_4\text{Cat})_2(\text{Cl}_4\text{SQ})]^{2-}$, is unusual in that it is synthesized as a mixed-valence compound, with ligands in different oxidation states. Cyclic voltammetry of this complex shows two reversible one-electron couples at nearly the same potential, which have been resolved using differential pulse voltammetry.

Acknowledgements

Thanks to Joseph Kelly, Nathan Hawkey, and Paul Nelson for their work on the iron complex.

Contents

Chapter

1	Introduction	1
2	Experimental Section	11
2.1	Instrumentation and Methods	11
2.1.1	Cyclic Voltammetry and Differential Pulse Voltammetry	11
2.1.2	Fourier Transform Infrared Spectroscopy	12
2.1.3	UV-Vis Spectroscopy	12
2.1.4	Near-IR Spectroscopy	12
2.1.5	Nuclear Magnetic Resonance Spectroscopy	12
2.1.6	Magnetic Susceptibility	13
2.1.7	Mössbauer Spectroscopy	13
2.2	Reagents and Solvents	13
2.3	Preparation of complexes	15
2.3.1	Preparation of Bis(tetrachlorocatecholato)tetrachloro-1,2-semiquinonatecobalt(III) Dianion	15
2.3.2	Preparation of Tris(tetrachlorocatecholato)manganese(IV) Dianion	16
2.3.3	Preparation of Tris(tetrachloro-1,2-semiquinonato)iron(III)	16
2.3.4	Preparation of Tris(tetrachlorocatecholato)iron(III) Trianion	16

3	Results and Discussion	18
3.1	Characterization of Complexes	18
3.1.1	Preparation of Complexes	18
3.1.2	X-Ray Crystallography	20
3.1.3	Magnetic Properties	28
3.1.4	Spectroscopy	30
3.2	Electrochemistry of Complexes	38
3.2.1	Cyclic Voltammetry of $(\text{Pr}_4\text{N})_2[\text{Mn}(\text{Cl}_4\text{Cat})_3]$	38
3.2.2	Differential Pulse Voltammetry of $[\text{Mn}(\text{Cl}_4\text{Cat})_3]^{2-}$	44
3.2.3	Cyclic voltammetry of $[\text{Fe}(\text{Cl}_4\text{Cat})_3]^{3-}$	49
3.2.4	Differential pulse voltammetry of $[\text{Fe}(\text{Cl}_4\text{Cat})_3]^{3-}$	53
3.2.5	Cyclic Voltammetry of $[\text{Co}(\text{Cl}_4\text{Cat})_2(\text{Cl}_4\text{SQ})]^{2-}$	59
3.2.6	Differential Pulse Voltammetry of $[\text{Co}(\text{Cl}_4\text{Cat})_2(\text{Cl}_4\text{SQ})]^{2-}$	66
3.2.7	Comparison of Electrochemical Behavior	68
4	Conclusion	75
	Bibliography	79

Tables

Table

3.1	Selected bond lengths and angles of $(\text{Ph}_4\text{P})_2[\text{Mn}(\text{Cl}_4\text{Cat})_3]$	21
3.2	Average bond lengths (\AA) for iron tetrachloroquinone complexes	24
3.3	Selected bond lengths and angles of $(\text{Ph}_4\text{P})_2[\text{Co}(\text{Cl}_4\text{SQ})(\text{Cl}_4\text{Cat})_2]$	25
3.4	$(\text{Pr}_4\text{N})_2[\text{Mn}(\text{Cl}_4\text{Cat})_3]$ cyclic voltammetry peak potentials in DMSO	39
3.5	$(\text{Pr}_4\text{N})_2[\text{Mn}(\text{Cl}_4\text{Cat})_3]$ cyclic voltammetry peak potentials in MeOH	42
3.6	E_p , $\Delta E_{p/2}$, and $E_{1/2}$ from DPV of the iron complex in DMSO	53
3.7	E_p , $\Delta E_{p/2}$, and $E_{1/2}$ from DPV of the iron complex in MeOH	56
3.8	Diffusion coefficients for reduced species calculated from the first oxidation peak, at 25 °C	70

Figures

Figure

1.1	The Creutz-Taube ion	1
1.2	The three redox forms of tetrachloro-1,2-benzoquinone	4
1.3	Cyclic voltammograms for $\text{Cr}(\text{O}_2\text{C}_6\text{H}_2(t\text{-Bu})_2)_3$, $\text{Cr}(\text{phen})_3$, and $\text{Cr}(\text{O}_2\text{C}_6\text{Cl}_4)_3$	6
1.4	Cyclic voltammogram for $(\text{Ph}_4\text{P})_2[\text{V}(\text{Cl}_4\text{Cat})_3]$	6
3.1	X-Ray structure of $[\text{Mn}(\text{Cl}_4\text{Cat})_3]^{2-}$	21
3.2	X-Ray structure of $\text{Fe}(\text{Cl}_4\text{SQ})_3$	22
3.3	X-Ray structure of $(\text{CoCp}_2)_3[\text{Fe}(\text{Cl}_4\text{Cat})_3]$	23
3.4	X-Ray structure of $(\text{Ph}_4\text{P})_2[\text{Co}(\text{Cl}_4\text{SQ})(\text{Cl}_4\text{Cat})_2]$	26
3.5	X-Ray structure of $(\text{Ph}_4\text{P})_2[\text{Co}(\text{Cl}_4\text{SQ})(\text{Cl}_4\text{Cat})_2]$, without counterion	27
3.6	Applied field Mössbauer spectrum of $(\text{Bu}_4\text{N})_3[\text{Fe}(\text{Cl}_4\text{Cat})_3]$	29
3.7	EPR of $(\text{Pr}_4\text{N})_2[\text{Co}(\text{Cl}_4\text{Cat})_2(\text{Cl}_4\text{SQ})]$	30
3.8	UV-Visible spectrum of $(\text{Pr}_4\text{N})_2[\text{Mn}(\text{Cl}_4\text{Cat})_3]$ in MeCN	31
3.9	UV-Visible spectrum of $[\text{Fe}(\text{Cl}_4\text{Cat})_3]^{3-}$, $[\text{Fe}(\text{Cl}_4\text{Cat})_2(\text{Cl}_4\text{SQ})]^{2-}$, and $\text{Fe}(\text{Cl}_4\text{SQ})_3$ in MeCN	33
3.10	UV-Visible spectrum of $[\text{Fe}(\text{Cl}_4\text{Cat})_3]^{3-}$ in MeCN and EtOH	34
3.11	UV-Visible spectrum of $(\text{Pr}_4\text{N})_2[\text{Co}(\text{Cl}_4\text{Cat})_2(\text{Cl}_4\text{SQ})]$ in MeCN	35
3.12	Near-IR spectrum of $(\text{Pr}_4\text{N})_2[\text{Co}(\text{Cl}_4\text{Cat})_2(\text{Cl}_4\text{SQ})]$	37
3.13	Fingerprint region of the cobalt and iron complexes, overlaid	37

3.14	Cyclic voltammograms of $(\text{Pr}_4\text{N})_2[\text{Mn}(\text{Cl}_4\text{Cat})_3]$ in DMSO at several scan rates . . .	39
3.15	Cyclic voltammograms of $(\text{Pr}_4\text{N})_2[\text{Mn}(\text{Cl}_4\text{Cat})_3]$ and $(\text{Pr}_4\text{N})_2[\text{Mn}(\text{Cl}_4\text{Cat})_3]$ with ferrocene in DMSO	41
3.16	Cyclic voltammograms of $(\text{Pr}_4\text{N})_2[\text{Mn}(\text{Cl}_4\text{Cat})_3]$ in DMSO at 5 mV/s and 10 mV/s	41
3.17	Cyclic voltammograms of $(\text{Pr}_4\text{N})_2[\text{Mn}(\text{Cl}_4\text{Cat})_3]$ in MeOH at 10 mV/s, 25 mV/s, and 100 mV/s	43
3.18	Cyclic voltammograms of $(\text{Pr}_4\text{N})_2[\text{Mn}(\text{Cl}_4\text{Cat})_3]$ in MeOH at 10 mV/s	43
3.19	Cyclic voltammograms of $(\text{Pr}_4\text{N})_2[\text{Mn}(\text{Cl}_4\text{Cat})_3]$ in MeOH and DMSO at 10 mV/s .	45
3.20	Differential pulse voltammograms of $(\text{Pr}_4\text{N})_2[\text{Mn}(\text{Cl}_4\text{Cat})_3]$ in DMSO, effective scan rate 100 mV/s	47
3.21	Differential pulse voltammograms of $(\text{Pr}_4\text{N})_2[\text{Mn}(\text{Cl}_4\text{Cat})_3]$ in DMSO, effective scan rate 3 mV/s	48
3.22	Differential pulse voltammograms of $(\text{Pr}_4\text{N})_2[\text{Mn}(\text{Cl}_4\text{Cat})_3]$ in MeOH, effective scan rate 3 mV/s	50
3.23	Cyclic voltammograms of $(\text{Bu}_4\text{N})_3[\text{Fe}(\text{Cl}_4\text{Cat})_3]$ in DMSO at slow scan rates	51
3.24	Cyclic voltammograms of $(\text{Bu}_4\text{N})_3[\text{Fe}(\text{Cl}_4\text{Cat})_3]$ and $(\text{Bu}_4\text{N})_3[\text{Fe}(\text{Cl}_4\text{Cat})_3]$ with ferrocene in DMSO	52
3.25	Cyclic voltammograms of $(\text{Bu}_4\text{N})_3[\text{Fe}(\text{Cl}_4\text{Cat})_3]$ in MeOH at various scan rates . . .	54
3.26	Cyclic voltammograms of $(\text{Bu}_4\text{N})_3[\text{Fe}(\text{Cl}_4\text{Cat})_3]$ in MeOH at 1 mV/s and 5 mV/s . .	54
3.27	Electronic spectra of the $\text{Fe}(\text{Cl}_4\text{SQ})_3$ redox series obtained via spectroelectrochemistry	55
3.28	Differential pulse voltammograms of $(\text{Bu}_4\text{N})_3[\text{Fe}(\text{Cl}_4\text{Cat})_3]$ in DMSO, effective scan rate 20 mV/s	57
3.29	Differential pulse voltammograms of $(\text{Bu}_4\text{N})_3[\text{Fe}(\text{Cl}_4\text{Cat})_3]$ in DMSO, effective scan rate 3 mV/s	58
3.30	Differential pulse voltammograms of $(\text{Bu}_4\text{N})_3[\text{Fe}(\text{Cl}_4\text{Cat})_3]$ in MeOH, effective scan rate 20 mV/s	60

3.31	Differential pulse voltammograms of $(\text{Bu}_4\text{N})_3[\text{Fe}(\text{Cl}_4\text{Cat})_3]$ in MeOH, effective scan rate 3 mV/s	61
3.32	Cyclic voltammograms of $(\text{Pr}_4\text{N})_2[\text{Co}(\text{Cl}_4\text{Cat})_2(\text{Cl}_4\text{SQ})]$ in DMSO at several scan rates	62
3.33	Cyclic voltammogram of $(\text{Pr}_4\text{N})_2[\text{Co}(\text{Cl}_4\text{Cat})_2(\text{Cl}_4\text{SQ})]$ in DMSO at 200 mV/s	62
3.34	Cyclic voltammograms of $(\text{Pr}_4\text{N})_2[\text{Co}(\text{Cl}_4\text{Cat})_2(\text{Cl}_4\text{SQ})]$ with and without ferrocene in DMSO at 10 mV/s	63
3.35	Cyclic voltammograms of $(\text{Pr}_4\text{N})_2[\text{Co}(\text{Cl}_4\text{Cat})_2(\text{Cl}_4\text{SQ})]$ in MeOH at several scan rates	65
3.36	Cyclic voltammograms of $(\text{Pr}_4\text{N})_2[\text{Co}(\text{Cl}_4\text{Cat})_2(\text{Cl}_4\text{SQ})]$ in MeOH and DMSO at 25 mV/s	65
3.37	Differential pulse voltammograms of $(\text{Ph}_4\text{P})_2[\text{Co}(\text{Cl}_4\text{Cat})_2(\text{Cl}_4\text{SQ})]$ in DMSO	67
3.38	Differential pulse voltammograms of $(\text{Pr}_4\text{N})_2[\text{Co}(\text{Cl}_4\text{Cat})_2(\text{Cl}_4\text{SQ})]$ in MeOH	69
3.39	Cyclic voltammograms of $(\text{Bu}_4\text{N})_3[\text{Fe}(\text{Cl}_4\text{Cat})_3]$, $(\text{Pr}_4\text{N})_2[\text{Mn}(\text{Cl}_4\text{Cat})_3]$, and $(\text{Pr}_4\text{N})_2^-[\text{Co}(\text{Cl}_4\text{Cat})_2(\text{Cl}_4\text{SQ})]$ in DMSO at 25 mV/s	71
3.40	Cyclic voltammograms of $(\text{Bu}_4\text{N})_3[\text{Fe}(\text{Cl}_4\text{Cat})_3]$, $(\text{Pr}_4\text{N})_2[\text{Mn}(\text{Cl}_4\text{Cat})_3]$, and $(\text{Pr}_4\text{N})_2^-[\text{Co}(\text{Cl}_4\text{Cat})_2(\text{Cl}_4\text{SQ})]$ in DMSO at 5 mV/s	71
3.41	Cyclic voltammograms of $(\text{Pr}_4\text{N})_2[\text{Mn}(\text{Cl}_4\text{Cat})_3]$, $(\text{Bu}_4\text{N})_3[\text{Fe}(\text{Cl}_4\text{Cat})_3]$, and $(\text{Pr}_4\text{N})_2^-[\text{Co}(\text{Cl}_4\text{Cat})_2(\text{Cl}_4\text{SQ})]$ in DMSO at 5 mV/s	73
3.42	Cyclic voltammograms of $(\text{Pr}_4\text{N})_2[\text{Mn}(\text{Cl}_4\text{Cat})_3]$, $(\text{Bu}_4\text{N})_3[\text{Fe}(\text{Cl}_4\text{Cat})_3]$, and $(\text{Pr}_4\text{N})_2^-[\text{Co}(\text{Cl}_4\text{Cat})_2(\text{Cl}_4\text{SQ})]$ in DMSO at 10 mV/s	73

Chapter 1

Introduction

Transition metal-quinone compounds have been known since 1890, although study of these compounds was not widespread until the 1970s.^{1,2} Since then, many transition metal-quinone complexes have been synthesized and characterized, and they have become an important part of bioinorganic chemistry, as part of the modeling of metal complexes with "non-innocent" ligands.^{3,4} Non-innocent ligands are ligands that may themselves change in oxidation state, while innocent ligands, e.g. halides, are considered to have a fixed oxidation state. In this way, non-innocent ligands behave similarly to transition metals, which also may have multiple oxidation states.

One property of complexes with multiple non-innocent ligands is that they may be mixed-valence. Mixed-valence materials are best known as polymetallic complexes, of which one of the most famous examples is the Creutz-Taube ion (Figure 1.1).⁵



Figure 1.1: The Creutz-Taube ion

The Creutz-Taube ion is a bimetallic complex with two pentaammine ruthenium centers bridged by pyrazine (pz). It has an overall charge of +5, which formally assigns Ru^{II} and Ru^{III} oxidation states, hence mixed-valence, as each ruthenium has a different number of valence electrons. Mixed-valence materials have been studied extensively,⁶⁻¹⁰ especially the electron transfer between

the mixed-valence centers, which for the Creutz-Taube ion is the equilibrium:



The rate of electron transfer depends upon the degree of charge localization, that is, the coupling between the mixed-valence centers. Coupling depends on several factors, including distance between mixed-valence centers and the environment surrounding each center. Robin and Day developed three broad categories describing the degree of interaction between mixed-valence centers.⁶ Class I compounds are described as having localized valences, where there is little or no communication between the mixed-valence centers. Class II compounds have some degree of communication between mixed-valence centers, with an activation energy barrier to electron transfer between the centers. Class III compounds are described as having completely delocalized charge, with no barrier to coupling between mixed-valence centers.

The degree of coupling, H_{ab} , may be analyzed by spectroscopy through an analysis of the intervalence charge transfer (IVCT) band.^{11,12} Class I ($H_{ab} = 0$) and weakly-coupled Class II compounds do not generally have an observed IVCT band, whereas more strongly coupled Class II ($0 < H_{ab} < \lambda/2$) and Class III ($H_{ab} \geq \lambda/2$) compounds have an IVCT band in the near-infrared or visible spectrum. For systems where coupling is very weak, and IVCT transitions are either not observed or too weak to analyze, the comproportionation constant, K_{com} , calculated from the separation between E° of electrochemical couples, may be used to describe coupling strength.¹³

The Creutz-Taube ion generally considered a Class III compound. Essentially, the ion exists as $[(\text{NH}_3)_5\text{Ru}^{\text{II}/2}(\text{pz})\text{Ru}^{\text{III}/2}(\text{NH}_3)_5]^{5+}$, with both ruthenium centers indistinguishable from each other. An IVCT band is observed at 1570 nm, with $\epsilon = 5000 \text{ M}^{-1}\text{cm}^{-1}$ (in water). Substituting other bridging molecules for the pyrazine has allowed researchers to investigate the effect of distance and aromaticity on the electron transfer. For example, with 4,4'-bipyridine as the bridging molecule, $K_{com} = 20$ while using 3,3'-dimethyl-4,4'-bipyridine results in $K_{com} = 9.8$ (both in water).^{7,13} The bridging distance for each of these complexes is the same (11.3 Å), but the additional methyl groups halve the comproportionation constant. In this case, the methyl groups cause the rings

to be perpendicular to each other, inhibiting electron transfer. Simply evaluating bond lengths and distances between redox centers does not necessarily grant insight into the degree of coupling. Furthermore, pinning down the difference between completely-delocalized Class III and partially-delocalized Class II systems is still a challenge, even with modern analytical techniques.^{9,14}

Electrochemical properties of polymetallic clusters, such as oligomers of ferrocene, often include cyclic voltammograms with multiple one-electron couples, the separation of which depends upon the degree of coupling between metal centers.^{15,16} Class I compounds, with completely localized valency, have one-electron couple at the same, or nearly the same, potential. As electron transfer between mixed-valence sites increases towards Class II and Class III regimes, the separation between couples also increases. Transition metal-quinone complexes may exhibit similar behavior, with the couples corresponding to either redox activity on the non-innocent ligands or the metal center. These complexes are unique in that it is the metal center of the complex that acts as the bridge between redox-active ligands, rather than ligands acting as a bridge between metal centers. Some of these complexes exhibit properties desirable in electrocatalysts, with multiple reversible redox couples within a narrow range of potential. These may supply or accept multiple electrons to catalyze redox reactions. One advantage of ligand-based redox chemistry is that it does not rely on oxidative addition/reductive elimination to transfer electrons, so the chemistry it facilitates does not have to be on substances that ligate with the metal. Furthermore, the narrow potential range of the redox couples mitigates the problem of chemically-active intermediates by allowing multiple electrons to be transferred nearly simultaneously.

Another complication of transition metal-quinone electrochemistry is valence tautomerism. Valence tautomerism describes the property of electron transfer between metal centers and non-innocent ligands, of the type $M^n(L^m) \rightleftharpoons M^{n+1}(L^{m-1})$. This has previously been observed in quinone complexes of vanadium, manganese, cobalt, iron, and copper.¹⁷⁻²² Determining valence tautomerism is especially challenging when there is no accompanied change in overall spin, and thus no change in magnetic moment. Spectral differences may help to clarify this, although these may be obscured by strong ligand-to-metal charge transfer (LMCT) absorptions.

Many first-row transition metal quinone complexes have been synthesized and characterized, of both homoleptic and heteroleptic varieties.^{2,23-52} This thesis focuses on tris complexes of tetrachloro-1,2-benzoquinones, whose three oxidation states are shown in Figure 1.2. Dianionic tetrachlorocatecholates ($\text{Cl}_4\text{Cat}^{2-}$) is the most reduced form, which can be oxidized in two one-electron steps to radical anion tetrachloro-1,2-semiquinone ($\text{Cl}_4\text{SQ}^{\bullet-}$) and neutral tetrachloro-1,2-benzoquinone (Cl_4BQ).

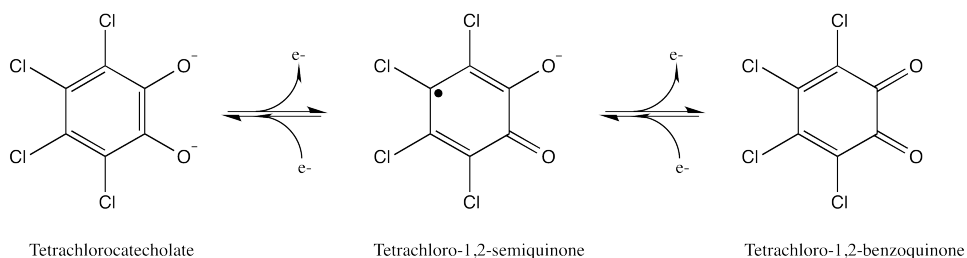
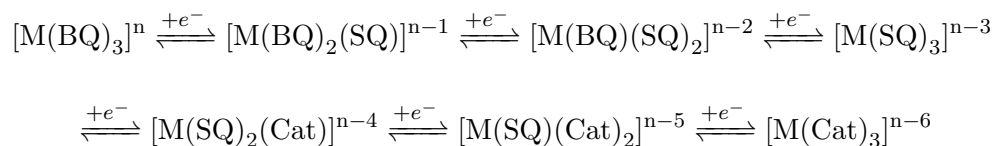


Figure 1.2: The three redox forms of tetrachloro-1,2-benzoquinone

Each of these quinone oxidation states has been isolated and characterized, including their redox potentials independent of metal chelation.⁵³⁻⁵⁵ Many different quinone ligands have been studied, which exhibit different electrochemical behavior based on their electrophilic properties and the properties of the metal center. Complexes of 9,10-phenanthraquinones, 3,5-di-*tert*-butyl-o-quinones, and 3,6-di-*tert*-butyl-o-quinones have been studied extensively, and their electrochemistry is well-characterized.^{2,21,28,44,45,47,48,52,54,56,57} First row transition metals will form tris-quinone complexes, theoretically allowing a seven-membered redox series:



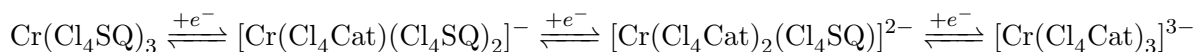
All redox activity is on the ligands, and n depends on the oxidation state of the metal center, M. The full seven-membered redox series has been observed using cyclic voltammetry for a chromium-quinone complex, where the chromium is +3 and the quinone ligands are 9,10-phenanthrenequinone, although for the more electrophilic tetrachloro-1,2-quinone, only the four

most reduced members of the redox series have been observed (Figure 1.3). The diketone structure of the benzoquinone makes it a weak donor ligand, and it is therefore subject to dissociation under the conditions of electrochemical experiments (polar solvents, high concentration of electrolyte). Electrophilic chlorines as substituents on the ring draw electron density away from the chelating oxygens, making Cl_4BQ even more prone to dissociation. Furthermore, the more electrophilic the ligands are, the more positive the potentials of the redox couples.⁵⁸ This means that theoretical potentials for complexes of tetrachloro-1,2-benzoquinone, if they were stable enough to be observed, would be far positive of most accessible electrochemical ranges.

Tris-tetrachloro-1,2-quinone complexes of vanadium and chromium have been previously synthesized and are well characterized.^{2,26} Their cyclic voltammograms are shown in Figures 1.3 and 1.4. Each shows three distinct redox couples, clearly identifying each of the four-membered redox series that goes from $(\text{Cl}_4\text{Cat})_3$ to $(\text{Cl}_4\text{SQ})_3$. The chromium complex is of more interest, as the chromium ion has enough kinetic stability so that all of the redox couples are ligand-based. The vanadium complex, on the other hand, also undergoes redox chemistry at the metal center.^{25,59}



For the chromium complex, three clear redox couples are clear over a range of approximately 1.3 V. This is an example of a Robin and Day Class II compound, although unlike other well-known mixed-valence compounds like the Creutz-Taube ion, $[\text{Ru}(\text{NH}_3)_5]_2(\text{C}_4\text{H}_4\text{N}_2)^{5+}$, the mixed-valency is ligand-centered rather than metal-centered.⁶ Charge is delocalized over all of the ligands, resulting in three distinct one electron, reversible redox couples, giving the redox series:



Intermediate mixed-charge members of this series have been characterized by Chang and Kitagawa, confirming the mixed-charge state of the ligands in the -1 and -2 complexes.^{42,60-62} This is in agreement with the SQ radical spectra obtained by EPR characterization on members of the series with charges of +1 and 1 (although EPR characterization of +1 complexes were not

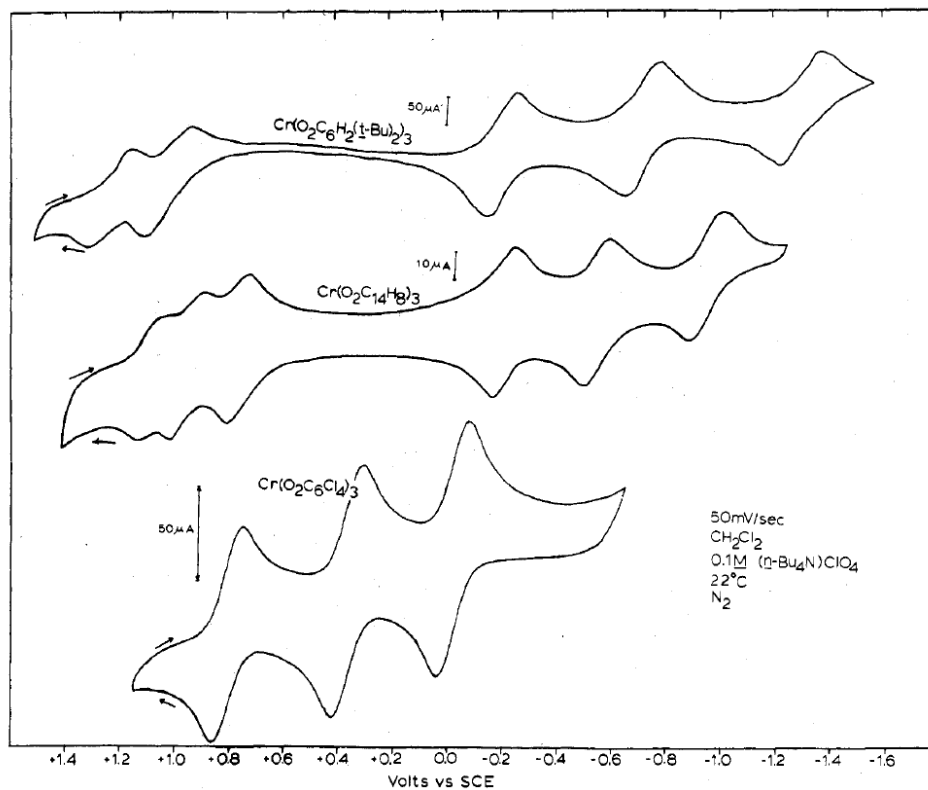


Figure 1.3: Cyclic voltammograms for $\text{Cr}(\text{O}_2\text{C}_6\text{H}_2(t\text{-Bu})_2)_3$, $\text{Cr}(\text{phen})_3$, and $\text{Cr}(\text{O}_2\text{C}_6\text{Cl}_4)_3$. All solutions were approximately 0.1 mM in complex except for $\text{Cr}(\text{phen})_3$ which was approximately 0.05 mM. Reprinted with permission. Copyright 1979 American Chemical Society.⁵⁸

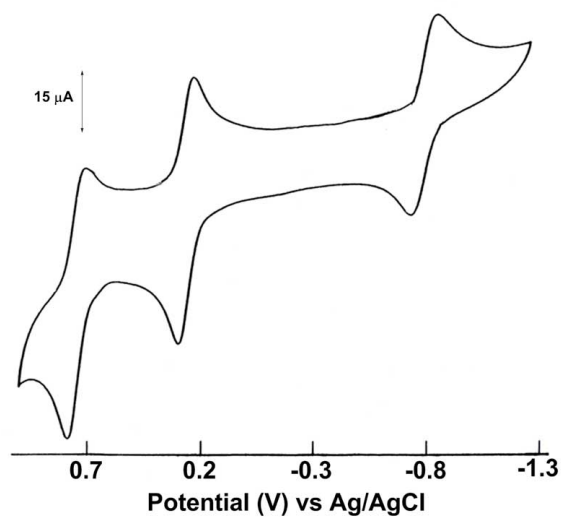


Figure 1.4: Cyclic voltammogram for $(\text{Ph}_4\text{P})_2[\text{V}^{\text{IV}}(\text{Cl}_4\text{SQ})(\text{Cl}_4\text{Cat})_2]$ in dichloromethane/0.1M $(\text{Bu}_4\text{N})(\text{PF}_6)$ at 100 mV/s. Adapted with permission. Copyright 2011 American Chemical Society.⁵⁹

performed on tris-tetrachloroquinone complexes), and with theoretical formulations for members of the redox series calculated by Gordon and Fenske, who also did theoretical formulations for the vanadium analog.^{47,63}

This thesis aims to complete the electrochemical characterization of the tris(tetrachloro-1,2-quinone)/first-row transition metal series by synthesizing and characterizing the manganese, iron, and cobalt analogs. (While quinone complexes of titanium have been reported, they are either with large tridentate ligands or are polymers.^{49,64,65}) The manganese complex has previously been synthesized as $(\text{Bu}_4\text{N})_2[\text{Mn}(\text{Cl}_4\text{Cat})_3]$ and characterized via spectroscopy and X-ray crystallography.^{32,38,46} Here, a synthetic method is presented using Pr_4N^+ as the counter-ion, which was confirmed as $(\text{Pr}_4\text{N})_2[\text{Mn}(\text{Cl}_4\text{Cat})_3]$ via spectroscopic analysis. The electrochemical behavior of the manganese complex is unclear, as the manganese center may itself be redox active and undergo valence tautomerism.

The iron analog was synthesized as both neutral $(\text{Fe}(\text{Cl}_4\text{SQ})_3)$ and trianion $([\text{Fe}(\text{Cl}_4\text{Cat})_3]^{3-})$ redox isomers, both of which were characterized with spectroscopy and X-ray crystallography, as well as Mössbauer spectroscopy. X-ray crystallization of the trianion complex synthesized as $(\text{Bu}_4\text{N})_3[\text{Fe}(\text{Cl}_4\text{Cat})_3]$ presented some challenges, due to disorder in the Bu_4N^+ counter-ion, but a synthesis with cobaltocenium as reducing agent and counter-ion, yielding $(\text{CoCp}_2)_3[\text{Fe}(\text{Cl}_4\text{Cat})_3]$, gave a precise crystal structure. The iron complex shows unique electrochemical properties by showing clear one-electron oxidations in cyclic voltammetry, similar to the chromium, but indistinct reductions except at very slow scan rates, less than 10 mV/s. The dependence of the reduction peaks on scan rate is unexpected, especially when compared to the vanadium and cobalt analogs. This has been investigated using differential pulse voltammetry.

The cobalt analog, $[\text{Co}(\text{Cl}_4\text{Cat})_2(\text{Cl}_4\text{SQ})]^{2-}$, has been synthesized using either Pr_4N^+ or Ph_4P^+ as counter-ion, and characterized with spectroscopy and X-ray crystallography. It is synthesized as a mixed-valence complex, rather than a tris(tetrachlorocatecholato) or tris(tetrachlorosemiquinonato) complex, which makes the X-ray crystallography challenging, as its mixed-valence properties introduce disorder into the crystal structure. Its electrochemical properties are similar in

some ways to the manganese and iron analogs, although it exhibits closely-overlapping, reversible, one-electron couples.

Electrochemical characterization of the complexes was performed using cyclic voltammetry and differential pulse voltammetry. Cyclic voltammetry investigated redox activity at the metal and ligands, while differential pulse voltammetry clarified the electron stoichiometry of the couples. Also of interest is the comproportionation constant, K_{com} , which describes the equilibrium $Ox + Red_2 \rightleftharpoons 2Red_1$ for species with more than two oxidation states. K_{com} is expressed by:

$$K_{com} = \exp\left(\frac{n_1 \cdot n_2 \cdot \Delta E^\circ \cdot F}{R \cdot T}\right)$$

K_{com} allows assignment of Robin and Day classification by describing communication between redox centers.^{6,15} For a Class I species, $K_{com} < 4$, and for Class III $K_{com} > 10^6$. Class II species have intermediate values. However, it is accepted that for $K_{com} < 10^2$ the compound is Class I, for $10^2 < K_{com} < 10^6$ the compound is Class II, and for $K_{com} > 10^6$ the compound is Class III.

Cyclic voltammetry (CV) is a very common electrochemical characterization technique. The cyclic voltammogram can provide much useful information about the redox properties of an analyte, especially its reversibility. An electrode reaction is considered reversible when the ratio between the reverse peak current and the forward peak, i_{pr}/i_{pf} , is constant at different scan rates and equal to one^{15,66} although this is somewhat complicated because the reverse peak's amplitude must be corrected to a baseline, due to capacitive currents. In addition, the ratio between the current of the forward peak and the square root of the scan rate, $i_{pf}/v^{1/2}$, is constant for a reversible process. In terms of potential, the potential of the forward peak should also be constant with scan rate, and the peak-to-peak separation should be approximately $59/n$ at 25 °C (from the relationship $\Delta E_p = \frac{2.3 \cdot R \cdot T}{n \cdot F}$). However, peak-to-peak separation can be affected by solution resistances and scan rates, so some variation from this does not necessarily mean the process isn't reversible. It is generally assumed that the diffusion coefficients of the reduced and oxidized species are approximately equal, so that the E° of the redox couple is equal to $E_{1/2}$, the potential halfway between the forward and reverse peaks.

When multiple electrons may be involved, cyclic voltammetry becomes more difficult as a diagnostic tool. For the couples here that are clearly observed and reversible, the challenge has been to determine how many electrons are involved stoichiometrically. One possible method is the addition of a known amount of ferrocene to the solution. However, direct comparison of peak currents has several complications. The capacitive current, which shifts the effective baseline from zero amperes, can make it difficult to determine what the peak current is in subsequential couples, especially if they are closely spaced. Further, from Fick's second law, one can derive that the maximum current for a planar electrode is:^{15,66}

$$i_p = 0.4463 \cdot A \cdot C_{ox}^* \cdot \frac{n^3 \cdot F^3 \cdot D_{ox} \cdot v}{\sqrt{R \cdot T}}$$

Or at 25 °C:

$$i_p = 2.69 \cdot 10^5 \cdot n^{3/2} \cdot A \cdot D_{ox}^{1/2} \cdot C_{ox}^* \cdot v^{1/2}$$

A = area of the working electrode (cm^2), D_{ox} = diffusion coefficient of the oxidized species (cm^2/s), C_{ox}^* = bulk concentration of the oxidized species (mol/cm^3), v = scan rate (V/s), R = universal gas constant, F = Faraday's constant, and n = electron stoichiometry.

This equation, known as the Randles-Sevcik equation, shows that the peak current not only depends on the bulk concentration of the oxidized species, C_{ox}^* , but also on the diffusion coefficient of the oxidized species, D_{ox} , and the number of electrons transferred, n . While n and D_{ox} are known for ferrocene ($n = 1$ and $D_{red} = 4.4 \cdot 10^{-6} \frac{\text{cm}^2}{\text{s}}$ in DMSO),⁶⁷ D_{ox} is unknown for the complex, which means that with two unknown variables it is difficult to discern whether an increase in i_p is due to number of electrons transferred or diffusivity. However, it's reasonable to assume that the complexes will have lower diffusivity than ferrocene, because of the higher molar mass and larger size. As the peak current and the square root of the diffusion coefficient are directly proportional, one would expect that a decrease in diffusion coefficient would result in a decrease in peak current if the number of electrons transferred is the same. A rough estimate of the diffusion coefficient can be made using cyclic voltammetry, if the ratio $i_{pf}/v^{1/2}$ is constant. Substituting $n=1, 2$, or 3 will give diffusion coefficients for each of those electron stoichiometries, which can then be more

reasonably compared to ferrocene.

Another complication with using ferrocene is that there can be interactions between the cyclopentadienyl rings and the quinone rings of the complex. As will be shown, this is relevant for the iron and manganese complexes, but not the cobalt complex, and depends on the E^o of the couples.

Differential pulse voltammetry (DPV) is traditionally used with a dropping mercury electrode, although here it was performed using the same setup as cyclic voltammetry, with a stationary vitreous carbon working electrode. This technique superimposes small, constant-potential pulses over a staircase potential waveform. The differential current is measured from the difference between the end of the pulse width and the end of the pulse period. Differential pulse voltammetry is useful mainly in separating closely-overlapped couples, although it can also be used to help determine the number of electrons in a couple from the relationship between FWHM of the peak, $\Delta E_{p/2}$, and the number of electrons transferred.^{15,66}

$$\Delta E_{p/2} = 3.53 \frac{R \cdot T}{n \cdot F}$$

Or at 25 °C:

$$\Delta E_{p/2} = \frac{90.5}{n} \text{ (mV)}$$

Differential pulse voltammetry also allows a more precise determination of $E_{1/2}$, from the relationship $E_{max} = E_{1/2} - \frac{E_{pulse}}{2}$. Generally it is also used at slower effective scan rates than cyclic voltammetry, at effective rates of 20 mV/s or less, which was especially convenient for analysis of the iron complex.

These syntheses and techniques complete the electrochemical characterization of the first row transition metal/tris-tetrachloroquinone complexes. Their similarities and differences are discussed, and their redox potentials and properties are determined.

Chapter 2

Experimental Section

2.1 Instrumentation and Methods

2.1.1 Cyclic Voltammetry and Differential Pulse Voltammetry

Cyclic voltammograms and differential pulse voltammograms were obtained with a Bioanalytical Systems Inc. (BASi) Epsilon potentiostat and the C3 cell stand apparatus coupled with the BASi Epsilon instrument interface software package. Cyclic voltammograms were performed in dimethylsulfoxide (DMSO) and methanol (MeOH). Both cyclic voltammetry and differential pulse voltammetry were run using a three electrode configuration in a 30 mL glass cell. The reference electrode for DMSO was an Ag/Ag⁺ electrode consisting of a silver wire in a 0.01 M solution of AgNO₃ in MeCN (approximately +0.54 V vs NHE), separated from solution by a Vycor frit. The reference electrode for MeOH was Ag/AgCl/Saturated KCl (approximately +0.197 V vs NHE), separated from solution by a Vycor frit. The ferrocene/ferrocenium couple (FeCp₂/FeCp₂⁺) was used as the internal standard, and is +0.91 V in DMSO vs Ag/Ag⁺ and +0.447 V in MeOH vs Ag/AgCl. Potentials are reported vs FeCp₂/FeCp₂⁺. For all solvents, the working electrode was a 3 mm diameter vitreous carbon electrode, and the auxiliary electrode was a 1.6 cm platinum wire. Electrolytes used were 0.1 M tetrabutylammonium hexafluorophosphate ((Bu₄N)(PF₆)) for DMSO, and 0.1 M NaCl for MeOH. Electrodes were cleaned by rinsing with acetone or nitric acid, and periodically polished.⁶⁸

2.1.2 Fourier Transform Infrared Spectroscopy

A Thermo Scientific Nicolet Avatar 360 FT-IR spectrometer was used to collect spectra in the 400 cm^{-1} to 4000cm^{-1} range. Spectra measurements were taken under a constant flow of N_2 in the sample chamber. Samples were prepared as KBr pellets using a hand press and mortar and pestle.

2.1.3 UV-Vis Spectroscopy

UV-Vis spectroscopy was performed on an Agilent 8435 UV-Vis spectrophotometer equipped with one tungsten and one deuterium lamp, using a quartz cuvette with one centimeter path length.

2.1.4 Near-IR Spectroscopy

NIR spectroscopy was performed on two instruments. Data for iron complexes was collected on a Perkin Elmer Lambda 9 UV/VIS/NIR spectrophotometer. Data for cobalt and manganese complexes was collected on a Varian Cary 5000 UV-Vis-IR spectrophotometer. Solid state samples were prepared as KBr pellets using a hand press and mortar and pestle, solvent samples used a 1 cm path length quartz cuvette.

2.1.5 Nuclear Magnetic Resonance Spectroscopy

^{31}P NMR spectra were obtained on a Bruker AV-III 300 MHz NMR spectrometer for triphenylphosphine oxide (TPPO) experiments. Measurements were performed in deuterated chloroform using the deuterium lock as an internal reference. Evans method magnetic measurements for $(\text{Bu}_4\text{N})_3[\text{Fe}(\text{Cl}_4\text{Cat})_3]$ were performed using ^1H NMR on the same instrument at 400 MHz in both acetonitrile and methanol. Due to lack of a deuterated internal reference, the instrument was manually shimmed.

2.1.6 Magnetic Susceptibility

Temperature dependent magnetic susceptibility measurements on iron-centered complexes were carried out by Dr. Karl Wieghardt at the Max Planck Institute of Bioinorganic Chemistry. Magnetic susceptibility data were measured on powder samples in the temperature range 2-300 K by using a SQUID susceptometer with a field strength of 1.0 T (MPMS-7, Quantum Design, calibrated with standard palladium reference sample, error <2%). The experimental data were corrected for diamagnetism by use of tabulated Pascals constant,⁶⁹ as well as for temperature-independent paramagnetism. Evans method susceptibility measurements using NMR spectroscopy were described in the NMR section.

Magnetic susceptibility measurements for cobalt- and manganese-centered complexes were made on an Johnson Matthey Magnetic Susceptibility Balance (Model MK1, C=1.094)

2.1.7 Mössbauer Spectroscopy

High magnetic field Mössbauer data were recorded by Dr. Karl Wieghardt at the Max Planck Institute of Bioinorganic Chemistry on a spectrophotometer with alternating constant acceleration. The minimum experimental line width was 0.24 mms^{-1} (full width at half-height). The sample temperature was maintained constant with either an Oxford Instruments Variox or an Oxford Instruments Mossbauer-Spectromag cryostat. The $^{57}\text{Co}/\text{Rh}$ source (1.8 GBq) was positioned at room temperature inside the gap of the magnet system at a zero-field position. Measurements were recorded at an external field strength of 4 T. Isomer shifts are quoted relative to iron metal at 300K. Spectra were simulated with the program MX. The hyperfine interactions for the ^{57}Fe were calculated using the nuclear Hamiltonian.⁷⁰

2.2 Reagents and Solvents

Reagents and solvents were used as purchased except as noted. Brackets indicate abbreviations used in text.

Acetone - Fisher Scientific

Acetonitrile [MeCN] - Sigma-Aldrich

Cobalt(II) acetate tetrahydrate - General Chemical Company

Cobaltocene - Acros Organics

Dichloromethane [DCM] - Fisher Scientific

Diethyl ether - Fisher Scientific

Dimethyl sulfoxide [DMSO] - Sigma-Aldrich

Ethanol [EtOH] - Pharmco-Aaper

Ferrocene [FeCp₂] was prepared by reaction of sodium cyclopentadienide (Aldrich) with iron(II) chloride tetrahydrate (Sigma-Aldrich)

Iron(III) nitrate nonahydrate - J. T. Baker Chemical Co.

Iron(0) pentacarbonyl - Aldrich Chemical Co.

Magnesium sulfate anhydrous - Mallinckrodt

Manganese(II) chloride tetrahydrate - Aldrich Chemical Co.

Methanol [MeOH] - Honeywell

Potassium bromide [KBr] - Aldrich Chemical Co.

Potassium hydroxide [KOH] - Sigma-Aldrich

Tetrabutylammonium hexafluorophosphate [(Bu₄N)(PF₆)] - Fluka Analytical

Tetrabutylammonium hydroxide [Bu₄NOH] - Sigma-Aldrich

Tetrachloro-1,2-benzoquinone [Cl₄BQ] - Aldrich Chemical Co

Tetrachlorocatechol monohydrate [$\text{Cl}_4\text{CatH}_2 \cdot \text{H}_2\text{O}$] was prepared by chlorination of catechol in glacial acetic acid, then recrystallized from water and ethanol.⁷¹

Tetraphenylphosphonium bromide [Ph_4PBr] - Aldrich Chemical Co.

Tetrapropylammonium bromide [Pr_4NBr] - Aldrich Chemical Co.

Toluene - Sigma-Aldrich

Triethylamine - Sigma-Aldrich

Triphenylphosphine oxide [TPPO] - Aldrich Chemical Co.

2.3 Preparation of complexes

2.3.1 Preparation of Bis(tetrachlorocatecholato)tetrachloro-1,2-semiquinonato-cobalt(III) Dianion

(Pr₄N)₂[Co(Cl₄Cat)₂(Cl₄SQ)] (F.W. 1169.27 g/mol) Tetrachlorocatechol monohydrate (0.80 g, 3.0 mmol) was dissolved in 50 mL of acetone with cobalt(II) acetate tetrahydrate (0.25 g, 1.0 mmol) in a round bottom flask, stirred, and bubbled with nitrogen for approximately 15 minutes. Under nitrogen atmosphere, 6 mmol of KOH was delivered via syringe (1.3 mL of 4.5 M aqueous solution). The reaction immediately darkened upon addition of KOH. This was left to stir overnight, sealed. The next day, Pr₄NBr was added (0.53 g, 2.0 mmol), and the solution was stirred until it fully dissolved. This solution was poured into a beaker to air-dry, yielding small brown crystals.

(Ph₄P)₂[Co(Cl₄Cat)₂(Cl₄SQ)] (F.W. 1475.36 g/mol) Tetrachlorocatechol monohydrate (0.80 g, 3.0 mmol) was dissolved in 50 mL of acetone with cobalt(II) acetate tetrahydrate (0.25 g, 1.0 mmol) in a round bottom flask, stirred, and bubbled with nitrogen for approximately 15 minutes. Under nitrogen atmosphere, 6 mmol of KOH was delivered via syringe (1.3 mL of 4.5 M aqueous solution). The reaction immediately darkened upon addition of KOH. This was left to stir overnight, sealed. The next day, Ph₄PBr was added (0.84 g, 2.0 mmol), and the solution

was stirred until it fully dissolved. This solution was poured into a beaker to air-dry, yielding small greenish/brown crystals.

2.3.2 Preparation of Tris(tetrachlorocatecholato)manganese(IV) Dianion

$(\text{Pr}_4\text{N})_2[\text{Mn}(\text{Cl}_4\text{Cat})_3]$ (F.W. 1165.29 g/mol) Tetrachlorocatechol monohydrate (0.80 g, 3.0 mmol) was dissolved in 50 mL of acetone with triethylamine (0.9 mL, 6.0 mmol). Manganese(II)chloride tetrahydrate (0.20 g, 1.0 mmol) was dissolved in another 50 mL of acetone. These solutions were combined in a round bottom flask, then Pr_4NBr (0.53 g, 2.0 mmol) was added. This solution was bubbled with O_2 gas for approximately one hour, then left to stir overnight. The next day, the solution was poured into a beaker to air-dry, yielding a dark blue product. This was redissolved in an acetone/toluene mixture and left to dry, yielding dark blue crystals.

2.3.3 Preparation of Tris(tetrachloro-1,2-semiquinonato)iron(III)

$\text{Fe}(\text{Cl}_4\text{SQ})_3 \cdot \text{C}_7\text{H}_8$ (F.W. 885.62 g/mol) Toluene solvent was dried with MgSO_4 , degassed, and stored under 4A molecular sieves before use. The reaction was performed under inert atmosphere. $\text{Fe}(\text{CO})_5$ (0.92 mL, 7 mmol) was placed in 12 mL toluene. The mixture was slowly added dropwise to a solution containing tetrachloro-1,2-benzoquinone (5 g, 20 mmol) dissolved in 75 mL toluene. Addition took place over the period of one hour and stirred until all bubbling ceased. The solution was allowed to cool in an ice bath for 15 min and then was filtered. Solid was recrystallized in a methylene chloride/toluene solution to give dark green crystals.

2.3.4 Preparation of Tris(tetrachlorocatecholato)iron(III) Trianion

$(\text{Bu}_4\text{N})_3[\text{Fe}(\text{Cl}_4\text{Cat})_3]$ (F.W. 1520.89 g/mol) The synthesis was performed under ambient conditions. Tetrachlorocatechol (3 g, 0.012 mol) was dissolved in 50 mL of methanol and deprotonated with 24 mL of 0.1 M tetrabutylammonium hydroxide (Bu_4N)OH (0.024 mol). The mixture was added slowly to a solution of $\text{Fe}(\text{NO}_3)_3 \cdot 9\text{H}_2\text{O}$ (1.6 g, 4 mmol) dissolved in 50 mL of methanol. Slow evaporation of solvent produced red cubic crystals.

(CoCp₂)₃[Fe(Cl₄Cat)₃] (F.W. 1360.48 g/mol) Previously synthesized Fe(Cl₄SQ)₃ (0.240 g, 0.3 mmol) was dissolved in 30 mL degassed dichloromethane under argon atmosphere. Cobaltocene (0.153 g, 0.9 mM) was dissolved in 90 mL dichloromethane under argon, then added dropwise to the Fe(Cl₄SQ)₃ solution with care not to allow any oxygen into the reaction flask. The solution was allowed to stir overnight while solvent was removed with a steady stream of argon gas. The resulting solid was re-solvated in acetonitrile and filtered. The red/purple solid was isolated and recrystallized to give red shaft-like crystals.

Chapter 3

Results and Discussion

3.1 Characterization of Complexes

3.1.1 Preparation of Complexes

3.1.1.1 Synthesis of $(\text{Pr}_4\text{N})_2[\text{Mn}(\text{Cl}_4\text{Cat})_3]$

The manganese analog has been previously synthesized and characterized,^{32,46} although these syntheses used Bu_4N^+ as a counter-ion, so most characterization here was done to confirm successful synthesis. Unlike the synthesis methods used by Sheriff⁴⁶ and Ruiz,³² where Bu_4NOH was the source of both the counter-ion and the base to deprotonate the catechol, this synthesis used Pr_4NBr as counter-ion and triethylamine as deprotonation agent. The main reason for this was that using Bu_4NOH gave a very wet, gooey product that was difficult to isolate, while using acetone and triethylamine gave a dark blue product that was easy to recrystallize directly from acetone and toluene. Using triethylamine and Pr_4NBr accomplishes the same effect as Bu_4NOH , which is to prevent dechlorination and polymerization reactions with the tetrachlorocatechol.^{38,40,72,73} Another difference was bubbling the solution with O_2 gas, to accelerate the oxidation of the manganese, instead of stirring under reflux.

3.1.1.2 Synthesis of Iron Complexes

$\text{Fe}(\text{Cl}_4\text{SQ})_3$ The neutral iron complex was synthesized under inert atmosphere due to the air sensitivity and volatility of $\text{Fe}(\text{CO})_5$, which has a flash point of -15°C . The $\text{Fe}(0)$ is oxidized by

the tetrachloro-1,2-benzoquinone, which is itself reduced to a semiquinone. This reaction is fairly rapid, so the reagents were added dropwise to avoid bubbling over as CO gas was released.

(Bu₄N)₃[Fe(Cl₄Cat)₃] and (CoCp₂)₃[Fe(Cl₄Cat)₃] The trianion iron complex was synthesized a few different ways. (Bu₄N)₃[Fe(Cl₄Cat)₃] used iron(III) nitrate in the synthesis, so the iron was already in the desired oxidation state. Chelation of the tetrachlorocatechol only required that the catechol be deprotonated, which was accomplished with a base that then also provided the source of counter-ion (Bu₄NOH). The other synthetic method was reduction of Fe(Cl₄SQ)₃ by cobaltocene, a strong organometallic reducing agent. This was performed under inert atmosphere due to the air sensitivity of both Fe(Cl₄SQ)₃ and cobaltocene. Oxidized cobaltocenium (CoCp₂⁺) was then incorporated into the crystal lattice as the counter-ion for [Fe(Cl₄Cat)₃]³⁻

3.1.1.3 Synthesis of [Co(Cl₄SQ)(Cl₄Cat)₂]²⁻

The synthesis of [Co(Cl₄SQ)(Cl₄Cat)₂]²⁻ has slower kinetics than either the iron- or manganese-complex synthesis - it takes more time for the tetrachlorocatechol to chelate to the cobalt. One problem with the synthesis is that adding any bromide-containing counter-ion too early will yield nothing but cobalt bromide, which reacts with Co²⁺ in solution and immediately precipitates out. Another important aspect of the synthesis is the need for a mostly-nitrogen atmosphere, but not entirely nitrogen. Because KOH is used as the base to deprotonate the catechol, deprotonation is very rapid. However, chelation to the cobalt is much slower, due to coordination of the catecholate with K⁺.³² If too much oxygen is present, a side reaction with the deprotonated catechol can occur to form chloranilic acid^{72,73} and, interestingly, if KOH is not added promptly (within approximately 10-15 minutes) CoCl₂ will form, as even weak bases (here, the acetate from cobalt (II) acetate) can cause dechlorination of the catechol. This is not a problem observed with either the manganese or iron syntheses, as the chelation is fast enough to stabilize the catechol before undesired side products are formed. However, attempting the synthesis using a bubbler was unsuccessful, because some oxygen is needed to oxidize the Co²⁺ to Co³⁺. Instead, flushing the solution with nitrogen and injecting KOH under nitrogen atmosphere, then leaving it to react overnight while still sealed,

allowed the trace oxygen necessary to oxidize the cobalt without dechlorinating the tetrachlorocatechol before it could chelate. After leaving the reaction enough time to go to completion, the counter-ion could safely be added without forming CoBr_2 .

Attempts to synthesize $(\text{Pr}_4\text{N})_2[\text{Co}(\text{Cl}_4\text{Cat})_2(\text{Cl}_4\text{SQ})]$ with triethylamine as the base, as was done with manganese, did appear to yield the desired complex, but syntheses were extremely difficult to crystallize and the synthesis with KOH was deemed preferable. All data analyzed here was done on the KOH synthesis. Synthesis was also attempted without adding more counter-ion, as in the $\text{K}_3[\text{Fe}(\text{Cl}_4\text{Cat})_3]$ synthesis, but the product was amorphous and not deemed suitable for analysis. Similarly, an attempt was made to reduce $[\text{Co}(\text{Cl}_4\text{Cat})_2(\text{Cl}_4\text{SQ})]^{2-}$ to $[\text{Co}(\text{Cl}_4\text{Cat})_3]^{3-}$ using cobaltocene, as was done with the iron. While a color change was observed as yellow cobaltocenium appeared, no characterizable product of $[\text{Co}(\text{Cl}_4\text{Cat})_3]^{3-}$ could be isolated.

3.1.2 X-Ray Crystallography

3.1.2.1 Crystal Structure of $[\text{Mn}(\text{Cl}_4\text{Cat})_3]^{2-}$

The manganese complex has been well characterized by others, so X-Ray crystallography was not performed on the manganese complex synthesized here. Crystallography performed by Ruiz³² is duplicated here with permission for comparison to the iron and cobalt complexes (Figure 3.1 and Table 3.1). The Mn-O bond lengths are all very similar, averaging 1.88Å, confirming that all ligands have the same oxidation state, and are consistent with other characterized Mn^{IV} catecholate complexes.^{33,44} The geometry around the Mn center is trigonally-distorted octahedral, due to the constraints of the five-membered ring's bite distance (average bite angle 85.6°).

3.1.2.2 Crystal Structure of Iron Complexes

X-Ray crystallography performed on $\text{Fe}(\text{Cl}_4\text{SQ})_3$ (Figure 3.2), $(\text{CoCp}_2)_3[\text{Fe}(\text{Cl}_4\text{Cat})_3]$ (Figure 3.3, and $(\text{Bu}_4\text{N})_3[\text{Fe}(\text{Cl}_4\text{Cat})_3]$ confirms three bidentate ligands surrounding the iron center in a trigonally-distorted octahedral geometry with D_3 symmetry. In the structure for $(\text{CoCp}_2)_3[\text{Fe}(\text{Cl}_4\text{Cat})_3]$, the cobaltocenium counter-ions participate in pi-stacking on the catecholate ligands.

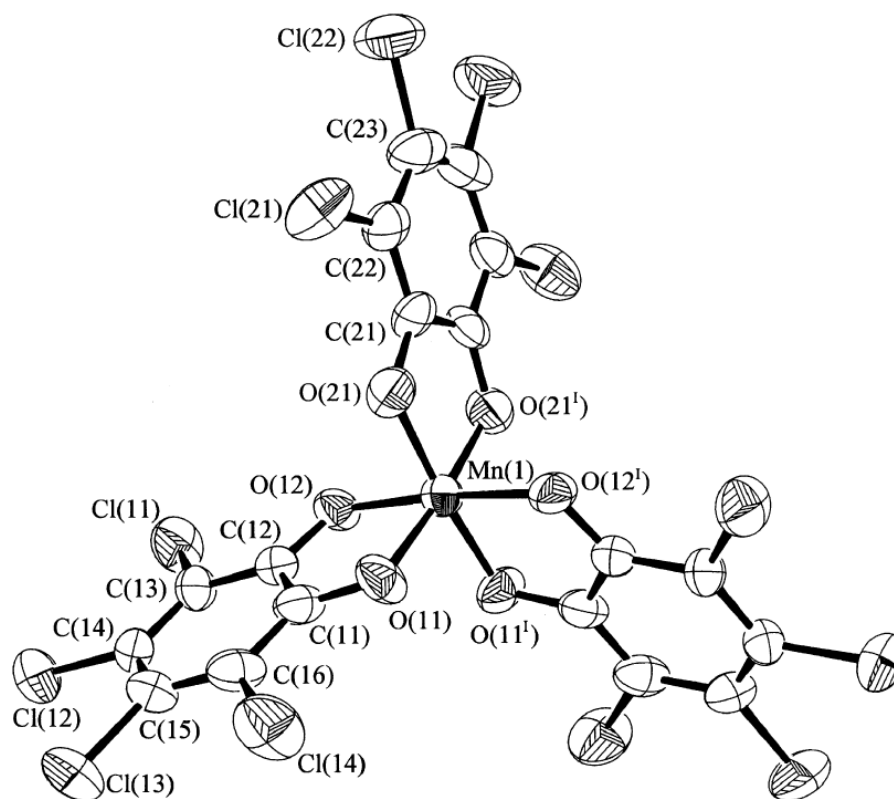


Figure 3.1: X-Ray structure of $[\text{Mn}(\text{Cl}_4\text{Cat})_3]^{2-}$, ellipsoids drawn at 30% probability level. Counterion (not pictured) is Ph_4P^+ . Reprinted from Ruiz et al.³² with permission from Elsevier.

Table 3.1: Selected bond lengths and angles of $(\text{Ph}_4\text{P})_2[\text{Mn}(\text{Cl}_4\text{Cat})_3]$.³² symmetry code: $I = x, y, -z + 1/2$

Bond Lengths (Å)		Bond Angles (deg)	
Mn(1)–O(11)	1.892(6)	O(11)–Mn(1)–O(12)	85.6(2)
Mn(1)–O(12)	1.885(5)	O(11)–Mn(1)–O(21)	90.8(2)
Mn(1)–O(21)	1.877(6)	O(11)–Mn(1)–O(11 ^I)	92.9(4)
		O(11)–Mn(1)–O(12 ^I)	90.8(2)
		O(11)–Mn(1)–O(21 ^I)	175.1(3)
		O(12)–Mn(1)–O(21)	92.7(2)
		O(12)–Mn(1)–O(12 ^I)	174.8(3)
		O(12)–Mn(1)–O(21 ^I)	91.2(2)
		O(21)–Mn(1)–O(21 ^I)	85.7(3)

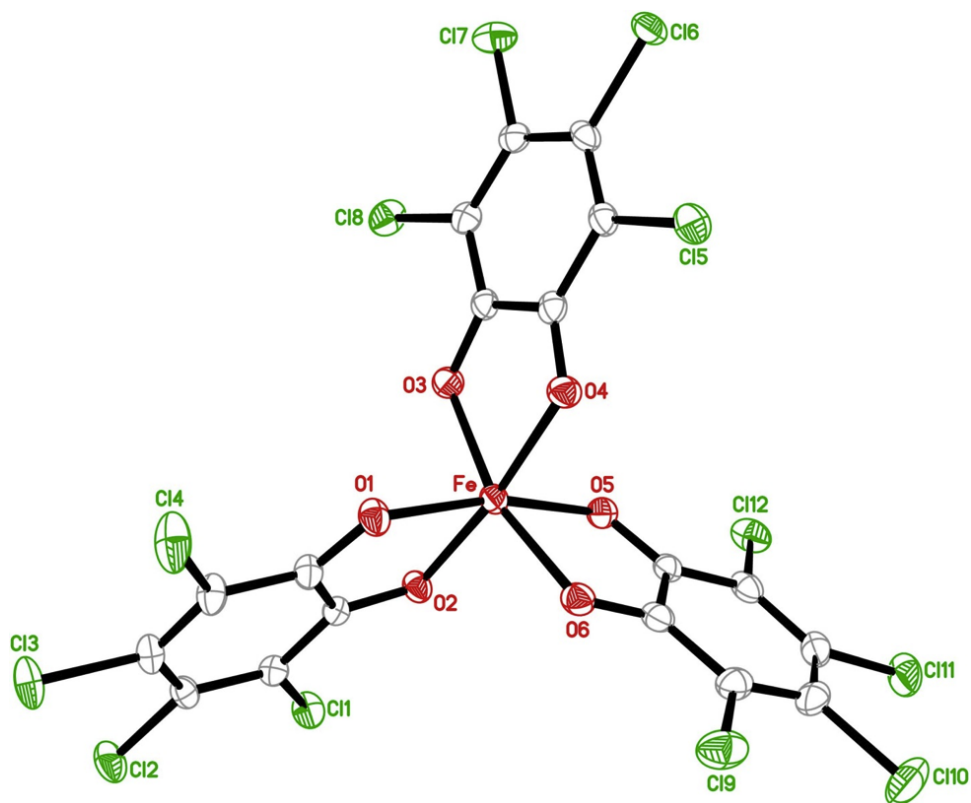


Figure 3.2: X-Ray structure of $\text{Fe}(\text{Cl}_4\text{SQ})_3$, solvent molecules omitted for clarity. Ellipsoids drawn at 50% probability level.

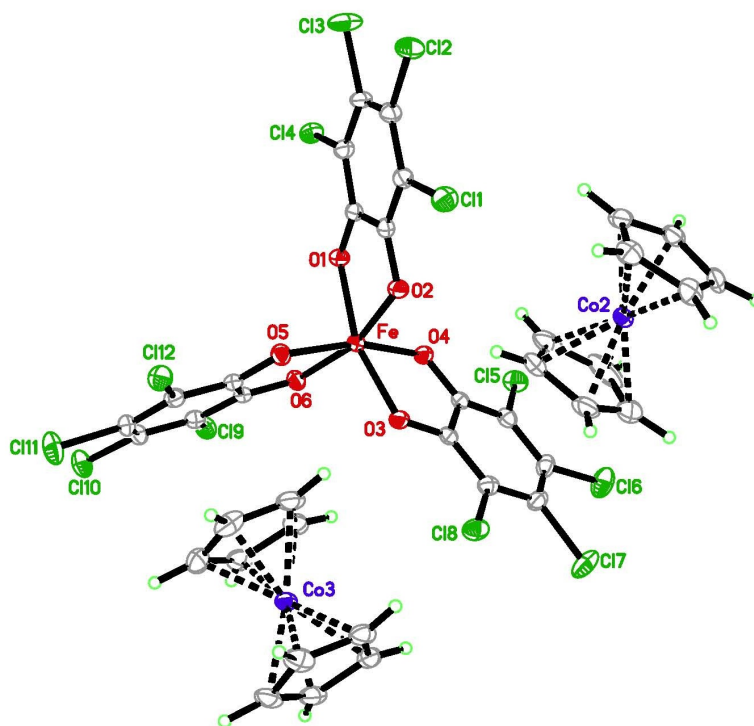


Figure 3.3: X-Ray structure of $(\text{CoCp}_2)_3[\text{Fe}(\text{Cl}_4\text{Cat})_3]$, ellipsoids drawn at 30% probability level. A third CoCp_2^+ counter-ion has been omitted, it occupies an interstitial site.

The difference in charge between the semiquinone and catechol ligands is reflected in a change in average C-O bond lengths of the complexes. Typical bond lengths for semiquinone complexes are approximately 1.29 Å, while bond lengths for catechol are longer at 1.34 Å.⁵⁷ The neutral complex exhibits average bond lengths typical for semiquinonate complexes previously reported. However, the trianion complexes exhibit C-O bond lengths of 1.307 Å and 1.313 Å, which, while still longer than the semiquinone C-O bond lengths, are shorter than previously reported for catecholate ligands. An explanation for the C-O bond shortening can be found in the lengthening of the C-Cl bonds, which are 1.736 Å and 1.735 Å in the catecholate and only 1.709 Å in the semiquinonate. (See Table 3.2) This suggests that electron density is delocalized over the C-Cl bonds in the catecholate ligands, resulting in a shortening of the C-O bonds.

Table 3.2: Average bond lengths (Å) for iron tetrachloroquinone complexes

	$\text{Fe}(\text{Cl}_4\text{SQ})_3 \cdot \text{C}_7\text{H}_8$	$(\text{Bu}_4\text{N})_4[\text{Fe}(\text{Cl}_4\text{Cat})_3](\text{NO}_3) \cdot 3 \text{C}_7\text{H}_8$
Fe-O	2.019(2)	2.017(4)
C1-O	1.275(3)	1.307(6)
C1-C2	1.461(3)	1.431(8)
C2-C3	1.420(3)	1.390(8)
C3-C4	1.372(3)	1.406(9)
C4-C5	1.439(3)	1.377(10)
C-Cl	1.709(2)	1.736(7)
	$(\text{CoCp}_2)_3[\text{Fe}(\text{Cl}_4\text{Cat})_3] \cdot 2 \text{C}_7\text{H}_8$	${}^a\text{K}_3[\text{Fe}(\text{Cat})_3] \cdot 1.5 \text{H}_2\text{O}$
Fe-O	2.029(1)	2.015(6)
C1-O	1.313(2)	1.349(3)
C1-C2	1.433(2)	1.409(6)
C2-C3	1.393(2)	1.383(2)
C3-C4	1.404(3)	1.385(4)
C4-C5	1.380(3)	1.350(9)
C-Cl	1.735(2)	n/a

a Raymond 1976³⁰

3.1.2.3 Crystal Structure of $[\text{Co}(\text{Cl}_4\text{SQ})(\text{Cl}_4\text{Cat})_2]^{2-}$

The cobalt-centered complex was synthesized as a dianion, $[\text{Co}(\text{Cl}_4\text{SQ})(\text{Cl}_4\text{Cat})_2]^{2-}$, with two different counter-ions for characterization, Pr_4N^+ and Ph_4P^+ . X-ray crystallography was performed on both complexes, however, due to the mixed-charge ligands, resolving the crystal

structure is quite difficult.^{7-9,17} Because there is electron transfer between ligands, there is disorder present in the counter-ions. In an attempt to ameliorate this, the complex was synthesized with the large, relatively inflexible Ph_4P^+ as the counter-ion. In the X-ray structure of $(\text{Ph}_4\text{P})_2[\text{Co}(\text{Cl}_4\text{Cat})_2(\text{Cl}_4\text{SQ})]$ (Figure 3.4), the disorder can be seen in the flexing of what should be rigid phenyl rings, as well as two extra oxygen atoms near the cobalt center. In contrast, the X-ray structure of $(\text{Pr}_4\text{N})_2[\text{Co}(\text{Cl}_4\text{Cat})_2(\text{Cl}_4\text{SQ})]$ shows far more disorder in the Pr_4N^+ counter ion, with its flexible propyl groups, as well as some solvent molecule disorder. The presence of two counter ions per unit, however, illustrates that the complex synthesized is the dianion, with one ligand in the radical semiquinone oxidation state.

In Figure 3.5 the counter-ions have been omitted for clarity. Here the octahedral structure of the complex is clearer. However, because the charge can move between ligands, the bond lengths are not truly consistent with either catechol or semiquinone ligands (see Table 3.3).

Table 3.3: Selected bond lengths and angles of $(\text{Ph}_4\text{P})_2[\text{Co}(\text{Cl}_4\text{SQ})(\text{Cl}_4\text{Cat})_2]$

Bond Lengths (Å)		Bond Angles (deg)	
Co–O1	1.903	O1–Co–O2	87.38
Co–O2	1.860	O2–Co–O3	90.98
Co–O3	1.897	O3–Co–O4	86.63
Co–O4	1.884	O4–Co–O5	89.87
Co–O5	1.889	O5–Co–O6	89.05
Co–O6	1.835	O6–Co–O1	177.14
Cl1–C3	1.758	O2–Co–O4	176.47
Cl2–C4	1.777	O3–Co–O5	175.62
Cl3–C5	1.682		
Cl4–C6	1.706		
Cl5–C9	1.597		
Cl6–C10	1.800		
Cl7–C11	1.829		
Cl8–C12	1.722		
Cl9–C15	1.796		
Cl10–C16	1.796		
Cl11–C17	1.753		
Cl12–C18	1.755		

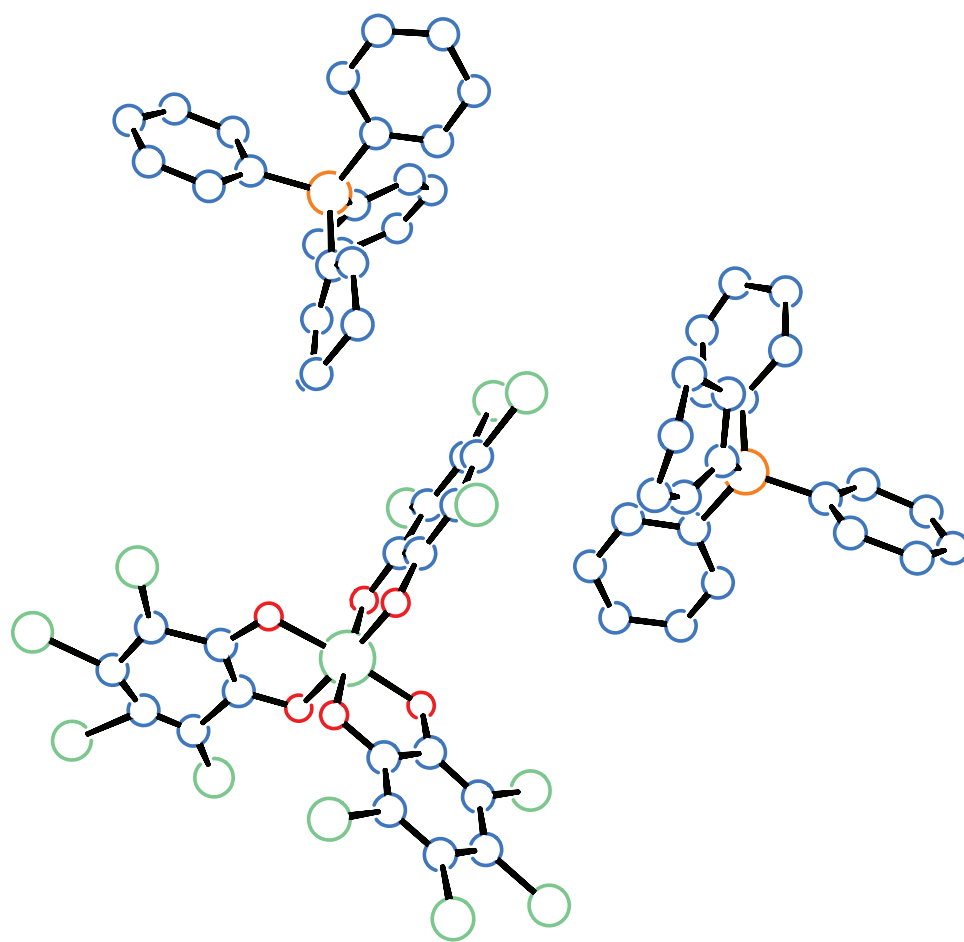


Figure 3.4: X-Ray structure of $(\text{Ph}_4\text{P})_2[\text{Co}(\text{Cl}_4\text{SQ})(\text{Cl}_4\text{Cat})_2]$. Note two extra oxygen atoms (O7, O8) near cobalt center.

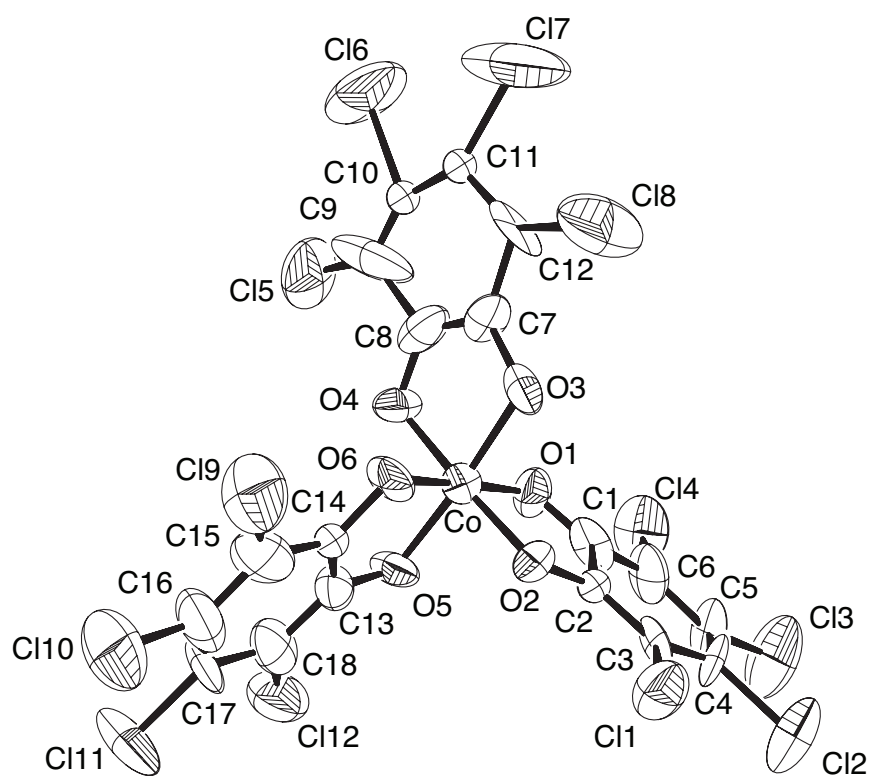


Figure 3.5: X-Ray structure of $(\text{Ph}_4\text{P})_2[\text{Co}(\text{Cl}_4\text{SQ})(\text{Cl}_4\text{Cat})_2]$, counter-ion and extra oxygens omitted for clarity

3.1.3 Magnetic Properties

3.1.3.1 Magnetic Characterization of $(\text{Pr}_4\text{N})_2[\text{Mn}(\text{Cl}_4\text{Cat})_3]$

Magnetic susceptibility measurements on $(\text{Pr}_4\text{N})_2[\text{Mn}(\text{Cl}_4\text{Cat})_3]$ give $S = \frac{3}{2}$, as expected for Mn^{IV} with three catecholate ligands. Magnetic susceptibility measurements giving the same spin have previously been performed on $(\text{Bu}_4\text{N})_2[\text{Mn}(\text{Cl}_4\text{Cat})_3]$ by Sheriff.⁴⁶

3.1.3.2 Magnetic Characterization of the Iron Complex Redox Series

Magnetic susceptibility measurements were obtained via the Evans method using both methanol and acetonitrile in order to identify a change in the iron oxidation state in response to solvent polarity.^{74,75} From the relative frequency shift $\Delta v/v = v_{\text{solvent}} - (v_{\text{solvent}+\text{complex}})$ produced by the paramagnetic metal complex, the number of unpaired electrons can be calculated using this formula, where MW is in kg/mol and m is in kg/m^3 :

$$\mu = 798 \sqrt{\left(\frac{-3\Delta v}{vm} + \chi_{\text{mass},0} \right) \cdot MW}$$

With a Δv of 13.6 Hz in methanol and 12.8 Hz in acetonitrile, $v = 400$ Hz, and using the relationship $\mu_{\text{eff}} = g(\mathbf{S}(\mathbf{S} + 1))^{\frac{1}{2}}$ where $g = 2.0023$, this method gives an iron oxidation state of 3^+ , with an $\mathbf{S} = \frac{5}{2}$ for $[\text{Fe}(\text{Cl}_4\text{Cat})_3]^{3-}$, indicating that the oxidation state of the metal is independent of solvent polarity.

Further magnetic susceptibility and high-field Mössbauer data on $(\text{Bu}_4\text{N})_3[\text{Fe}(\text{Cl}_4\text{Cat})_3]$ confirms that the metal is high spin iron(III) (Figure 3.6)^{43,76,77}.

3.1.3.3 Magnetic Characterization of $(\text{Ph}_4\text{P})_2[\text{Co}(\text{Cl}_4\text{Cat})_2(\text{Cl}_4\text{SQ})]$

Magnetic susceptibility measurements of $(\text{Ph}_4\text{P})_2[\text{Co}(\text{Cl}_4\text{Cat})_2(\text{Cl}_4\text{SQ})]$ confirm that the complex has spin $S=1/2$, which is consistent with low-spin Co^{III} with one semiquinone ligand.

The EPR spectrum of the cobalt complex is interesting because of the lack of Co hyperfine coupling. An unpaired electron would normally be expected to interact with the cobalt's nuclear spin ($I = \frac{7}{2}$ for ^{59}Co), but no splitting is observed (Figure 3.7). In order for the hyperfine splitting

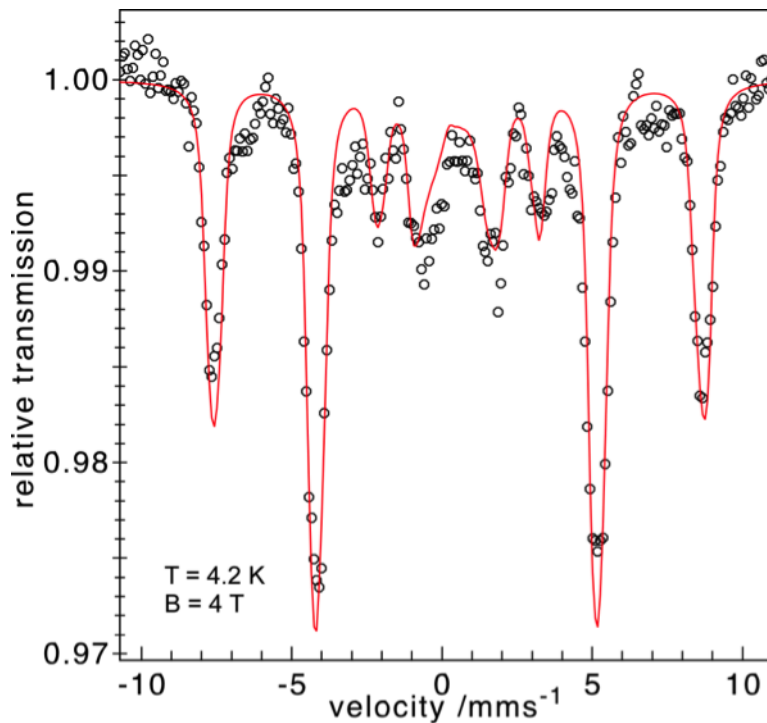


Figure 3.6: High field Mössbauer spectrum on $(\text{Bu}_4\text{N})_3[\text{Fe}(\text{Cl}_4\text{Cat})_3]$ recorded at a field strength of 4 T at a temperature of 4.2 K. The spectrum shows the six lines associated with $hs\text{-Fe}^{3+}$ with additional lines at -2 and $+3$ mm/s associated with the $|\pm 3/2\rangle$ Kramers doublet. The red line is a simulation with $S = 5/2$, $D = -0.2 \text{ cm}^{-1}$, $E/D = 0.33$, $g = 2$, $\delta = 0.52 \text{ mm/s}$, $\Delta\text{EQ} = 0.75 \text{ mm/s}$, $\eta = 1$, $A/g_N\beta_N = -21.8 \text{ T}$.

not to appear, the electron transfer reaction between the semiquinone and catechol ligands must happen on the EPR timescale, on the order of 10^{-9} seconds. This indicates the coupling between ligands is very weak.

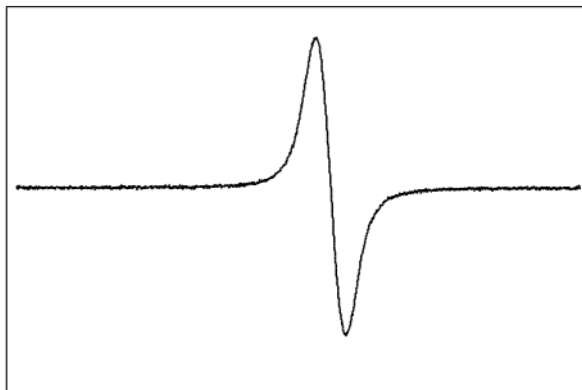


Figure 3.7: Electron Paramagnetic Resonance of $(\text{Pr}_4\text{N})_2[\text{Co}(\text{Cl}_4\text{Cat})_2(\text{Cl}_4\text{SQ})]$

3.1.4 Spectroscopy

3.1.4.1 Spectroscopy of $(\text{Pr}_4\text{N})_2[\text{Mn}(\text{Cl}_4\text{Cat})_3]$

UV-Visible spectroscopy in MeCN confirmed that the tris-catecholate complex had been synthesized successfully (Figure 3.8) The characteristic λ_{max} at 615 nm with shoulders at 700 nm and 425 nm in MeCN were all observed, matching UV-Vis spectra taken by Sheriff.⁴⁶ These can be assigned to LMCTs, which are typical of high-valent Mn^{IV} catecholate species.^{18-20,33,35,44,56} Absorbances farther into the UV at 310 nm and 220 nm belong to catechol, which has molar absorptivity in the tens of thousands.

FTIR data also correlates with previous literature, with catecholate C-O stretch at 1440 cm^{-1} and C-Cl stretch at 800 cm^{-1} .

3.1.4.2 Spectroscopy of the Iron Complexes

Spectral characterization of the different iron complexes show clear differences between the neutral and trianion species. This allows a way to easily identify different redox states of the

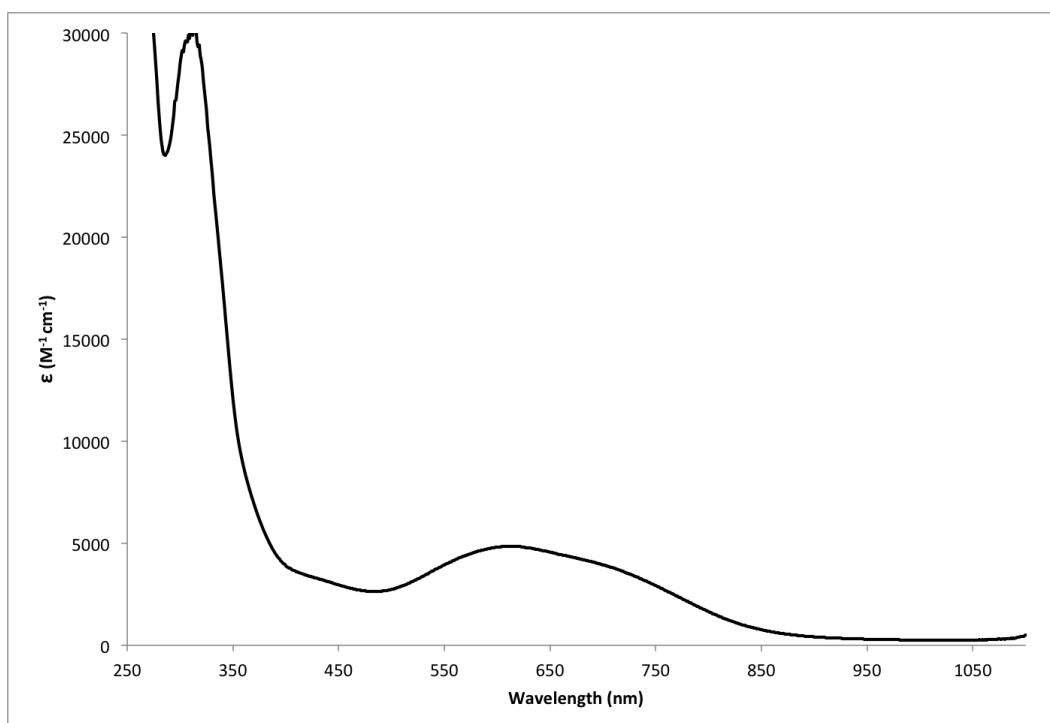


Figure 3.8: UV-Visible spectrum of $(\text{Pr}_4\text{N})_2[\text{Mn}(\text{Cl}_4\text{Cat})_3]$, 0.0001 M in MeCN

complex. The main features are LMCT in the visible region.

Electronic spectra for $\text{Fe}(\text{Cl}_4\text{SQ})_3$ consist of a single transition in the visible region, which has a slight solvatochromic dependence, shifting from $\lambda_{max} = 415$ nm in THF to 460 nm in CH_2Cl_2 ($\epsilon = 4.5 \cdot 10^3 \text{M}^{-1} \text{cm}^{-1}$). This shift to a lower energy for more polar solvents is typical for a LMCT band.

Electronic spectra for $[\text{Fe}(\text{Cl}_4\text{Cat})_3]^{3-}$ show greater solvent dependence than $\text{Fe}(\text{Cl}_4\text{SQ})_3$. Spectra in aprotic solvents show an intense band at 490 nm ($\epsilon = 6.5 \cdot 10^3 \text{M}^{-1} \text{cm}^{-1}$), which is similar to the $[\text{Fe}(\text{Cat})_3]^{3-}$ anion.⁷⁸ In protic solvents the solution is purple, and the transition shifts to 580 nm and broadens. Spectra were recorded in MeCN and EtOH, with varying MeCN:EtOH ratios (Figure 3.10). The shift of λ_{max} from 490 nm to 580 nm is apparent as percent EtOH increases, with an isosbestic point at 575 nm. This implies that the electronic structure of the complex varies depending on whether it is in a protic or aprotic solvent, as MeCN and EtOH have similar polarities. The solvent dependent change in electronic structure could be due to a change in spin state at the metal (spin-crossover) or due to a shift in charge distribution by forming the iron(II) redox isomer $[\text{Fe}^{\text{II}}(\text{Cl}_4\text{SQ})(\text{Cl}_4\text{Cat})_2]^{3-}$.^{22,79} Either of these would result in a change in magnetic moment, but solvent-dependent magnetic moment measurements showed values typical for *hs*- Fe^{III} (Section 3.1.3.2). From this, it is most likely that the ground state electronic structure is unperturbed, but the excited state electronic structure is solvent-dependent.

3.1.4.3 Spectroscopy of $(\text{Pr}_4\text{N})_2[\text{Co}(\text{Cl}_4\text{Cat})_2(\text{Cl}_4\text{SQ})]$

The most prominent feature of the electronic absorption spectrum is the peak at 635 nm, with molar absorptivity of $400 \text{M}^{-1} \text{cm}^{-1}$, as well as a shoulder at 440 nm ($\epsilon 1150 \text{M}^{-1} \text{cm}^{-1}$). Farther into the UV is intense absorption by the catechol ligands, whose molar absorptivity is typically in the tens of thousands. As the instrument only records absorbance up to 4 (0.01% transmittance) the molar absorptivity of the catechol is not clear here.

Near-infrared spectra taken in the solid state with a KBr pellet shows a very weak, broad intervalence charge transfer band at approximately 1400 nm. Again, this is consistent with weakly

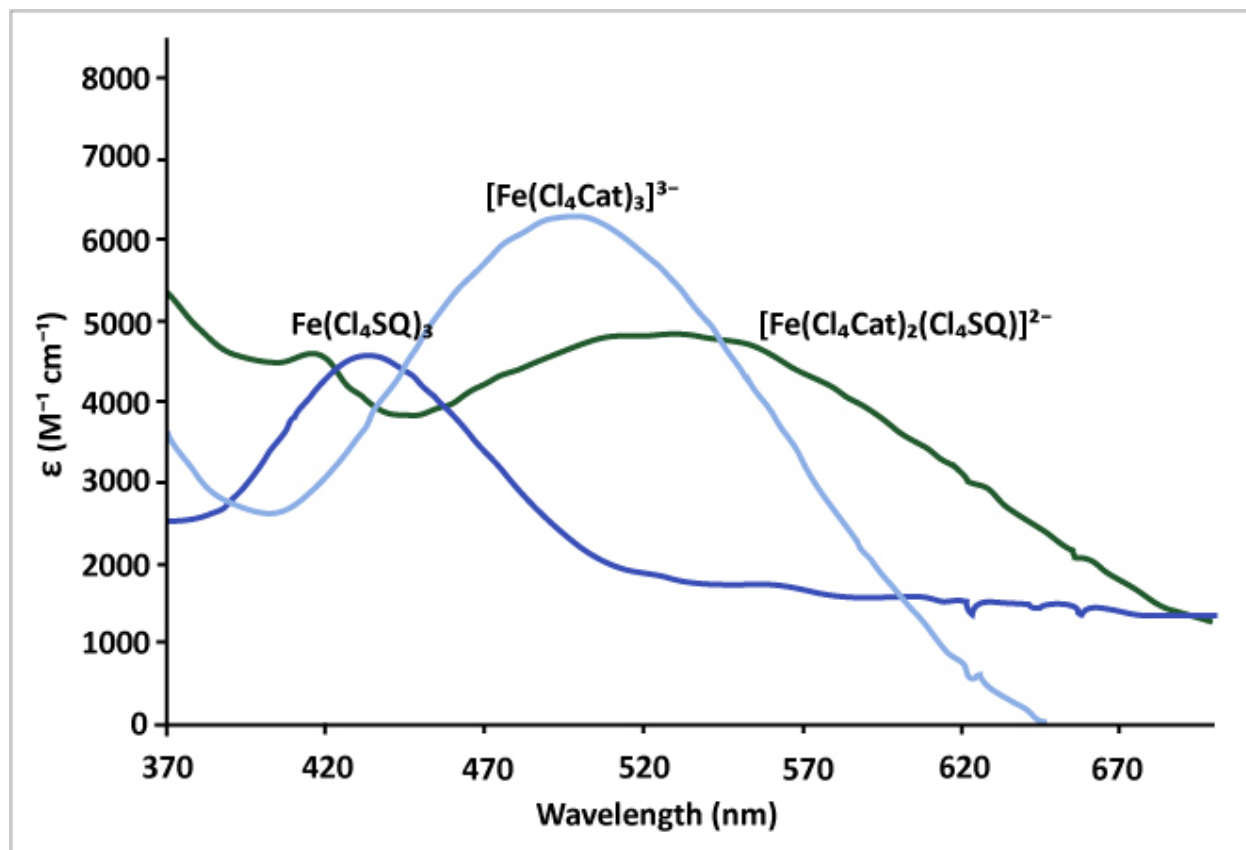


Figure 3.9: UV-Visible spectrum of $[\text{Fe}(\text{Cl}_4\text{Cat})_3]^{3-}$, $[\text{Fe}(\text{Cl}_4\text{Cat})_2(\text{Cl}_4\text{SQ})]^{2-}$, and $\text{Fe}(\text{Cl}_4\text{SQ})_3$ in MeCN. The spectrum of $[\text{Fe}(\text{Cl}_4\text{Cat})(\text{Cl}_4\text{SQ})_2]^-$ is similar to $\text{Fe}(\text{Cl}_4\text{SQ})_3$ in the visible region.

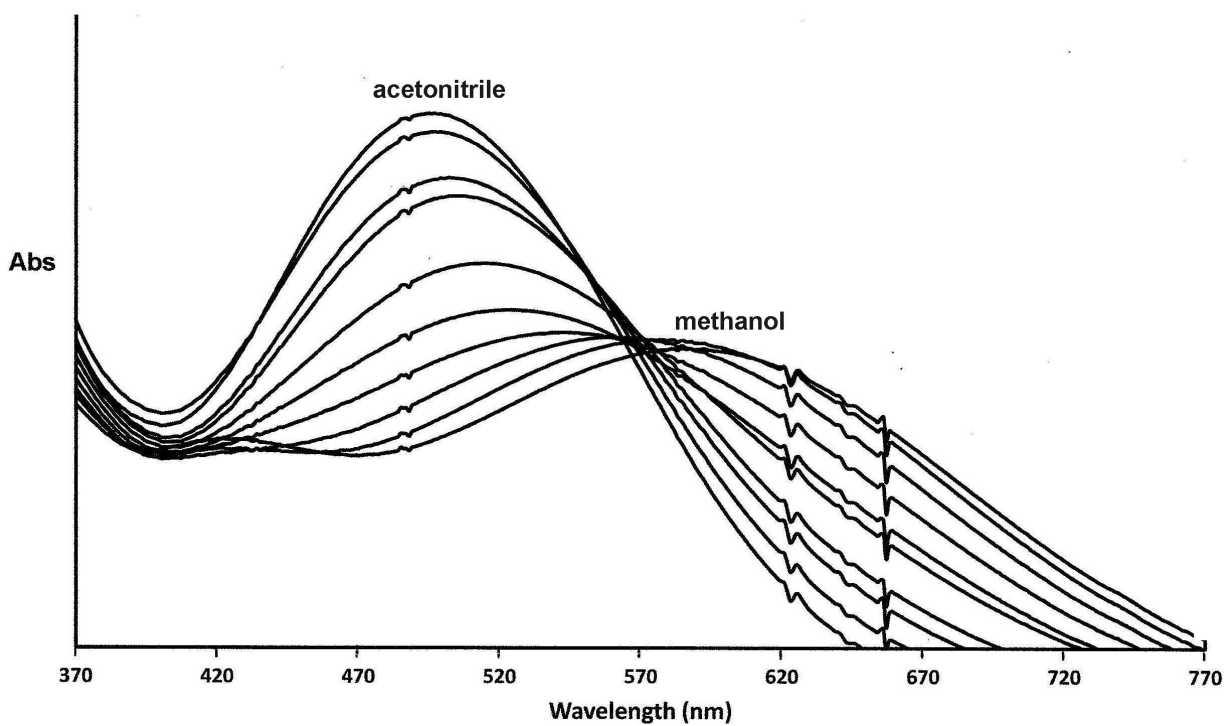


Figure 3.10: UV-Visible spectrum of $[\text{Fe}(\text{Cl}_4\text{Cat})_3]^{3-}$ in MeCN, MeOH, and solutions of varying MeCN:MeOH ratios.

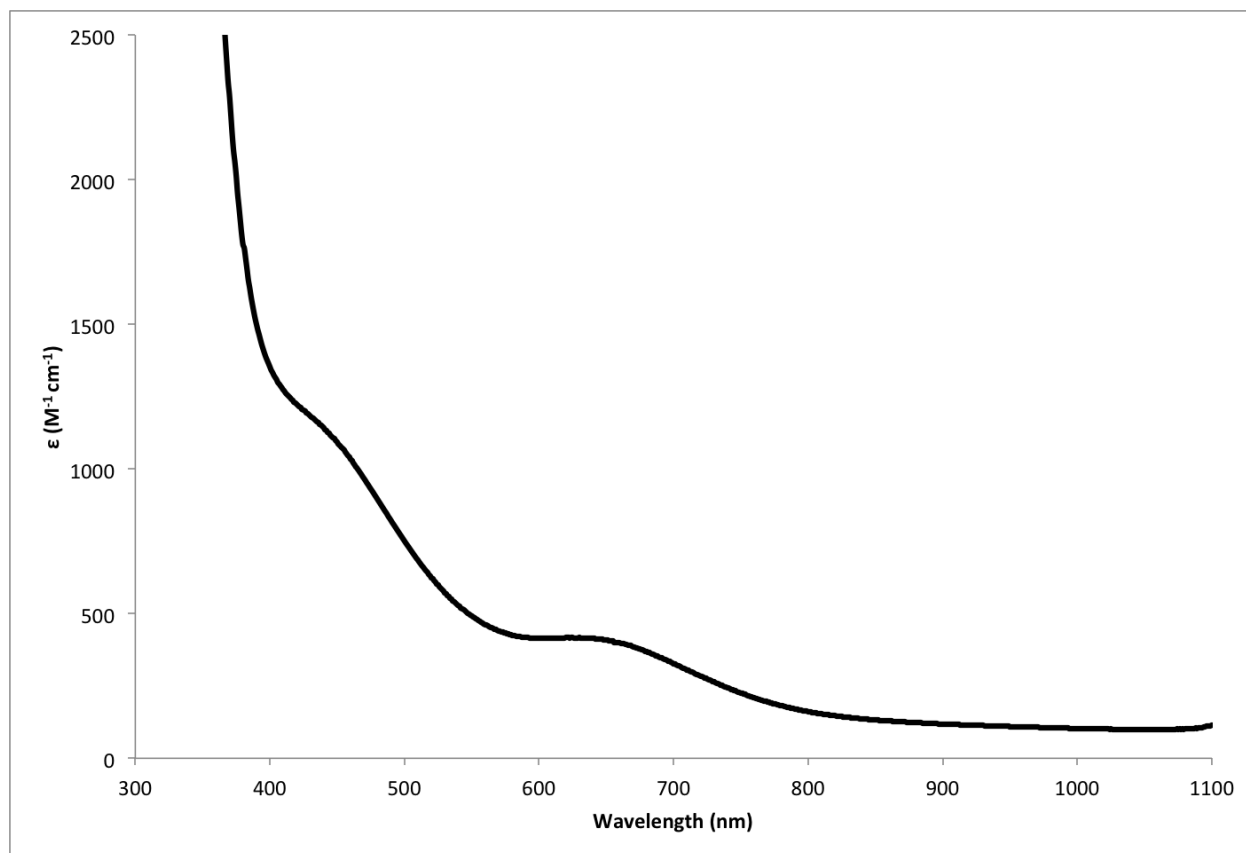


Figure 3.11: UV-Visible spectrum of $(\text{Pr}_4\text{N})_2[\text{Co}(\text{Cl}_4\text{Cat})_2(\text{Cl}_4\text{SQ})]$, 0.001 M in MeCN

coupled mixed-charge ligands of a Class II species.⁷ Peaks in the visible region of the spectrum are still visible at 645 nm and 450 nm (sh) (Figure 3.12) The small shift in λ_{max} from the UV-Visible spectrum is most likely due to solvent effects.

Fourier-transform IR spectroscopy was performed on both $(\text{Pr}_4\text{N})_2[\text{Co}(\text{Cl}_4\text{Cat})_2(\text{Cl}_4\text{SQ})]$ and $(\text{Ph}_4\text{P})_2[\text{Co}(\text{Cl}_4\text{Cat})_2(\text{Cl}_4\text{SQ})]$ so that counter-ion contributions could be identified. The peaks associated with the cobalt complex itself were identified at 1445 cm^{-1} (C-O stretch), and 800 cm^{-1} (C-Cl stretch). The C-O stretch at 1445 cm^{-1} is actually the overlap of the C-O stretches of semiquinone and catechol, seen as a shoulder at 1482 cm^{-1} and broadening of the main peak.

This is more obvious when the FTIR spectra of the cobalt complex and the neutral and trianion iron complexes are overlaid (Figure 3.13). Iron and cobalt have similar masses (55.8 and 58.9 amu, respectively) so there is not a large difference in the FTIR spectrum from changing the metal center, although there is slight shifting of the peaks.⁸⁰ $(\text{Bu}_4\text{N})_3[\text{Fe}(\text{Cl}_4\text{Cat})_3]$ has a C-O peak at approximately 1435 cm^{-1} , while $\text{Fe}(\text{Cl}_4\text{SQ})_3$ has two C-O peaks at 1493 cm^{-1} and 1460 cm^{-1} . These are compared with the $(\text{Pr}_4\text{N})_2[\text{Co}(\text{Cl}_4\text{Cat})_2(\text{Cl}_4\text{SQ})]$ spectrum, as the $(\text{Ph}_4\text{P})_2[\text{Co}(\text{Cl}_4\text{Cat})_2(\text{Cl}_4\text{SQ})]$ spectrum has extra peaks from the Ph_4P^+ counter-ion in the fingerprint region. There is also good agreement with the C-Cl stretch at approximately 800 cm^{-1} .

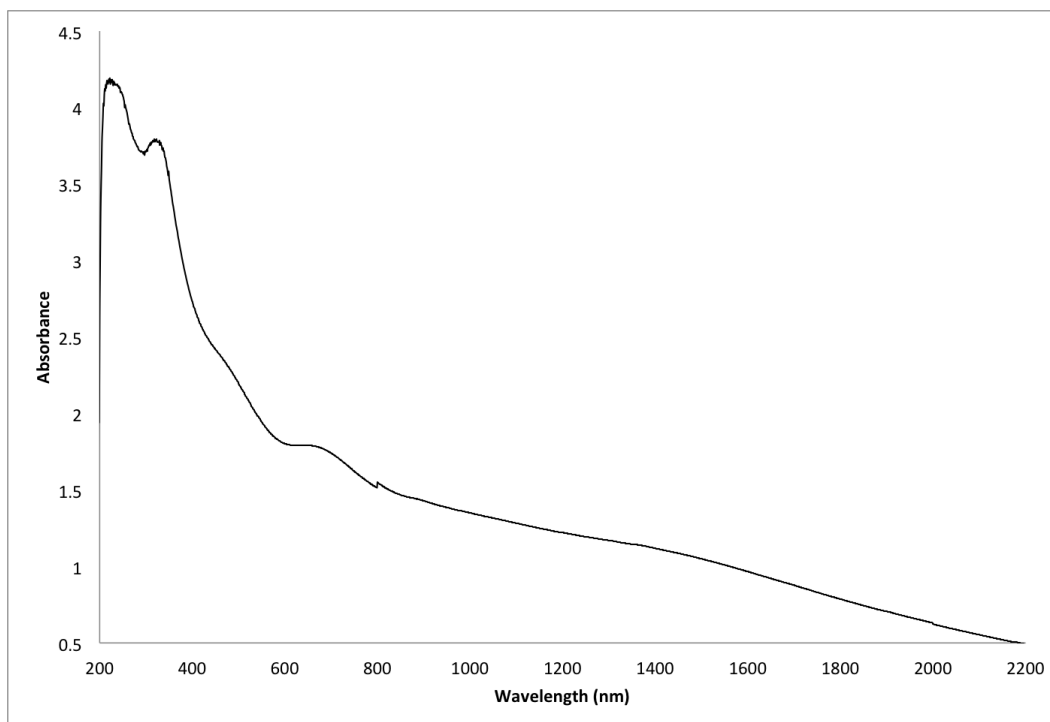


Figure 3.12: Near-IR spectrum of $(\text{Pr}_4\text{N})_2[\text{Co}(\text{Cl}_4\text{Cat})_2(\text{Cl}_4\text{SQ})]$ in KBr pellet from 2200 nm to 200 nm

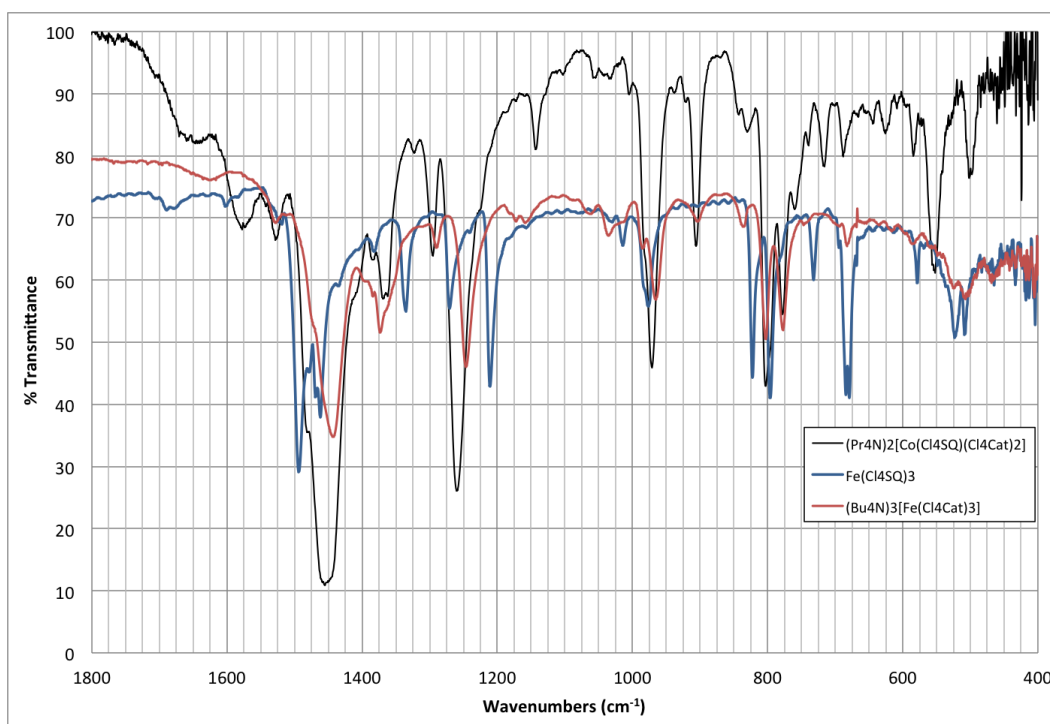


Figure 3.13: Fingerprint region comparative FTIR spectrum of $(\text{Pr}_4\text{N})_2[\text{Co}(\text{Cl}_4\text{Cat})_2(\text{Cl}_4\text{SQ})]$, $\text{Fe}(\text{Cl}_4\text{SQ})_3$, and $(\text{Bu}_4\text{N})_3[\text{Fe}(\text{Cl}_4\text{Cat})_3]$ from 400-1800 cm^{-1}

3.2 Electrochemistry of Complexes

3.2.1 Cyclic Voltammetry of $(\text{Pr}_4\text{N})_2[\text{Mn}(\text{Cl}_4\text{Cat})_3]$

Cyclic voltammetry was performed on $(\text{Pr}_4\text{N})_2[\text{Mn}(\text{Cl}_4\text{Cat})_3]$. The manganese complex has very different electrochemical behavior than the cobalt or iron complexes, in addition to being quite different from the chromium and vanadium analogs. This is due to the properties of the manganese center itself, which is capable of oxidation states from Mn^0 to Mn^{VII} . For iron and cobalt, common oxidation states are +2 and +3, which give d^6 and d^5 iron and d^7 and d^6 cobalt. One issue with the manganese complex is Jahn-Teller distortion, which affects *hs*- Mn^{III} but not Mn^{IV} species.⁸¹ Previous researchers have posited that the tris-tetrachlorocatecholate complex must have Mn^{IV} in order for the catecholate ligands to be bidentate, as the elongation of the *z*-axis in *hs*- Mn^{III} increases the bite distance.^{32,46} However, studies of tris(3,6-di-*tert*-butyl-catecholato)manganese(IV), as well as other manganese-quinone complexes containing N-donor ligands, show that $\text{Mn}^{\text{IV}}(\text{Cat})_3 \rightleftharpoons \text{Mn}^{\text{III}}(\text{Cat})_2(\text{SQ})$ valence tautomerism is possible without ligand dissociation.^{17,20,52} Due to antiferromagnetic coupling between the semiquinone ligands and manganese, these possible redox isomers have the same spin state of $S = 3/2$, so they cannot be differentiated using magnetic experiments. Comparison to cyclic voltammetry of tris(tetrachlorosemiquinonato)chromium(III),⁵⁸ as well as the iron and cobalt analogs, indicates that the CV is well within the potential range to oxidize the catecholate ligands, however, the CV of the manganese complex does not show clear reversible redox couples in DMSO, and only one reversible couple in MeOH.

Figure 3.14 shows CVs of $(\text{Pr}_4\text{N})_2[\text{Mn}(\text{Cl}_4\text{Cat})_3]$ in DMSO at scan rates of 100 mV/s, 25 mV/s, and 10 mV/s. A clear scan rate dependence can be seen, as the reductions appear as one broad peak at 100 mV/s, which then resolves into two peaks at 10 mV/s (Table 3.4).

Figure 3.15 shows $(\text{Pr}_4\text{N})_2[\text{Mn}(\text{Cl}_4\text{Cat})_3]$ CVs by itself and with ferrocene added in DMSO. Interaction between the manganese complex and the ferrocene is evident, as the main reduction peak of $(\text{Pr}_4\text{N})_2[\text{Mn}(\text{Cl}_4\text{Cat})_3]$ at -161 vs $\text{FcCp}_2/\text{FcCp}_2^+$ shifts negative by 130 mV when ferrocene

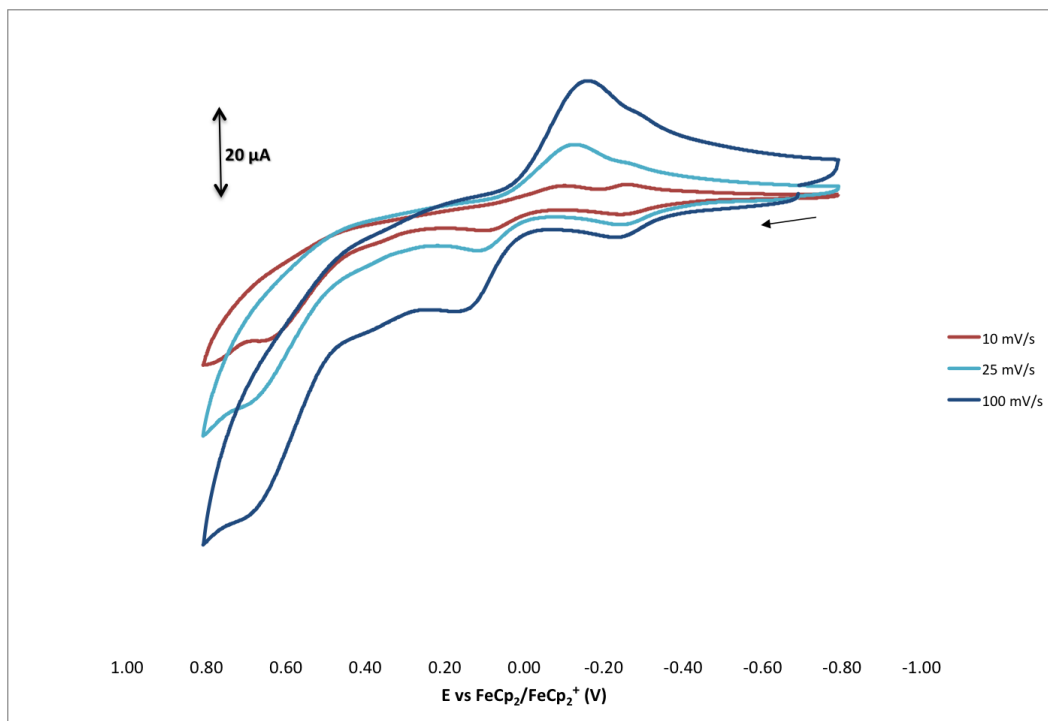


Figure 3.14: Cyclic voltammograms of 1 mM $(\text{Pr}_4\text{N})_2[\text{Mn}(\text{Cl}_4\text{Cat})_3]$ in DMSO vs $\text{FeCp}_2/\text{FeCp}_2^+$ at 10 mV/s, 25 mV/s, and 100 mV/s.

Table 3.4: Forward (E_{pf}) and reverse (E_{pr}) peak potentials of $(\text{Pr}_4\text{N})_2[\text{Mn}(\text{Cl}_4\text{Cat})_3]$ in DMSO at scan rates of 100, 25, and 10 mV/s.

Scan Rate	E_{pf} (mV)	E_{pr} (mV)
100 mV/s	-228	-161
	+175	
25 mV/s	-243	-127
	+117	
10 mV/s	-243	-258
	+102	-100

is present. The ferrocene reduction peak is also affected, appearing broader than the oxidation peak. The first manganese complex oxidation peak at -228 mV is unperturbed, but the second oxidation peak at 175 mV does not appear when ferrocene is present. Surprisingly, the oxidation peak at 689 mV also does not appear when ferrocene is present. The large increase in current for the 689 mV peak, especially at slow scan rates, indicates that it is catalytic. The presence of ferrocenium (as ferrocene has been oxidized at this potential) blocking this implies that the quinone rings are involved in the oxidation, and the ferrocenium shifts this potential outside the stable range of the DMSO/(Bu₄N)(PF₆).

At slow scan rates in DMSO (Figure 3.16) the main reduction peak resolves into two separate reduction peaks. In terms of peak-to-peak separation, however, for the more negative "couple" $\Delta E_p = 15$ mV, and for the more positive "couple" $\Delta E_p = 202$ mV. These values are both outside of the reversibility range, although the $+102/-100$ mV couple could qualify as quasireversible.

In methanol, the manganese complex exhibits quite different electrochemical behavior (Figure 3.17). There is still a dependence on scan rate, however, there is also an observable reversible couple at -154 mV, as well as a quasireversible couple at approximately -20 mV. Due to its quasireversible nature, the -20 mV couple's $E_{1/2}$ and ΔE_p have more of a scan-rate dependence than the reversible couple (Table 3.5). Figure 3.18 illustrates this reversibility by separating the overlapping couples, going from -446 mV to -97 mV vs FeCp₂/FeCp₂⁺ and returning, which shows that the first oxidation peak is coupled with the reduction peak. Figure 3.18 also shows that the quasireversible peaks are coupled, by going to $+183$ mV vs FeCp₂/FeCp₂⁺, giving two reduction peaks.

There appears to be another couple at approximately 200 mV, however, the current is less than for the other two couples. This indicates that the third couple is either very slow kinetically, or that it is another electroactive species present in solution at a lower concentration. The increased prominence of this couple at slow scan rates indicates that there is a kinetic factor, however, experiments in differential pulse voltammetry (Section 3.2.2) indicate that it is another electroactive species, probably a bis(tetrachlorocatecholato)manganese complex. Synthesis of the bis species

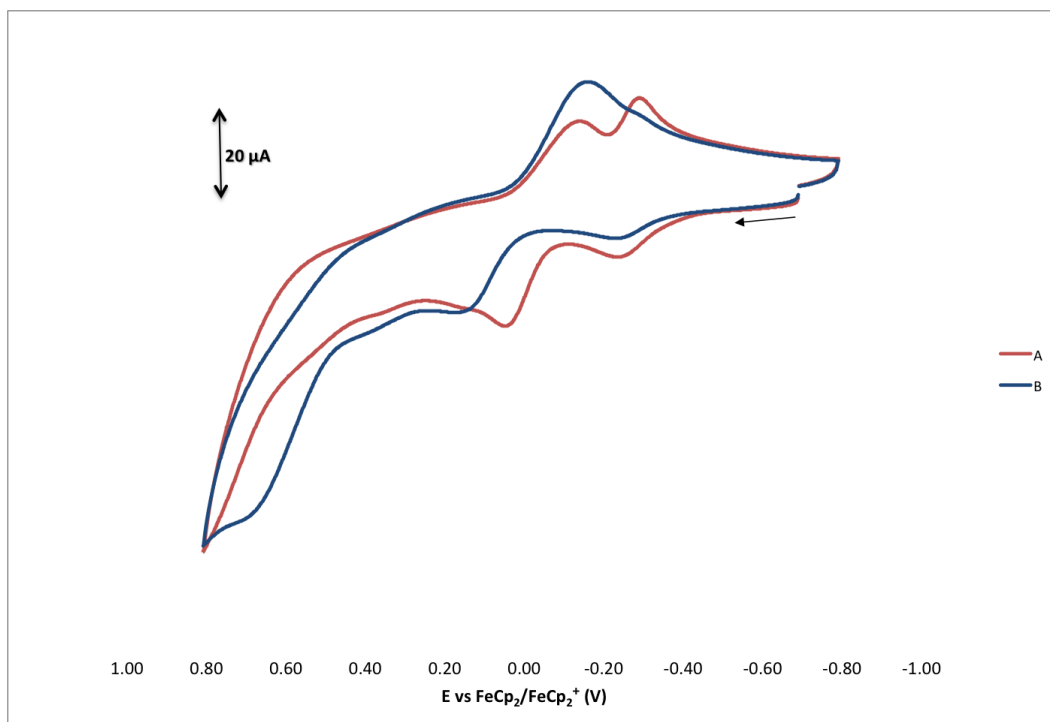


Figure 3.15: Cyclic voltammograms of (A) 1 mM $(\text{Pr}_4\text{N})_2[\text{Mn}(\text{Cl}_4\text{Cat})_3]$ with 0.5 mM ferrocene and (B) 1 mM $(\text{Pr}_4\text{N})_2[\text{Mn}(\text{Cl}_4\text{Cat})_3]$ in DMSO vs $\text{FeCp}_2/\text{FeCp}_2^+$ at 100 mV/s.

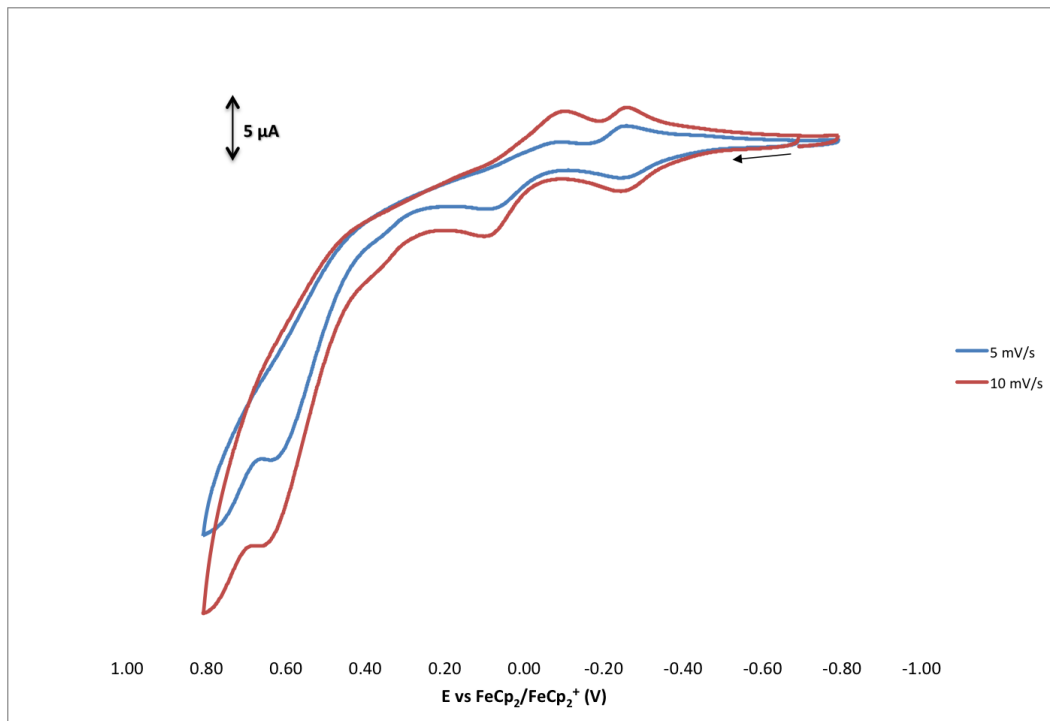


Figure 3.16: Cyclic voltammograms of 1 mM $(\text{Pr}_4\text{N})_2[\text{Mn}(\text{Cl}_4\text{Cat})_3]$ in DMSO vs $\text{FeCp}_2/\text{FeCp}_2^+$ at 5 mV/s and 10 mV/s.

has been performed by Sheriff⁴⁶ in wet ethanol, yielding $(\text{Bu}_4\text{N})[\text{Mn}^{\text{III}}(\text{Cl}_4\text{Cat})_2\text{H}_2\text{OEtOH}]$. In this case, a more labile semiquinone ligand could be replaced by methanol. Because this is a reversible dissociation (Ruiz reports that the tris complex may be formed from oxidation of the bis complex³²) it is not possible to definitively determine whether the 200 mV couple is from a bis(tetrachlorosemiquinonato) species, or a $\text{Mn}(\text{Cl}_4\text{Cat})(\text{Cl}_4\text{SQ})_2 \rightleftharpoons [\text{Mn}(\text{Cl}_4\text{SQ})_3]^+$ couple. However, differential pulse voltammetry, as well as the clear difference in peak current, indicates that ligand dissociation may occur in MeOH and the quasireversible 200 mV couple may be attributed to the resulting bis complex.

Table 3.5: Forward (E_{pf}) and reverse (E_{pr}) peak potentials, peak-to-peak separation (ΔE_p), and couple potentials ($E_{1/2}$) of $(\text{Pr}_4\text{N})_2[\text{Mn}(\text{Cl}_4\text{Cat})_3]$ in MeOH at scan rates of 100, 25, and 10 mV/s.

Scan Rate	E_{pf} (mV)	E_{pr} (mV)	ΔE_p (mV)	$E_{1/2}$ (mV)
100 mV/s	-117	-190	73	-154
	+120	-120	240	0
	+295	+100	195	+198
25 mV/s	-120	-190	70	-155
	+170	-115	185	-23
	+285	+100	185	+193
10 mV/s	-120	-175	55	-148
	+40	-95	135	-28
	+280	+130	150	+205

The solvent dependence is also observed with the cobalt and iron analogs (Sections 3.2.3 and 3.2.5). One feature is that the cyclic voltammogram becomes more compressed in MeOH, with the two most prominent oxidation/reduction peaks at a maximum difference of 215 mV in MeOH and 360 mV in DMSO at 10 mV/s (Figure 3.19). This is due in part to the different diffusivity in the different solvents, but also to interaction of the solvent with the quinone rings. While MeOH is less polar than DMSO, it is also a protic solvent, which allows interaction with the chelated oxygens. This affects the electrochemistry by decreasing electron transfer between ligands, which means that the couple potentials are closer together as the complex becomes more Class I in nature. Calculations of K_{com} for the manganese complex in MeOH at 10 mV/s gives $K_{com} = 1.1 \cdot 10^2$ for the -148/ -28 mV couples. In DMSO, the oxidation and reduction peaks are

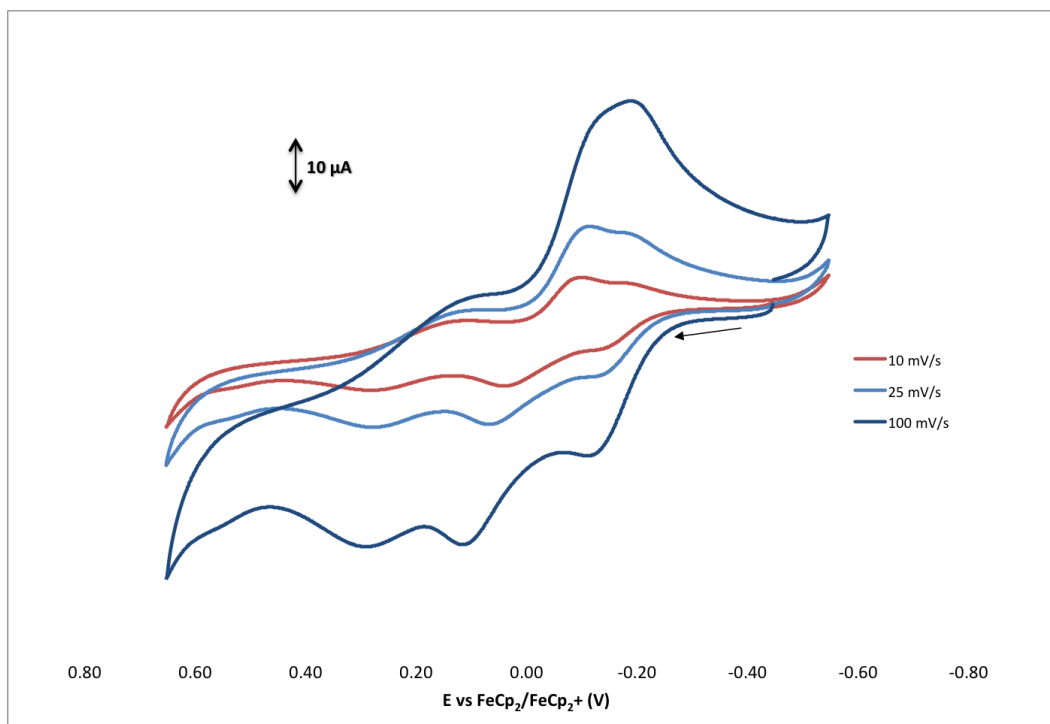


Figure 3.17: Cyclic voltammograms of 1 mM $(\text{Pr}_4\text{N})_2[\text{Mn}(\text{Cl}_4\text{Cat})_3]$ in MeOH vs $\text{FeCp}_2/\text{FeCp}_2^+$ at 10 mV/s, 25 mV/s, and 100 mV/s.

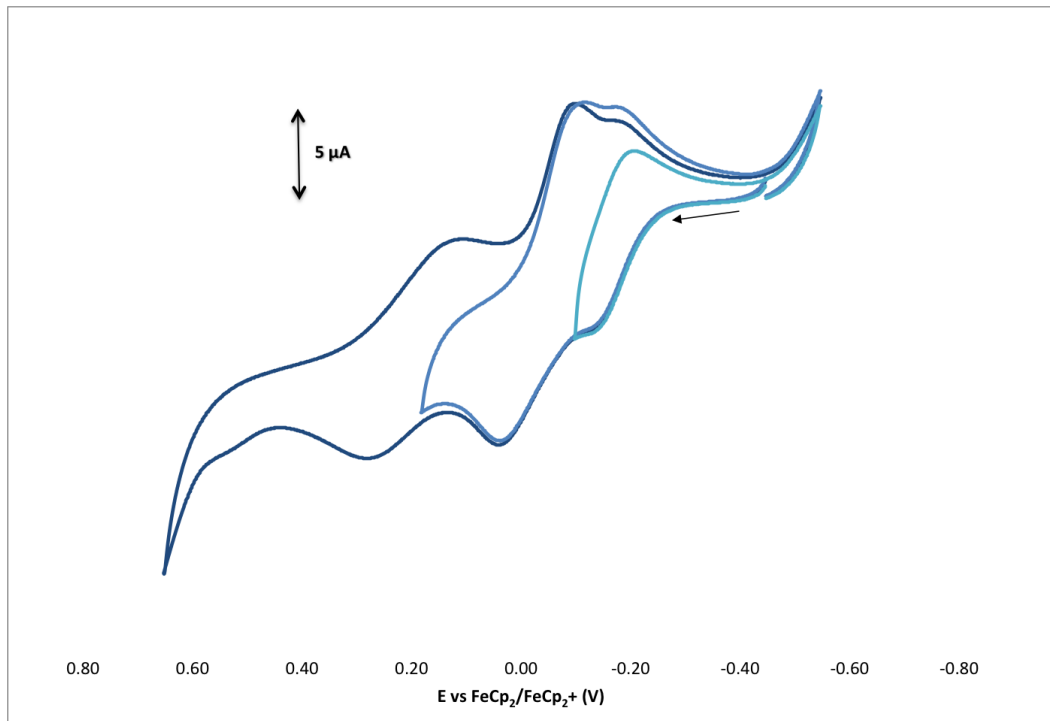
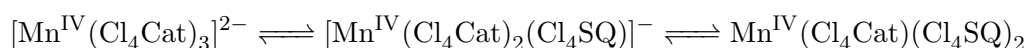


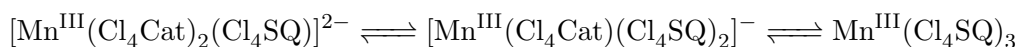
Figure 3.18: Cyclic voltammograms of 1 mM $(\text{Pr}_4\text{N})_2[\text{Mn}(\text{Cl}_4\text{Cat})_3]$ in MeOH vs $\text{FeCp}_2/\text{FeCp}_2^+$ at 10 mV/s.

not clearly coupled, however, an estimate may be made by assuming that the two oxidation and two reduction peaks observed at 10 mV/s correspond to two couples, at +1 mV and -250 mV. From this, $K_{com} = 1.6 \cdot 10^4$. While the overall electrochemical behavior in DMSO is not as clear as in MeOH, the effect on comproportionation can be estimated, and the complex behaves more as a Class I/Class II compound in the protic solvent.

In terms of the redox series, this would correspond to a three-membered redox series observed in both MeOH and DMSO:



This assumes, however, that valence tautomerism is not a factor. Another possible redox series would be:



It is possible that all six of these redox isomers could exist in solution. Catecholate ligands are strong pi-donors that may stabilize high-valent Mn^{IV} , but a neutral species with three semiquinone ligands may be more favorable than a neutral species with the mixed-valence combination of one catechol and two semiquinone ligands.

A final oxidation to $[\text{Mn}^{\text{IV}}(\text{Cl}_4\text{SQ})_3]^+$ or $[\text{Mn}^{\text{III}}(\text{Cl}_4\text{BQ})(\text{Cl}_4\text{SQ})_2]^+$ is not observed in DMSO. This supports the assignment of the quasireversible +200 mV couple in MeOH to the formation of an electrochemically active bis species.

3.2.2 Differential Pulse Voltammetry of $[\text{Mn}(\text{Cl}_4\text{Cat})_3]^{2-}$

Differential pulse voltammetry on $[\text{Mn}(\text{Cl}_4\text{Cat})_3]^{2-}$ is somewhat illuminating in determining potentials for the couples. For DMSO, a kinetic aspect is clearly present when comparing DPV, as seen in Figures 3.20 and 3.21, which have an effective scan rate of 100 mV/s and 3 mV/s, respectively. As in the CV, the reduction peaks don't resolve until the effective scan rate is quite slow, which is similar to the iron complex (Sections 3.2.3 and 3.2.4). In the faster effective scan

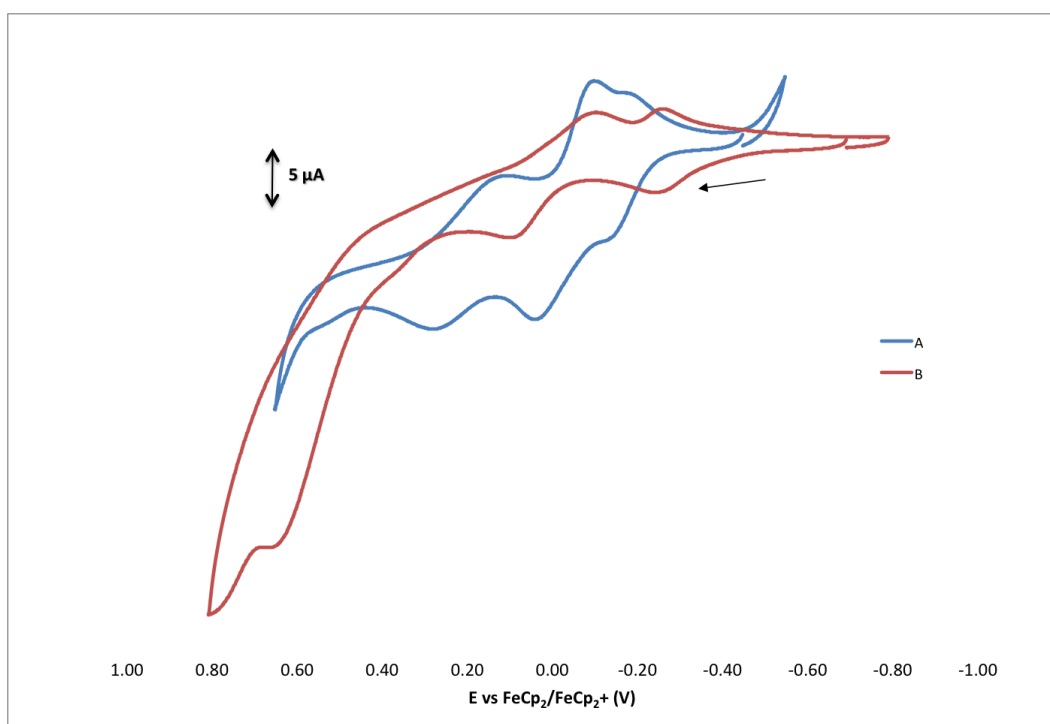
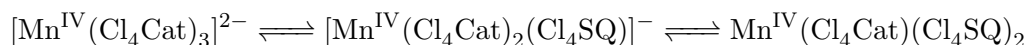
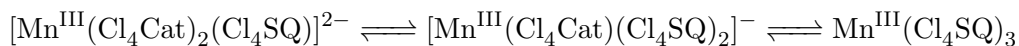


Figure 3.19: Cyclic voltammograms of 1 mM $(\text{Pr}_4\text{N})_2[\text{Mn}(\text{Cl}_4\text{Cat})_3]$ in (A) MeOH and (B) DMSO vs $\text{FeCp}_2/\text{FeCp}_2^+$ at 10 mV/s.

rate, only one peak appears in the reductive voltammogram (at -95 mV), while at the slower effective scan rate, two separate reductive peaks appear (at -301 mV and $+95$ mV). Peak fitting on the reduction peaks in Figure 3.21, using Igor Pro's Multipeak fitting 2 package, gives ΔE_p of 114 mV and 95 mV for the -247 mV peak and $+53$ mV peak, respectively. From this it's reasonable to assume that these peaks each correspond to a one-electron transfer. The -247 mV peak is also much more prominent in DPV, which implies kinetic limitations in electron transfer. This is supported by the CV, where the two oxidation and reduction peaks become clear only at very slow scan rates. Oddly, the oxidation peaks appear of equal magnitude at an effective scan rate of 100 mV/s, while at the slower effective scan rate of 3 mV/s the initial peak is much more prominent. Similarly, at the reductive peak at $+53$ mV is less in magnitude than the -247 mV peak at the effective scan rate of 3 mV/s. However, at an effective scan rate of 3 mV/s, the differential pulse voltammograms appear almost as mirrors of each other, indicating that the oxidations and reductions are happening at similar potentials. As before, this may be assigned to the series:



Or:



Calculations for K_{com} , assuming that the peaks in Figure 3.21 are coupled, gives $K_{com} = 2.3 \cdot 10^5$, which would place this complex as Class II in DMSO.

Peak fitting on Figure 3.20 gives just two one-electron oxidations at -301 mV and $+95$ mV, and while the reduction peak at -95 mV is too broad to be a simple two-electron reduction, this can again be assigned to kinetics, and as the reduction peak has a FWHM of 197 mV, it is likely that this is two one-electron couples that are close in E° but have an interaction with each other at the electrode's surface. This is also supported by the behavior of the complex when ferrocene is present, which interferes with that interaction, causing a peak shift (Figure 3.15).

Differential pulse voltammetry in methanol also has some unusual features (Figure 3.22). The clearly reversible couple from cyclic voltammetry is readily apparent at -160 mV, with the expected

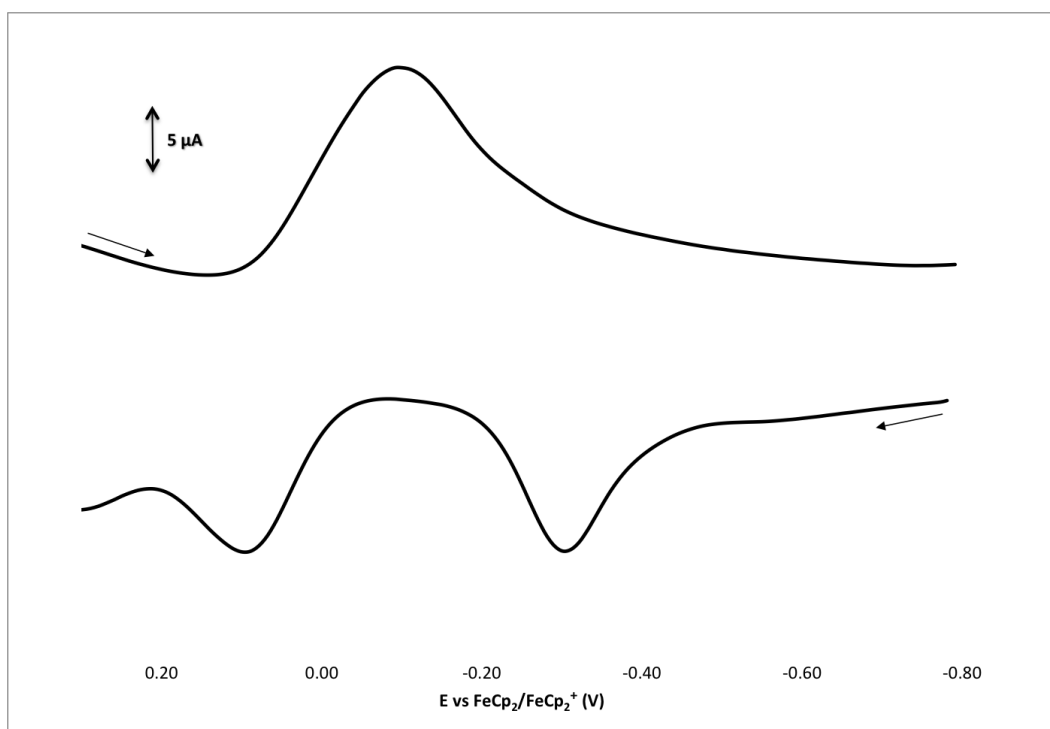


Figure 3.20: Differential pulse voltammograms of $(\text{Pr}_4\text{N})_2[\text{Mn}(\text{Cl}_4\text{Cat})_3]$ in DMSO vs $\text{FeCp}_2/\text{FeCp}_2^+$ at an effective scan rate of 100 mV/s. Pulse width = 50 ms, Pulse period = 100 ms, Step potential = 10 mV, Pulse amplitude = 50 mV.

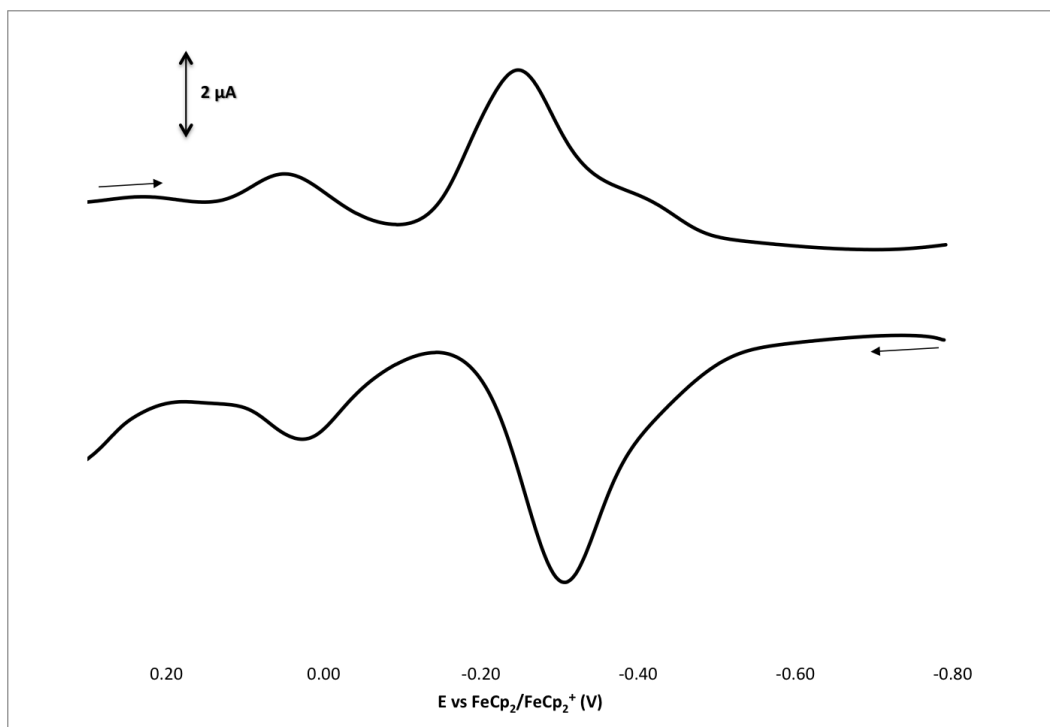
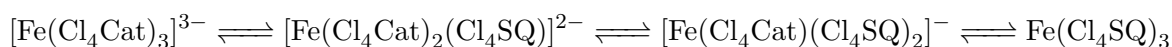


Figure 3.21: Differential pulse voltammograms of $(\text{Pr}_4\text{N})_2[\text{Mn}(\text{Cl}_4\text{Cat})_3]$ in DMSO vs $\text{FeCp}_2/\text{FeCp}_2^+$ at an effective scan rate of 3 mV/s. Pulse width = 300 ms, Pulse period = 600 ms, Step potential = 2 mV, Pulse amplitude = 50 mV.

ΔE_p of 10 mV, equal to the pulse amplitude. However, the quasireversible couple seen in the CV at approximately -28 mV appears here with a current similar to the reversible couple, but with an uneven and broadened peak, at approximately -65 mV. The couple previously assigned to a bis species generated in situ appears reversibly at $+230$ mV. It clearly has much less amplitude than the other two couples, and here the case that a bis species is formed through reversible ligand oxidation and dissociation is strengthened. Reversible ligand dissociation would explain why the couple at -65 mV has an unusual shape, as the tris complex does not maintain a constant concentration due to formation of the bis species. The same three-membered redox series would apply, as in DMSO, as the concentration of the bis species does not approach that of the tris species, hence the reduced current magnitude of the $+230$ mV couple. Calculating the comproportionation constant between the dianion and neutral forms gives $K_{com} = 40$, making the manganese complex Class I in MeOH.

3.2.3 Cyclic voltammetry of $[\text{Fe}(\text{Cl}_4\text{Cat})_3]^{3-}$

Cyclic voltammetry was performed on $(\text{Bu}_4\text{N})_3[\text{Fe}(\text{Cl}_4\text{Cat})_3]$ and $\text{Fe}(\text{Cl}_4\text{SQ})_3$, which have the same cyclic voltammograms. The iron complex has unique electrochemical properties, specifically, it has three clear oxidative peaks, similar to the chromium analog, but only one clear reductive peak. It is only at very slow scan rates that three reductive peaks become clear. In DMSO, the oxidation peaks are at -226 mV, 119 mV, and 404 mV vs Fc/Fc^+ (Figure 3.23). These can be assigned to the redox series:



At 25 mV/s, only one reduction peak is clear, but when slowed to 5 mV/s and 2 mV/s, each oxidation peak has a matching reduction peak. As with the manganese complex, the iron has different reduction kinetics than oxidation kinetics. This could be due to pi-stacking interactions, as addition of ferrocene causes the first oxidation peak to lose amplitude and the second to disappear (Figure 3.24). The reduction peak remains, but it, too, has lost amplitude. The capacitive current, on the other hand, has diminished, and the reduction coupled with the last oxidation, while still

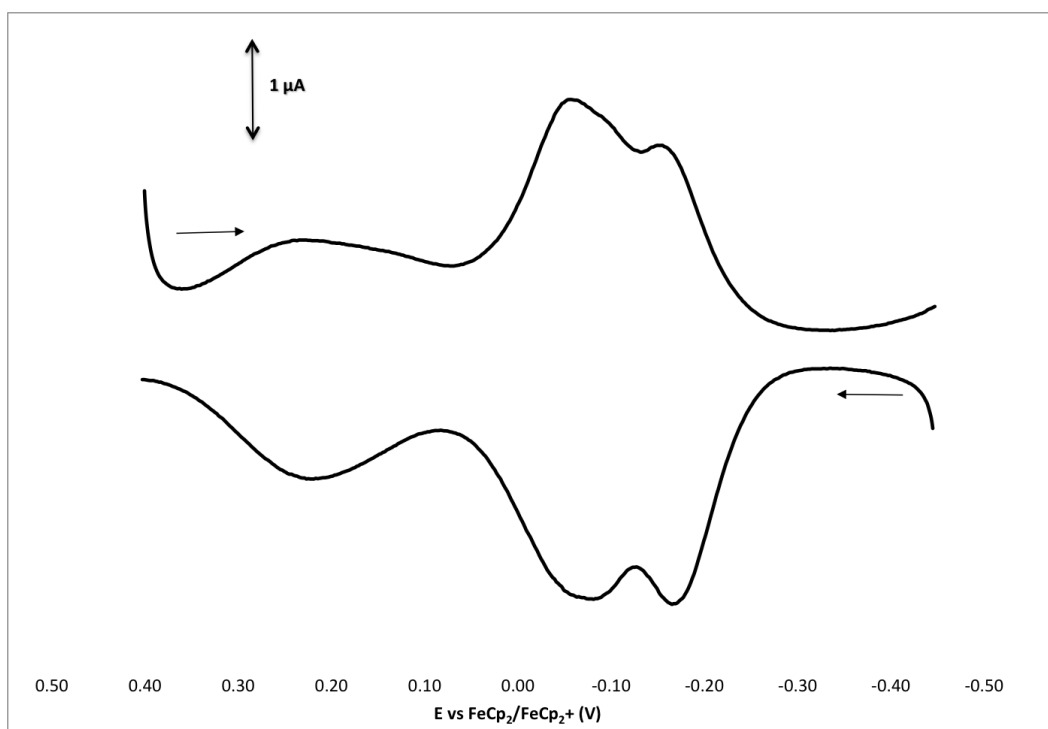


Figure 3.22: Differential pulse voltammograms of $(\text{Pr}_4\text{N})_2[\text{Mn}(\text{Cl}_4\text{Cat})_3]$ in MeOH vs $\text{FeCp}_2/\text{FeCp}_2^+$ at an effective scan rate of 3 mV/s. Pulse width = 300 ms, Pulse period = 600 ms, Step potential = 2 mV, Pulse amplitude = 10 mV.

not a clear peak, is more defined. This implies that the reduction of the iron complex is spread out over the range of about 560 mV to -360 mV, with the peak at -292 mV the equivalent of a 3-electron reduction as all oxidized species are reduced.

Assigning reduction peak potentials using the 5 mV/s CV, the $E_{1/2}$ of these couples are at 349 mV, 62 mV, and -259 mV. The ΔE_p of the -259 mV couple is 65 mV, close to the ideal $59/n$, but the 349 mV and 62 mV couples have a larger ΔE_p of 90 mV and 85 mV, respectively. This is consistent with slow electron transfer. As scan rate increases, the ΔE_p of the -259 mV couple also increases, giving $\Delta E_p = 100$ mV at 25 mV/s, although the $E_{1/2}$ does not shift, as expected for a reversible couple.

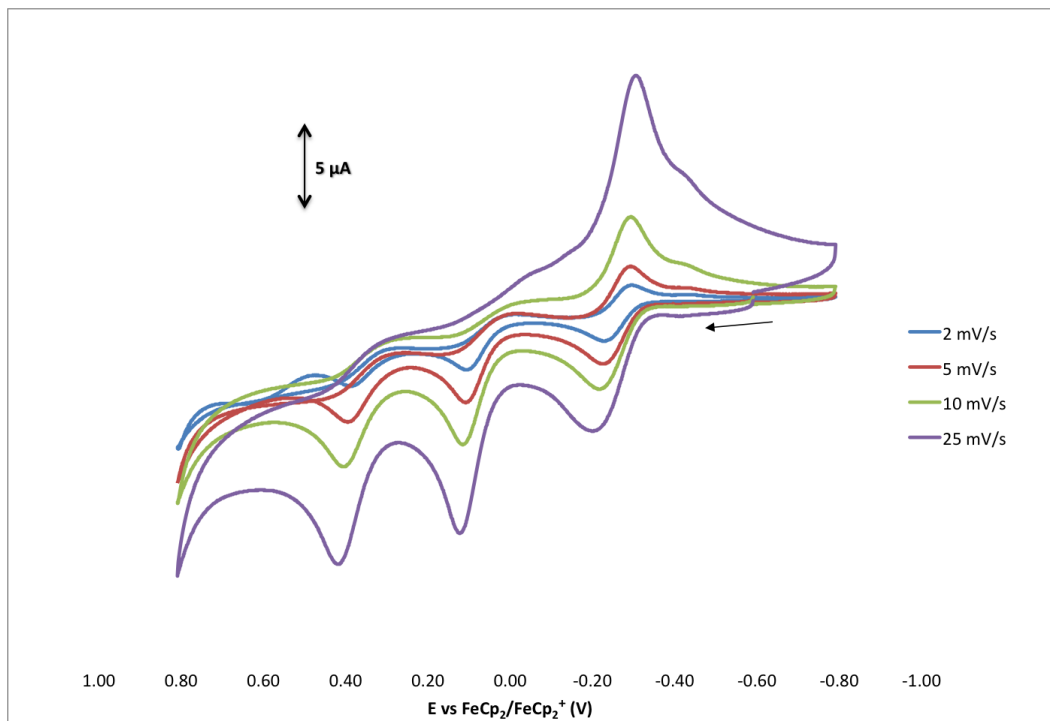


Figure 3.23: Cyclic voltammograms of 1 mM $(\text{Bu}_4\text{N})_3[\text{Fe}(\text{Cl}_4\text{Cat})_3]$ in DMSO vs $\text{FeCp}_2/\text{FeCp}_2^+$.

In MeOH, the iron complex shows the same electrochemical profile as in DMSO. Figure 3.25 shows CVs of $(\text{Bu}_4\text{N})_3[\text{Fe}(\text{Cl}_4\text{Cat})_3]$ in MeOH at scan rates from 25 mV/s to 1 mV/s. These voltammograms show how narrow the potential range for the iron redox series is (all the couples are within approximately 0.5 V), as well as the scan rate dependence of the reductions. Figure 3.26

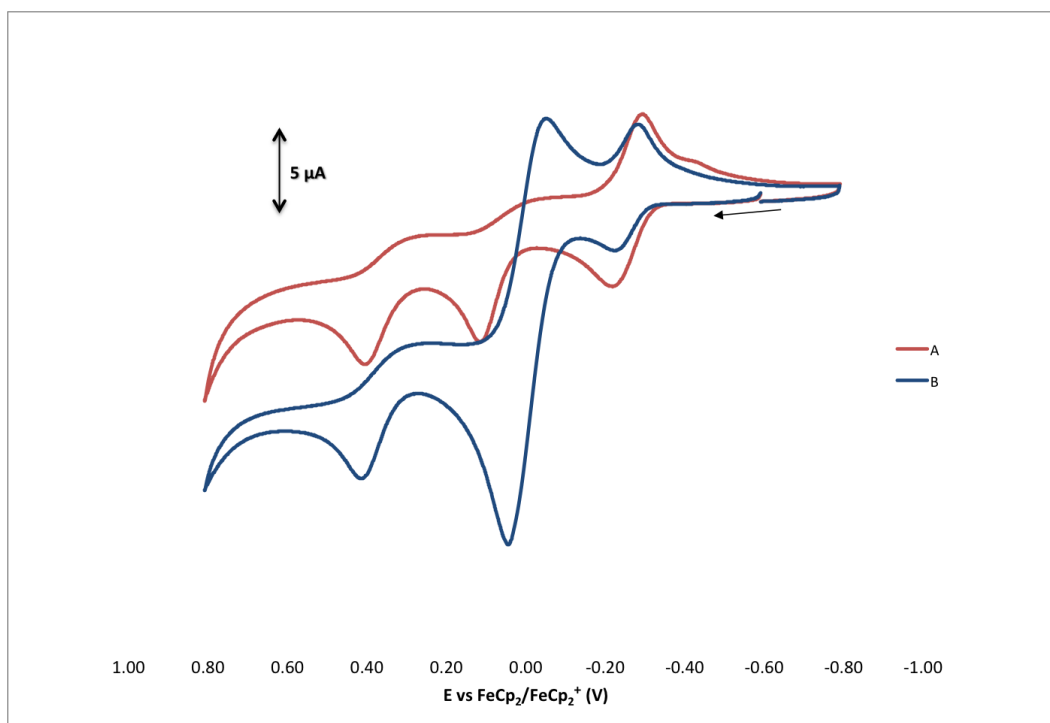


Figure 3.24: Cyclic voltammograms at 10 mV/s of (A) 1 mM $(\text{Bu}_4\text{N})_3[\text{Fe}(\text{Cl}_4\text{Cat})_3]$ and (B) 1 mM $(\text{Bu}_4\text{N})_3[\text{Fe}(\text{Cl}_4\text{Cat})_3]$ with 1.7 mM ferrocene in DMSO vs $\text{FeCp}_2/\text{FeCp}_2^+$. The most prominent couple in (B) is ferrocene.

illustrates the very slow scan rates required to distinguish the individual reduction peaks. From the 1 mV/s CV, ligand based reduction couples appear at 231 mV, 73 mV, and -103 mV vs $\text{FeCp}_2/\text{FeCp}_2^+$.

Because the iron complex has been synthesized as both $\text{Fe}(\text{Cl}_4\text{SQ})_3$ and $(\text{Bu}_4\text{N})_3[\text{Fe}(\text{Cl}_4\text{Cat})_3]$, UV-Visible spectral data for these complexes may be compared to a spectroelectrochemical series (Figure 3.27). As discussed in Section 3.1.4.2, the neutral complex, $\text{Fe}(\text{Cl}_4\text{SQ})_3$, and the monoanion, $[\text{Fe}(\text{Cl}_4\text{Cat})(\text{Cl}_4\text{SQ})_2]^-$, have nearly identical electronic spectra. Each member of the redox series is observed, with characteristic λ_{max} as indicated.

3.2.4 Differential pulse voltammetry of $[\text{Fe}(\text{Cl}_4\text{Cat})_3]^{3-}$

Differential pulse voltammetry was performed on $(\text{Bu}_4\text{N})_3[\text{Fe}(\text{Cl}_4\text{Cat})_3]$ in DMSO and MeOH. Like the manganese complex, DPV still shows scan rate dependence. In DMSO, at an effective scan rate of 20 mV/s (Figure 3.28), two small reductions are visible at approximately 410 mV and 120 mV, but the reduction is dominated by a large peak at -289 mV. However, at an effective scan rate of 3 mV/s, three clear reduction peaks are apparent to match the three oxidation peaks. Peak fitting using Igor Pro Multiplex fitting 2 package gives the results in Table 3.6. This shows that there are three one-electron couples, reversible at slow scan rates, corresponding to $[\text{Fe}(\text{Cl}_4\text{Cat})_3]^{3-} \rightleftharpoons [\text{Fe}(\text{Cl}_4\text{Cat})_2(\text{Cl}_4\text{SQ})]^{2-}$, $[\text{Fe}(\text{Cl}_4\text{Cat})_2(\text{Cl}_4\text{SQ})]^{2-} \rightleftharpoons [\text{Fe}(\text{Cl}_4\text{Cat})(\text{Cl}_4\text{SQ})_2]^-$, and $[\text{Fe}(\text{Cl}_4\text{Cat})(\text{Cl}_4\text{SQ})_2]^- \rightleftharpoons \text{Fe}(\text{Cl}_4\text{SQ})_3$ respectively. Further, the peak-to-peak separation for all of these couples is approximately 50 mV, the pulse amplitude.

Table 3.6: E_p , $\Delta E_{p/2}$, and $E_{1/2}$ from DPV of the iron complex in DMSO, as found using the Multiplex Fitting 2 package in Igor Pro. Effective scan rate = 3 mV/s

Oxidation		Reduction		
E_p (mV)	$\Delta E_{p/2}$ (mV)	E_p (mV)	$\Delta E_{p/2}$ (mV)	$E_{1/2}$ (mV)
-333	93	-287	85	-310
46	92	101	90	74
324	112	373	109	349

From these values, K_{com} can be calculated. For the $E_{-3/-1}$ couples, $K_{com} = 2.97 \cdot 10^6$, and

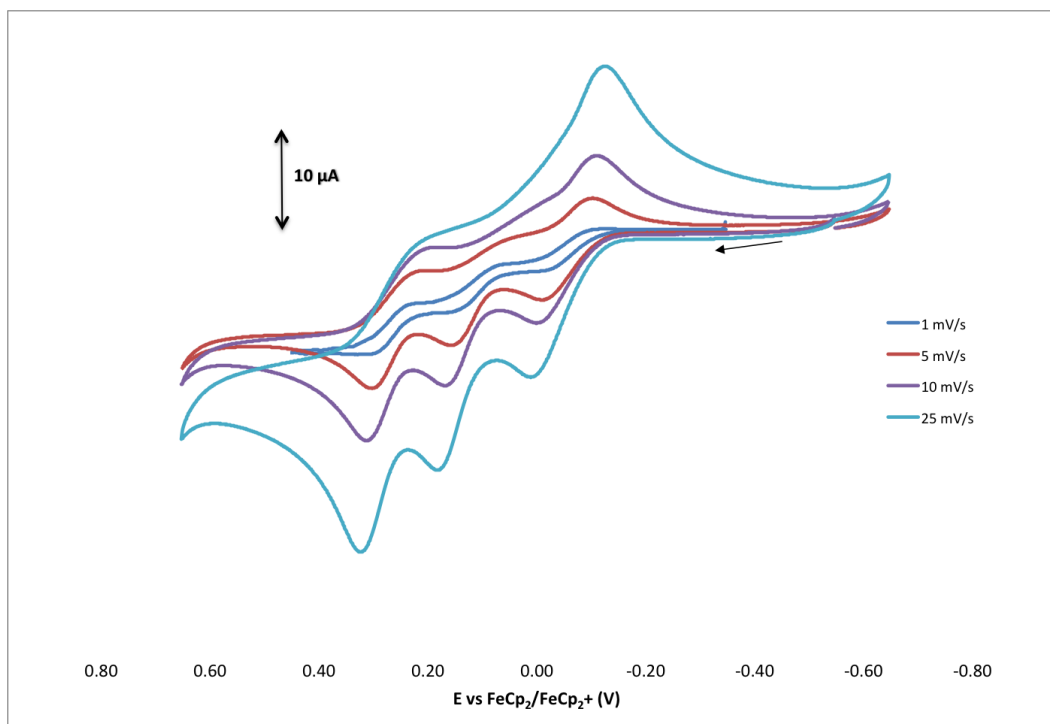


Figure 3.25: Cyclic voltammograms of 1 mM $(\text{Bu}_4\text{N})_3[\text{Fe}(\text{Cl}_4\text{Cat})_3]$ in MeOH at scan rates of 25 mV/s, 10 mV/s, 5 mV/s, and 1 mV/s.

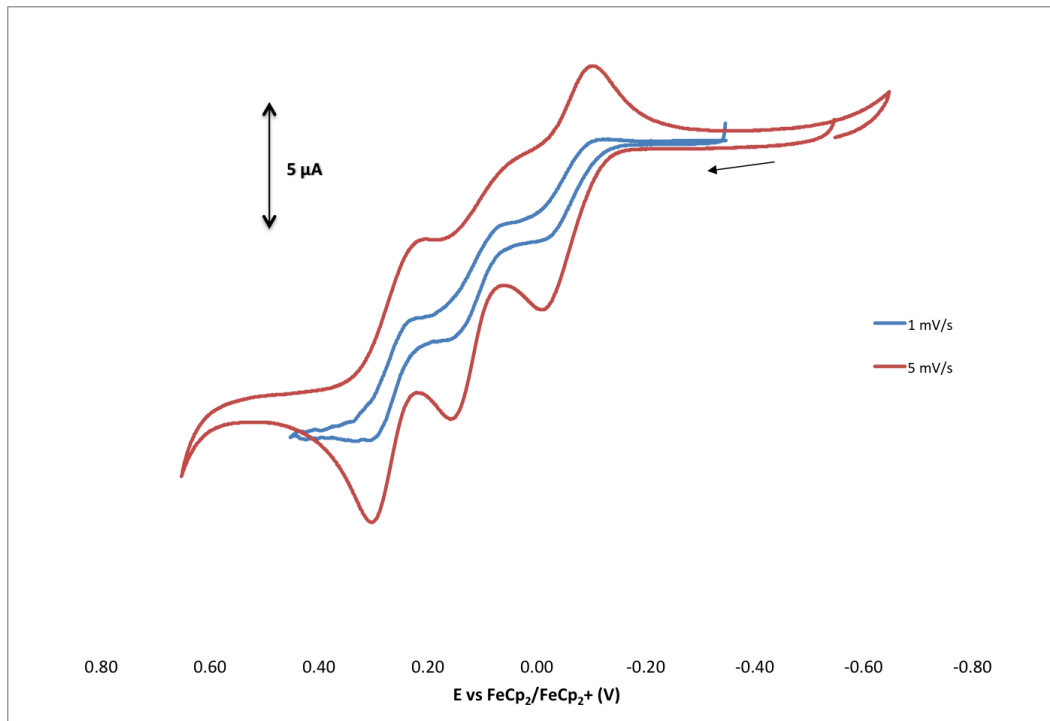


Figure 3.26: Cyclic voltammograms of 1 mM $(\text{Bu}_4\text{N})_3[\text{Fe}(\text{Cl}_4\text{Cat})_3]$ in MeOH at scan rates of 5 mV/s and 1 mV/s.

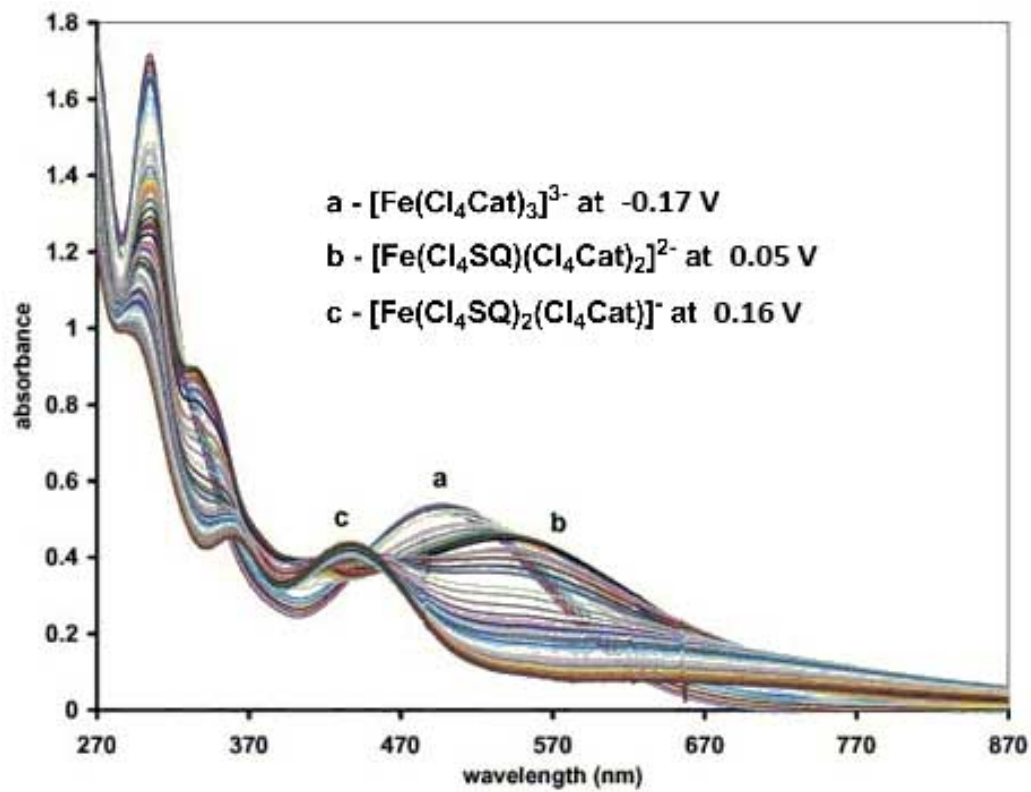


Figure 3.27: Electronic spectra on members of the $[\text{Fe}(\text{Cl}_4\text{Q})_3]^{n-}$ ($n = 1 - 3$) redox series obtained in spectroelectrochemical measurements beginning with $\text{Fe}(\text{Cl}_4\text{SQ})_3$ in acetonitrile solution containing 0.10 M $(\text{NBu}_4)(\text{PF}_6)$ as electrolyte. Potentials referenced to $\text{FeCp}_2/\text{FeCp}_2^+$. Peaks correspond to (a) $[\text{Fe}(\text{Cl}_4\text{Cat})_3]^{3-}$ at -0.17 V, (b) $[\text{Fe}(\text{Cl}_4\text{Cat})_2(\text{Cl}_4\text{SQ})]^{2-}$ at 0.05 V, and (c) $[\text{Fe}(\text{Cl}_4\text{Cat})(\text{Cl}_4\text{SQ})_2]^{-}$ at 0.16 V.

for the $E_{-2/0}$ couples, $K_{com} = 4.44 \cdot 10^4$. This gives Class II bordering on Class III for the $E_{-3/-1}$ couples and Class II for the $E_{-2/0}$ couples, which helps explain why the -310 mV couple has a larger current. The separation between the monoanion and trianion is distinct (Class III), but once oxidized to the dianion, there's a Class II relationship between that and the neutral complex. This causes the electron transfer kinetics to overlap more and gives less distinct redox peaks.

This relationship is more apparent in MeOH (Figures 3.30 and 3.31). At an effective scan rate of 20 mV/s, all three oxidation peaks are clear. The reduction peaks are observed as one at +329 mV, followed by a ramp up to a larger peak at -75 mV which corresponds to the three-electron reduction observed at faster scan rates in cyclic voltammetry. At an effective scan rate of 3 mV/s, three distinct reduction peaks are observed to match the three oxidation peaks (Table 3.7).

Table 3.7: E_p , $\Delta E_{p/2}$, and $E_{1/2}$ from DPV of the iron complex in MeOH, as found using the Multipeak Fitting 2 package in Igor Pro. Effective scan rate = 3 mV/s

Oxidation		Reduction		
E_p (mV)	$\Delta E_{p/2}$ (mV)	E_p (mV)	$\Delta E_{p/2}$ (mV)	$E_{1/2}$ (mV)
-58	106	-51	103	-55
119	100	134	127	127
270	85	297	88	284

Calculating K_{com} with these values gives $K_{com} = 1.2 \cdot 10^3$ for the $E_{-3/-1}$ couples, and $K_{com} = 4.5 \cdot 10^2$ for the $E_{-2/0}$ couples. This confirms the trend from DPV in DMSO, as the $E_{-2/0}$ couples have more charge localization for both solvents than the $E_{-3/-1}$ couples. In MeOH, the complex behaves as Class I for all couples, continuing the trend of the protic solvent inhibiting electron transfer between ligands.

Recalling that K_{com} refers to the equilibrium $\text{Ox} + \text{Red}_2 \rightleftharpoons 2\text{Red}_1$, it is apparent that in reducing the complex from $\text{Fe}(\text{Cl}_4\text{SQ})_3$, the dianion, $[\text{Fe}(\text{Cl}_4\text{Cat})_2(\text{Cl}_4\text{SQ})]^{2-}$, is the least stable redox isomer and will revert to the monoanion $[\text{Fe}(\text{Cl}_4\text{Cat})(\text{Cl}_4\text{SQ})_2]^-$ and the trianion $[\text{Fe}(\text{Cl}_4\text{Cat})_3]^{3-}$. This can even be seen in the oxidation peaks in DPV in MeOH, where the +119 mV peak has less magnitude than the other two. This is also why the ΔE_p found by Igor Pro is larger for this couple in both oxidation and reduction, as the kinetics are slower for electron transfer. This

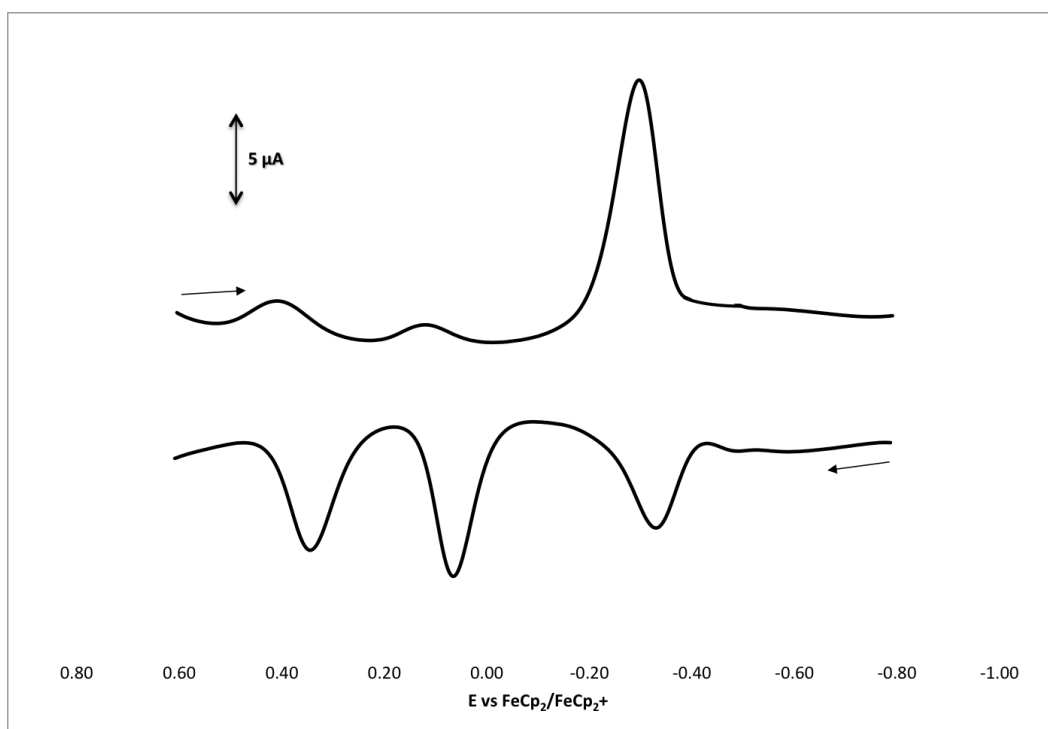


Figure 3.28: Differential pulse voltammograms of $(\text{Bu}_4\text{N})_3[\text{Fe}(\text{Cl}_4\text{Cat})_3]$ in DMSO at an effective scan rate of 20 mV/s. Pulse width = 50 ms, Pulse period = 20 ms, Step potential = 4 mV, Pulse amplitude = 50 mV.

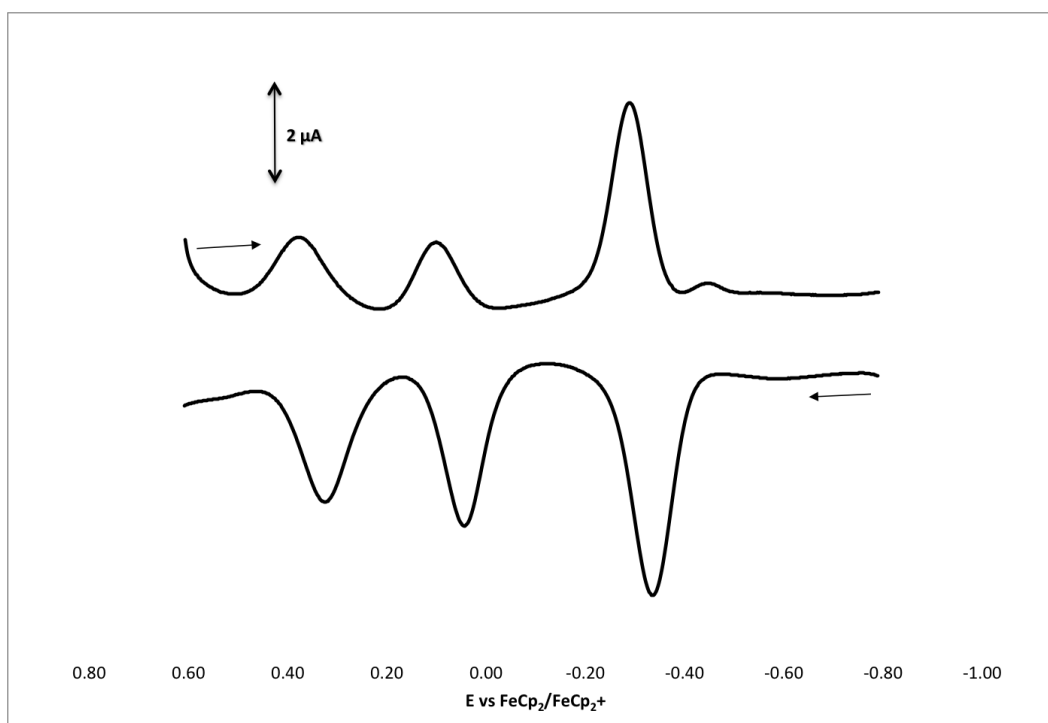


Figure 3.29: Differential pulse voltammograms of $(\text{Bu}_4\text{N})_3[\text{Fe}(\text{Cl}_4\text{Cat})_3]$ in DMSO at an effective scan rate of 3 mV/s. Pulse width = 300 ms, Pulse period = 600 ms, Step potential = 2 mV, Pulse amplitude = 50 mV.

is especially obvious in the DPV at an effective scan rate of 20 mV/s, where the reduction peak for $[\text{Fe}(\text{Cl}_4\text{Cat})(\text{Cl}_4\text{SQ})_2]^- \longrightarrow [\text{Fe}(\text{Cl}_4\text{Cat})_2(\text{Cl}_4\text{SQ})]^{2-}$ simply bleeds into the reduction peak for $[\text{Fe}(\text{Cl}_4\text{Cat})_2(\text{Cl}_4\text{SQ})]^{2-} \longrightarrow [\text{Fe}(\text{Cl}_4\text{Cat})_3]^{3-}$.

3.2.5 Cyclic Voltammetry of $[\text{Co}(\text{Cl}_4\text{Cat})_2(\text{Cl}_4\text{SQ})]^{2-}$

Cyclic voltammetry of $(\text{Pr}_4\text{N})_2[\text{Co}(\text{Cl}_4\text{Cat})_2(\text{Cl}_4\text{SQ})]$ and $(\text{Ph}_4\text{P})_2[\text{Co}(\text{Cl}_4\text{Cat})_2(\text{Cl}_4\text{SQ})]$ resulted in the same electrochemical behavior. In DMSO the cobalt complex has two closely overlapping couples, which become more distinguishable at slower scan rates, at $E_{1/2} = -247$ mV and -316 mV vs $\text{FeCp}_2/\text{FeCp}_2^+$ (Figure 3.32). Because the cobalt complex is mixed-valence as synthesized, the reduced species could be either $[\text{Co}(\text{Cl}_4\text{Cat})_2(\text{Cl}_4\text{SQ})]^{2-}$ or $[\text{Co}(\text{Cl}_4\text{Cat})_3]^{3-}$.

A scan on the same DMSO solution using a wider potential range is shown in Figure 3.33. From this it can be determined that the species present at potentials negative of -400 mV is $[\text{Co}(\text{Cl}_4\text{Cat})_3]^{3-}$, as no further reductions are observed despite going to -2091 mV. Two more irreversible oxidations at approximately 460 mV and 660 mV can be seen in both $(\text{Pr}_4\text{N})_2[\text{Co}(\text{Cl}_4\text{Cat})_2(\text{Cl}_4\text{SQ})]$ and $(\text{Ph}_4\text{P})_2[\text{Co}(\text{Cl}_4\text{Cat})_2(\text{Cl}_4\text{SQ})]$ cyclic voltammograms, which could be cleavage of carbon-chlorine bonds and/or an oxidation and dissociation of one or more ligands.

Another question is how many electrons are involved in the reversible couple/couples. In Figure 3.34, at 10 mV/s, with a 1 mM concentration of both ferrocene and $(\text{Pr}_4\text{N})_2[\text{Co}(\text{Cl}_4\text{Cat})_2(\text{Cl}_4\text{SQ})]$, the total peak height ($i_{pc} - i_{pa}$) is $15.5 \mu\text{A}$ for the cobalt complex at -247 mV, and $11.2 \mu\text{A}$ for ferrocene. The cobalt complex has a larger peak current than an equimolar amount of ferrocene, indicating that more than one electron is involved in the couple. However, it could be either two or three electrons, depending on if the complex is oxidized to $\text{Co}(\text{Cl}_4\text{SQ})_3$ or $[\text{Co}(\text{Cl}_4\text{Cat})(\text{Cl}_4\text{SQ})_2]^-$.

A more direct cyclic voltammetric comparison is the peak-to-peak separation, ΔE_p , which at 25°C is ideally $59/n$ mV.¹⁵ The ΔE_p is also used as a criteria for reversibility of a redox couple. In Figure 3.34 the ΔE_p for ferrocene is 77 mV, rather than the ideal 59 mV, but this correlates well with other sources for ferrocene in DMSO.⁶⁷ The cobalt complex, however, has two closely overlapping peaks. Determining what the ΔE_p is for each couple is complicated by the difficulty

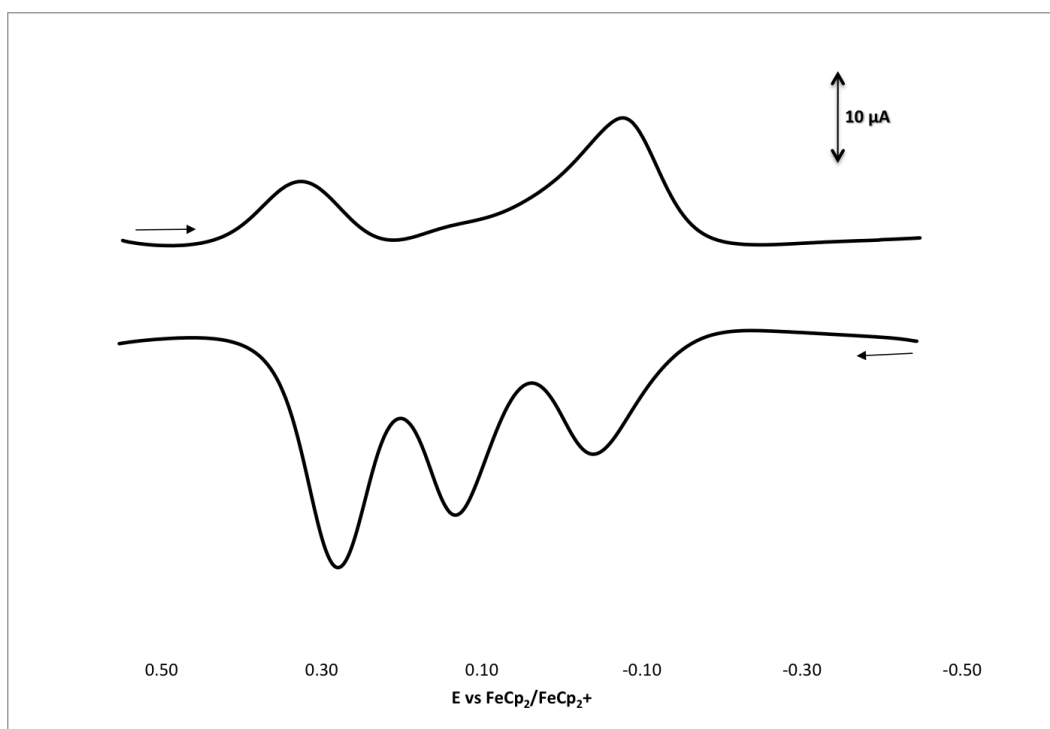


Figure 3.30: Differential pulse voltammograms of $(\text{Bu}_4\text{N})_3[\text{Fe}(\text{Cl}_4\text{Cat})_3]$ in MeOH at an effective scan rate of 20 mV/s. Pulse width = 50 ms, Pulse period = 200 ms, Step potential = 4 mV, Pulse amplitude = 50 mV.

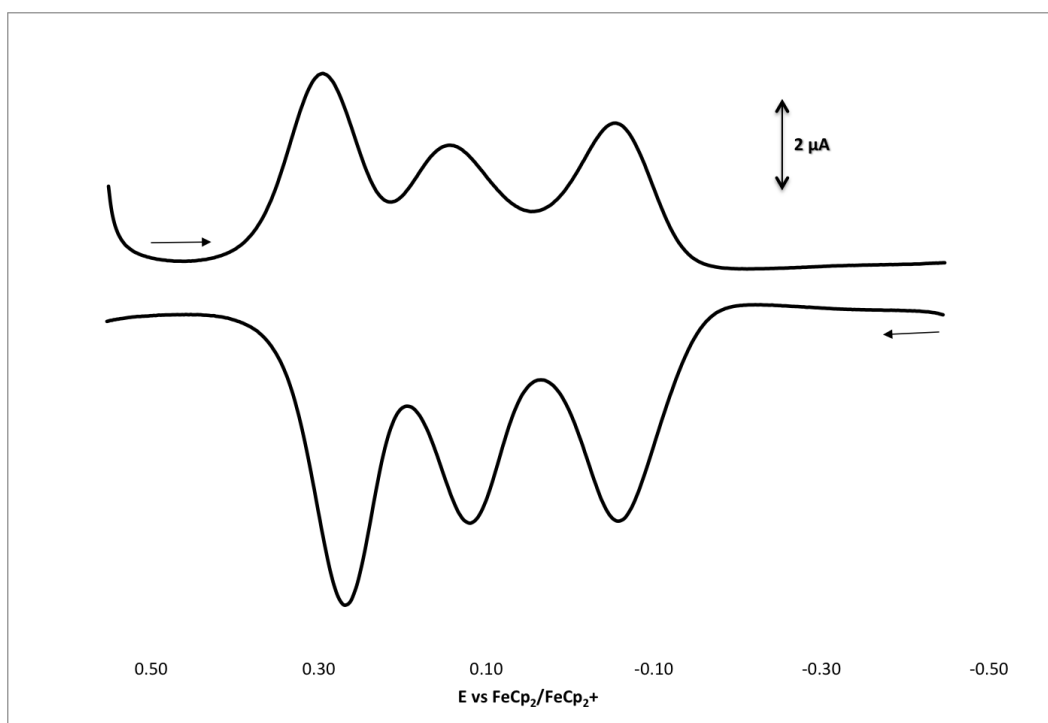


Figure 3.31: Differential pulse voltammograms of $(\text{Bu}_4\text{N})_3[\text{Fe}(\text{Cl}_4\text{Cat})_3]$ in MeOH at an effective scan rate of 20 mV/s. Pulse width = 300 ms, Pulse period = 600 ms, Step potential = 2 mV, Pulse amplitude = 25 mV.

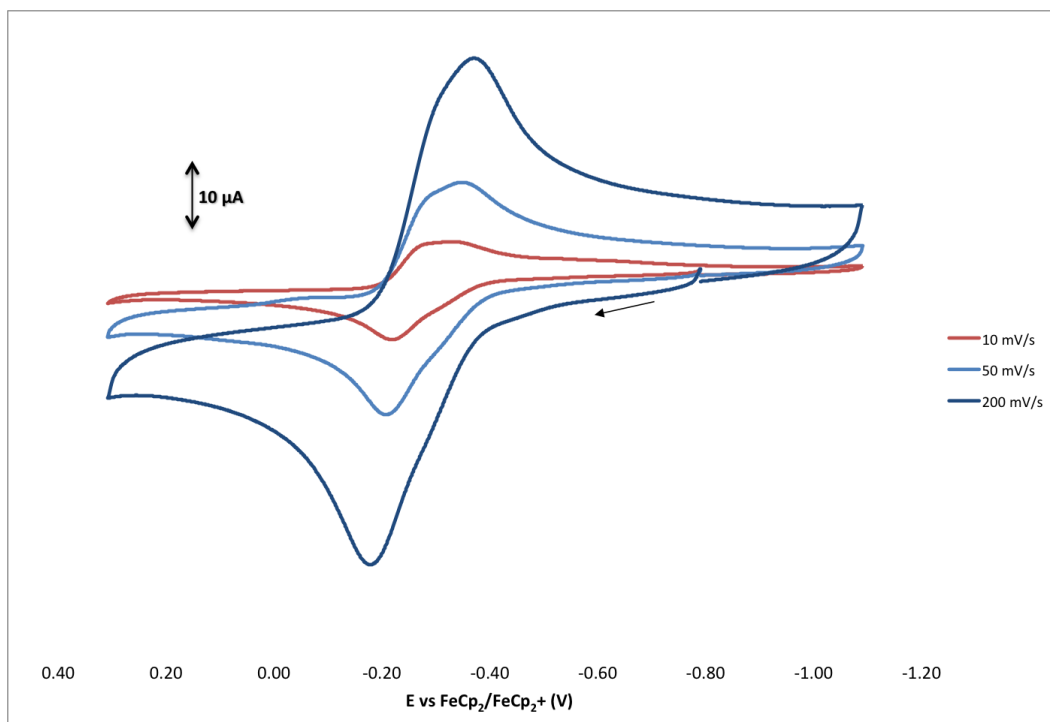


Figure 3.32: Cyclic voltammograms of 1 mM $(\text{Pr}_4\text{N})_2[\text{Co}(\text{Cl}_4\text{Cat})_2(\text{Cl}_4\text{SQ})]$ in DMSO vs $\text{FeCp}_2/\text{FeCp}_2^+$ at 10 mV/s, 50 mV/s, and 200 mV/s.

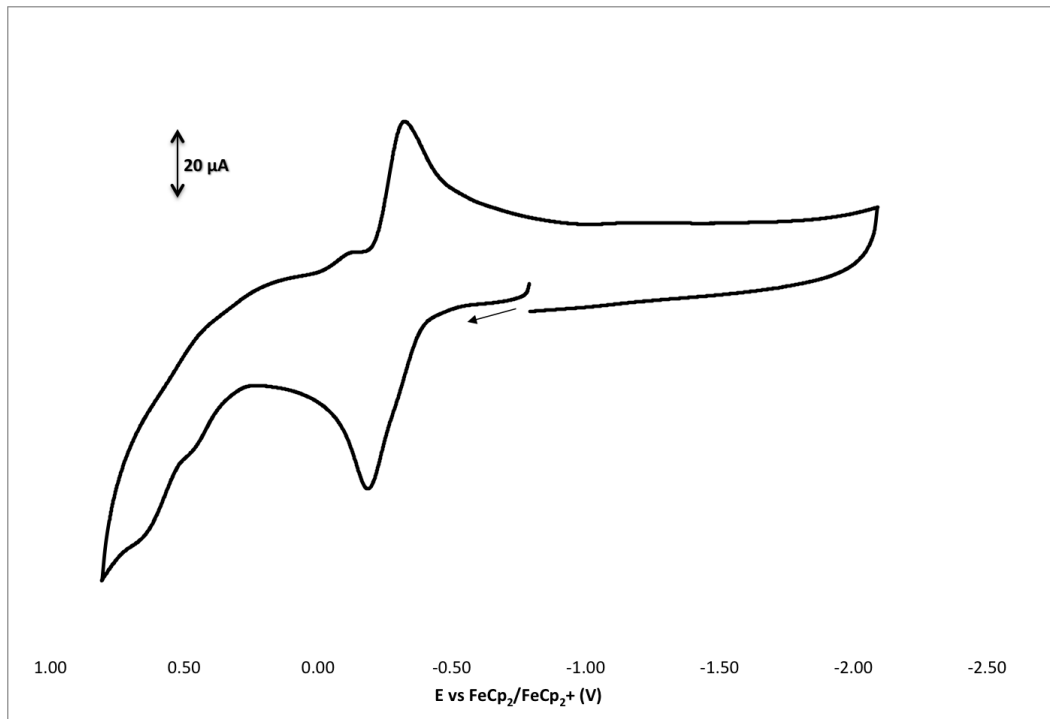


Figure 3.33: Cyclic voltammogram of 1 mM $(\text{Pr}_4\text{N})_2[\text{Co}(\text{Cl}_4\text{Cat})_2(\text{Cl}_4\text{SQ})]$ in DMSO vs $\text{FeCp}_2/\text{FeCp}_2^+$ at 200 mV/s.

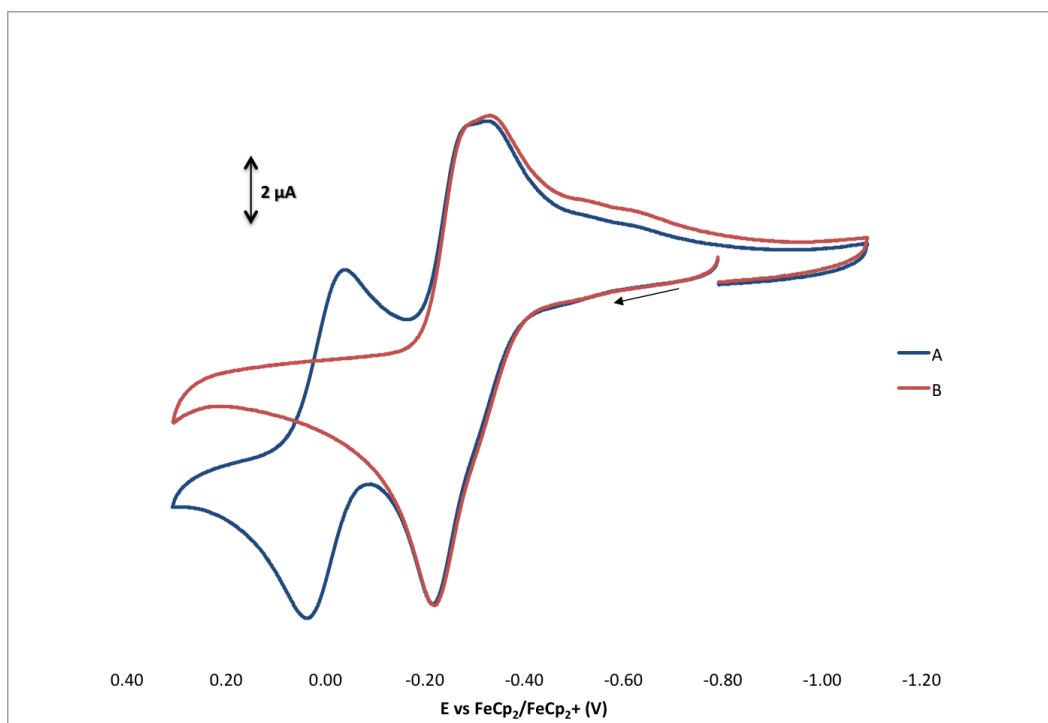


Figure 3.34: Cyclic voltammogram of (A) 1 mM $(\text{Pr}_4\text{N})_2[\text{Co}(\text{Cl}_4\text{Cat})_2(\text{Cl}_4\text{SQ})]$ with 1 mM ferrocene in DMSO and (B) 1 mM $(\text{Pr}_4\text{N})_2[\text{Co}(\text{Cl}_4\text{Cat})_2(\text{Cl}_4\text{SQ})]$ at 10 mV/s. The couple at 91 mV is $\text{FeCp}_2/\text{FeCp}_2^+$. Start/end potential -700 mV, range $+400$ mV to -1000 mV.

in picking out at what potential the forward and reverse peaks are. Estimating from the 50 mV/s cyclic voltammogram, the more positive couple has a ΔE_p of approximately 70 mV, and the more negative couple has a ΔE_p of approximately 65 mV. Comparing this to the one-electron ferrocene ΔE_p , these couples are one electron each.

The difference in $E_{1/2}$ for the cobalt complex couples also fits well with calculations by Richardson and Taube,⁸² in that the peak-to-peak difference of the most positive and most negative of the overlapping peaks (−226 mV and −323 mV, respectively, at 10 mV/s) is 97 mV, which corresponds to a difference in $E_{1/2}$ of approximately 70 mV. This is the calculated difference between the two couples (−247mV − 316mV = 69mV).

A comparison of the cyclic voltammogram of $(\text{Pr}_4\text{N})_2[\text{Co}(\text{Cl}_4\text{Cat})_2(\text{Cl}_4\text{SQ})]$ with and without ferrocene (Figure 3.34) also shows that the addition of ferrocene does not affect the cobalt complex couples. Because the ferrocene couple does not overlap with those of the cobalt complex, there is not pi-stacking interaction at the electrode surface between the cyclopentadienyl rings and the quinone rings.

The solvent effect in methanol also holds for the cobalt complex. Figure 3.35 shows a 1 mM solution of $(\text{Pr}_4\text{N})_2[\text{Co}(\text{Cl}_4\text{Cat})_2(\text{Cl}_4\text{SQ})]$ in MeOH. As with the iron and manganese analogs, the cyclic voltammogram appears compressed, which for the cobalt complex results in a reversible two-electron couple at $E_{1/2} = -133$ mV vs $\text{FeCp}_2/\text{FeCp}_2^+$ that does not resolve into separate peaks, even at slow scan rates.

Direct comparison of cyclic voltammograms of $(\text{Pr}_4\text{N})_2[\text{Co}(\text{Cl}_4\text{Cat})_2(\text{Cl}_4\text{SQ})]$ in DMSO and MeOH is shown in Figure 3.36. The potential shift to a single couple at −133 mV in MeOH from two couples at −247 mV and −316 mV in DMSO is apparent, as well as how the peak in MeOH is not split into overlapping couples, but appears as a single forward/reverse peak. The difference in current is, of course, due to differences in diffusivity in different solvents and different dielectric properties. The positive potential shift is also observed for the iron complex.

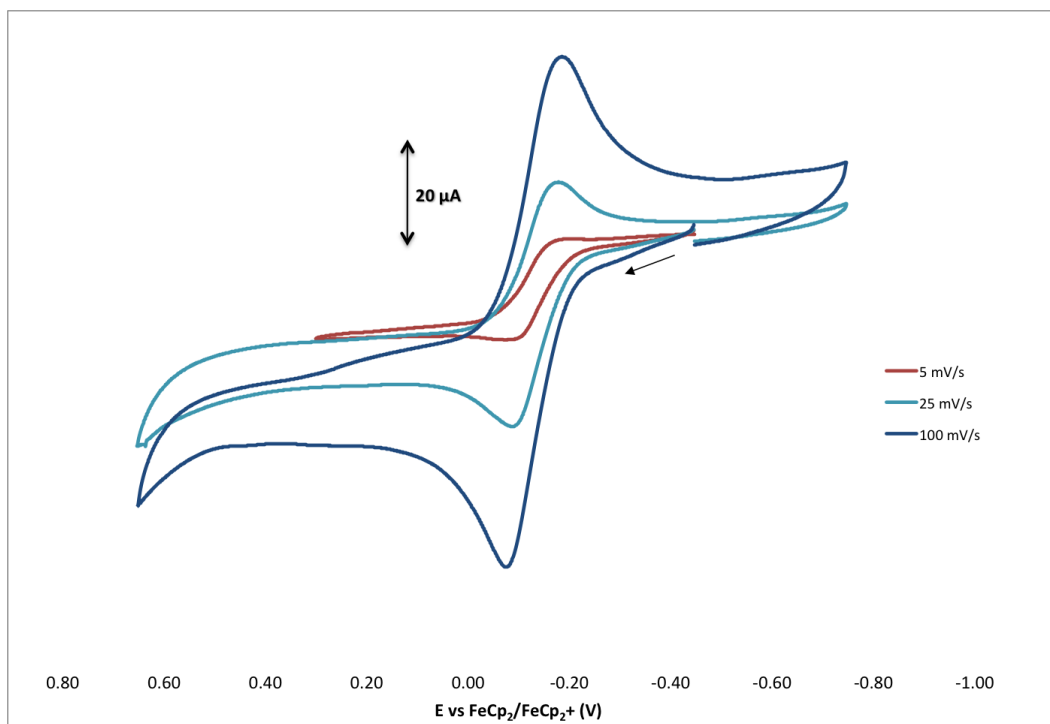


Figure 3.35: Cyclic voltammograms of 1 mM $(\text{Pr}_4\text{N})_2[\text{Co}(\text{Cl}_4\text{Cat})_2(\text{Cl}_4\text{SQ})]$ in MeOH vs $\text{FeCp}_2/\text{FeCp}_2^+$ at 5 mV/s, 25 mV/s, and 100 mV/s.

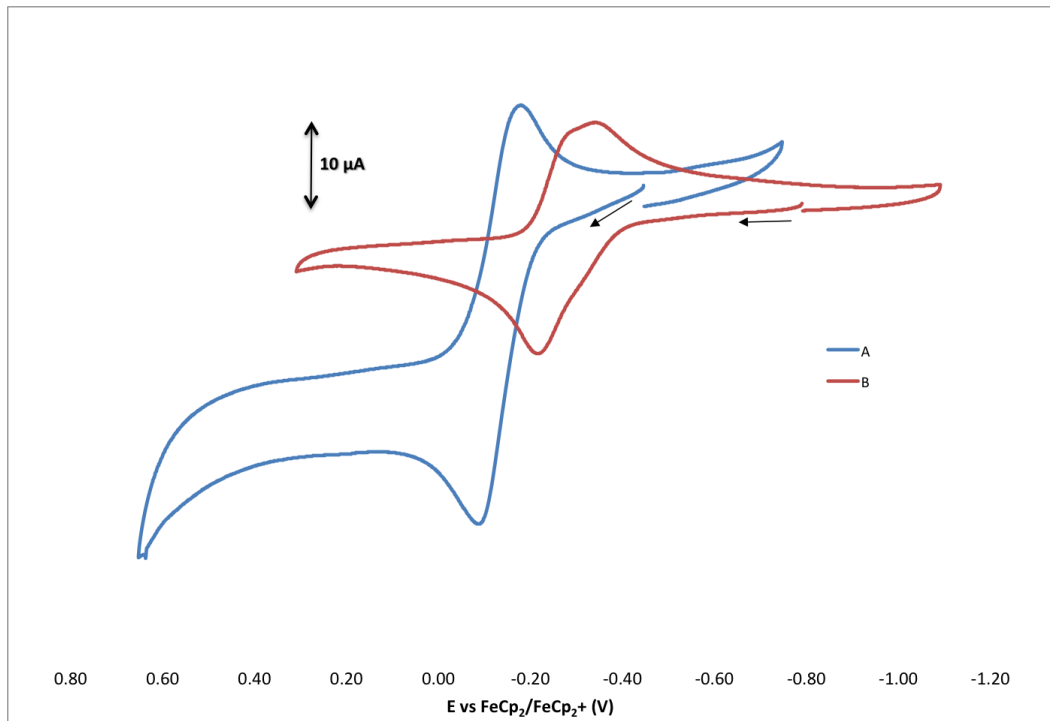


Figure 3.36: Cyclic voltammograms of 1 mM $(\text{Pr}_4\text{N})_2[\text{Co}(\text{Cl}_4\text{Cat})_2(\text{Cl}_4\text{SQ})]$ in (A) MeOH and (B) DMSO vs $\text{FeCp}_2/\text{FeCp}_2^+$ at 25 mV/s.

3.2.6 Differential Pulse Voltammetry of $[\text{Co}(\text{Cl}_4\text{Cat})_2(\text{Cl}_4\text{SQ})]^{2-}$

Figure 3.37 shows differential pulse voltammograms of $(\text{Ph}_4\text{P})_2[\text{Co}(\text{Cl}_4\text{Cat})_2(\text{Cl}_4\text{SQ})]$ in DMSO. The more positive couple has $E_{pa} = -261$ mV and $E_{pc} = -241$ mV vs $\text{FcCp}_2/\text{FcCp}_2^+$, giving a $E_{1/2}$ of -251 mV. The more negative couple appears at $E_{pa} = -331$ mV and $E_{pc} = -301$ mV, giving a $E_{1/2}$ of -316 mV. These values fit very well with the numbers from cyclic voltammetry. It is also easier to see the peak differences in anodic processes in the differential pulse voltammogram, something not clear in the cyclic voltammogram. It should be noted that adjusting the DPV parameters to clarify peak separation resulted in a voltammogram with fewer data points, so there is a larger margin of error in peak location, which is why the peak-to-peak separation is less than 50 mV.

For the cobalt complex, even with DPV, it is difficult to separate the overlapping peaks observed in DMSO. Peak fitting in Igor Pro using the Multipeak Fitting 2 package gives the two overlapping peaks $\Delta E_{p/2}$ of 106 mV and 85 mV, which correlates to two one-electron peaks. This provides yet more evidence that the cobalt complex behaves as a weakly-coupled Class II compound in DMSO, as theoretically a two-electron transfer of a true Class I complex would be a peak with $\Delta E_{p/2}$ of 45.2 mV. For ferrocene in DMSO, DPV gives a $\Delta E_{p/2}$ of about 90 mV, as expected.

These calculations combined with data from cyclic voltammetry confirm that the cobalt complex couple is a two-electron transfer, going from $[\text{Co}(\text{Cl}_4\text{Cat})_3]^{3-}$ to $[\text{Co}(\text{Cl}_4\text{Cat})(\text{Cl}_4\text{SQ})_2]^-$, and the last oxidation to a neutral complex is either not observed or irreversible. This is also supported by the lack of a synthesis for $\text{Co}(\text{Cl}_4\text{SQ})_3$, which further indicates that such a species is not stable. The difference in peak height of the two overlapping couples is most likely due to a difference in diffusion coefficient, especially considering the flattening and broadening of the $[\text{Co}(\text{Cl}_4\text{Cat})_3]^{3-} \rightleftharpoons [\text{Co}(\text{Cl}_4\text{Cat})_2(\text{Cl}_4\text{SQ})]^{2-}$ couple. A difference in diffusion coefficient would also explain why the overlapping anodic peaks are more apparent in differential pulse voltammetry than in cyclic voltammetry, as differential pulse voltammetry allows time for a diffusion layer to come to equilibrium at the electrode surface, by holding the potential constant on the order of

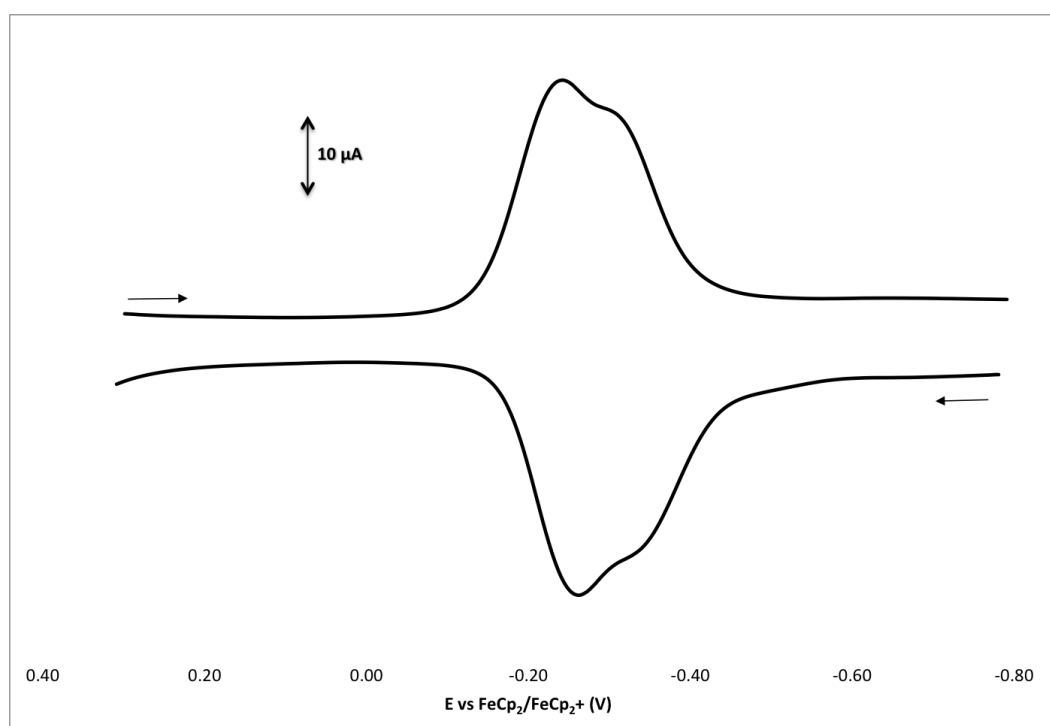


Figure 3.37: Differential pulse voltammograms of 1 mM $(\text{Ph}_4\text{P})_2[\text{Co}(\text{Cl}_4\text{Cat})_2(\text{Cl}_4\text{SQ})]$ in DMSO. Step $E = 10$ mV, Pulse amplitude = 50 mV, Pulse width = 50 ms, Pulse period = 100 ms.

milliseconds (in Figure 3.37, 50 ms, specifically). It also emphasizes the reversibility of the two couples, in that both are clearly observed to be mirrors of each other in the differential pulse voltammogram, much like the iron complex at slow scan rates.

Using the $E_{1/2}$ values from DPV for the $[\text{Co}(\text{Cl}_4\text{Cat})_3]^{3-} \rightleftharpoons [\text{Co}(\text{Cl}_4\text{Cat})_2(\text{Cl}_4\text{SQ})]^{2-}$ and $[\text{Co}(\text{Cl}_4\text{Cat})_2(\text{Cl}_4\text{SQ})]^{2-} \rightleftharpoons [\text{Co}(\text{Cl}_4\text{Cat})(\text{Cl}_4\text{SQ})_2]^-$ couples, K_{com} calculates to 13 (at 25 °C), and thus Class I by Robin and Day classification. This confirms again that the ligands of the cobalt complex are very weakly coupled, and while the EPR spectrum shows that the ligands communicate on the EPR timescale, electron transfer kinetics in DMSO are fast enough to observe overlapping couples, but slow enough to still result in Class I character.

This is also supported by DPV in MeOH (Figure 3.38). Only one cathodic or anodic peak is observed, although they are not as sharp as theoretical two-electron peaks would be, having an average ΔE_p of 125 mV. Comparing this result to DMSO, it seems that although the cobalt complex may be classified as Class I, it has enough Class II character to broaden the DPV peaks. While the solvent effect of MeOH is to increase the valence localization, there is still enough electron transfer between ligands to broaden the peaks. The $E_{1/2}$ given by DPV in MeOH is -129 mV vs $\text{FeCp}_2/\text{FeCp}_2^+$, which fits well with cyclic voltammetry.

3.2.7 Comparison of Electrochemical Behavior

Each of these first-row transition metal complex behaves in its own unique way. However, there are some clear similarities between the complexes. Figure 3.39 shows cyclic voltammograms of the iron, manganese, and cobalt complexes in DMSO at 25 mV/s. Comparing the cyclic voltammograms of all three complexes in the same solvent makes the assignment of number of electrons transferred per couple more obvious. As all three complexes are similar in mass and size, it is reasonable to assume that they have similar diffusion coefficients. Diffusion coefficients were calculated with the Randles-Sevcik equation, using the constant $i_{pf}/v^{1/2}$. Plugging in $n = 1$ for the manganese and iron complexes, and $n = 2$ for the cobalt complex, results in similar diffusion coefficients all three complexes (Table 3.8). This allows a more direct peak current comparison than

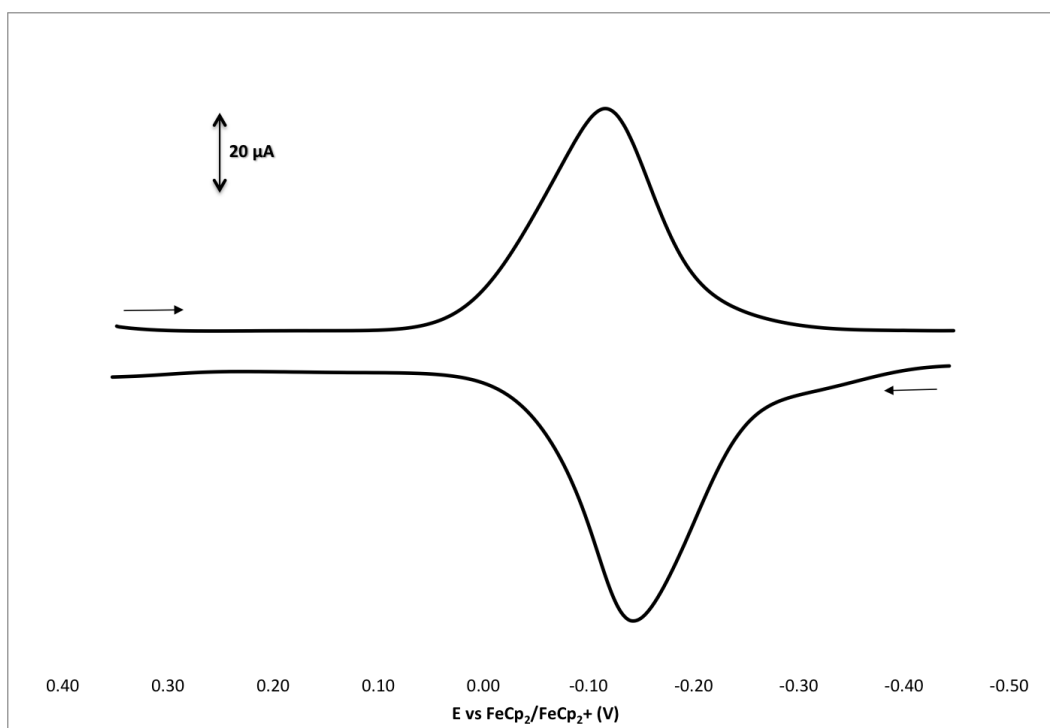


Figure 3.38: Differential pulse voltammograms of 1 mM $(\text{Pr}_4\text{N})_2[\text{Co}(\text{Cl}_4\text{Cat})_2(\text{Cl}_4\text{SQ})]$ in MeOH. Step E = 4 mV, Pulse amplitude = 50 mV, Pulse width = 50 ms, Pulse period = 200 ms.

is possible with ferrocene.

Table 3.8: Diffusion coefficients for reduced species calculated from the first oxidation peak, at 25 °C

	Diffusion Coefficient $\times 10^6$ cm ² /s
$[\text{Mn}(\text{Cl}_4\text{Cat})_3]^{2-}$	3.9
$[\text{Fe}(\text{Cl}_4\text{Cat})_3]^{3-}$	3.9
$[\text{Co}(\text{Cl}_4\text{Cat})_3]^{3-}$	3.8

The initial oxidation peak for the cobalt complex has approximately twice the current as the iron and manganese complexes, confirming previous assignment of the reversible cobalt couple as a Class I two-electron couple (i.e. two one-electron couples at nearly the same potential). This also confirms assignment of one-electron oxidations to the first and second oxidation peaks for the manganese and iron complexes, which not only fit well with their peak currents, but also with their peak potentials.

The broadness of the iron complex reduction is also more obvious when compared to the well-defined cobalt complex reduction. The manganese complex reduction is still unclear at 25 mV/s, however, when scan rates of 5 mV/s are compared (Figure 3.40) not only do the iron complex reductions become clear, but the two manganese complex reductions are seen to be one electron each. Further, considering peak potentials for the iron and manganese complex, the two oxidation peaks and two reduction peaks for the manganese analog can be assigned as $[\text{Mn}(\text{Cl}_4\text{Cat})_3]^{2-} \rightleftharpoons [\text{Mn}(\text{Cl}_4\text{Cat})_2(\text{Cl}_4\text{SQ})]^-$ and $[\text{Mn}(\text{Cl}_4\text{Cat})_2(\text{Cl}_4\text{SQ})]^- \rightleftharpoons \text{Mn}(\text{Cl}_4\text{Cat})(\text{Cl}_4\text{SQ})_2$. As previously discussed (Section 3.2.1), these couples may be subject to valence tautomerism, however, this property does not affect the number of electrons transferred.

Also noteworthy is that the initial one-electron cobalt complex oxidation peak, which is very difficult to see in the cyclic voltammogram, can, upon careful inspection, be seen as a shoulder at approximately the same peak potential as the iron and manganese complexes, further evidence that the cobalt peak is the result of two closely overlapped couples.

In methanol the complexes have similar behavior. As has been previously noted, methanol compresses the redox potential range for all three complexes by increasing the charge localization

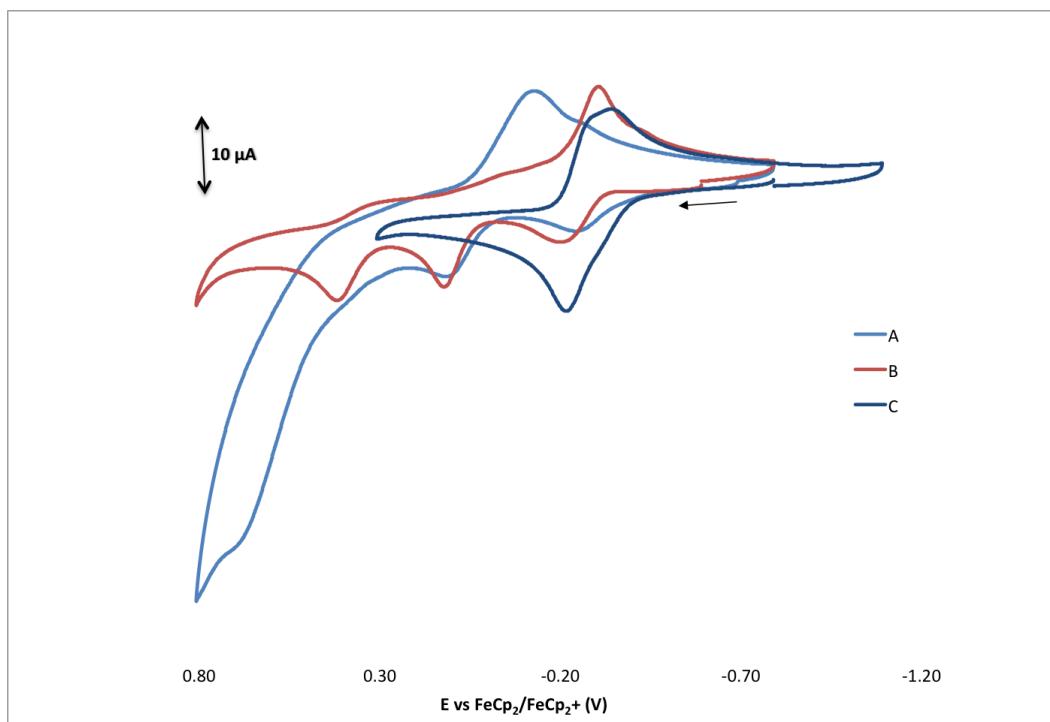


Figure 3.39: Cyclic voltammograms of 1 mM (A) $(\text{Pr}_4\text{N})_2[\text{Mn}(\text{Cl}_4\text{Cat})_3]$, (B) $(\text{Bu}_4\text{N})_3[\text{Fe}(\text{Cl}_4\text{Cat})_3]$, and (C) $(\text{Pr}_4\text{N})_2[\text{Co}(\text{Cl}_4\text{Cat})_2(\text{Cl}_4\text{SQ})]$ in DMSO at 25 mV/s.

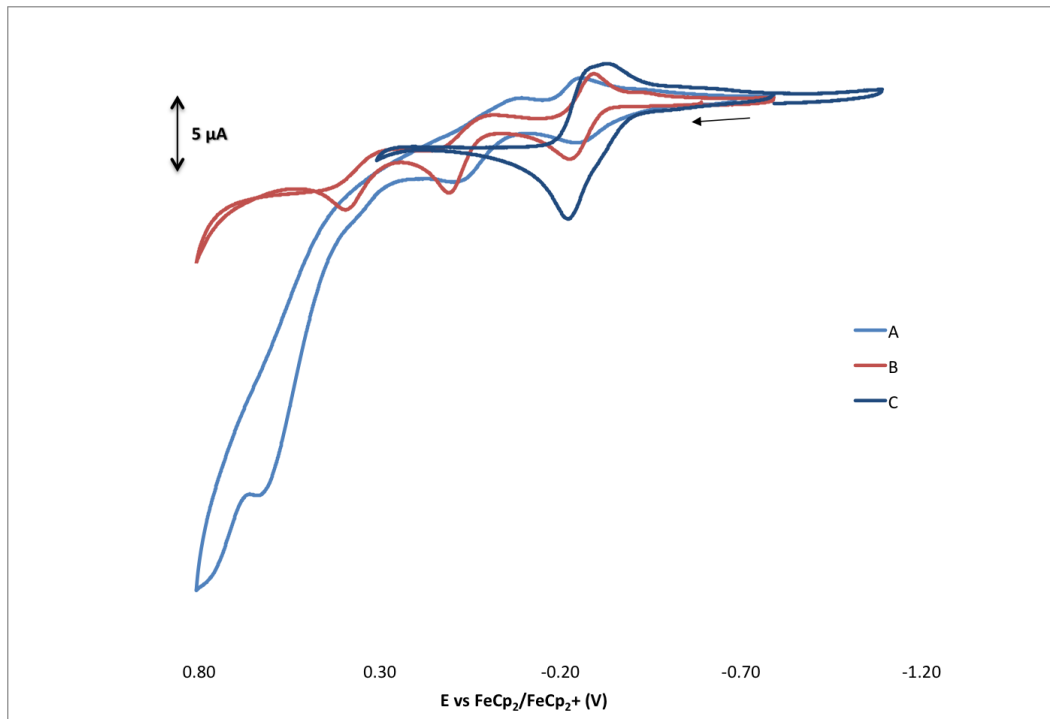


Figure 3.40: Cyclic voltammograms of 1 mM (A) $(\text{Pr}_4\text{N})_2[\text{Mn}(\text{Cl}_4\text{Cat})_3]$, (B) $(\text{Bu}_4\text{N})_3[\text{Fe}(\text{Cl}_4\text{Cat})_3]$, and (C) $(\text{Pr}_4\text{N})_2[\text{Co}(\text{Cl}_4\text{Cat})_2(\text{Cl}_4\text{SQ})]$ in DMSO at 5 mV/s.

on the ligands, making the complexes more Class I in nature. Figure 3.41 shows all three complexes in MeOH at 100 mV/s, and Figure 3.42 shows all three complexes in MeOH at 10 mV/s. Once again, the current for the cobalt complex peaks is much larger than for the corresponding iron or manganese complex peaks, further confirming that it is a two-electron transfer. The reduction peaks for all three analogs are close in potential at fast scan rates, with E_{pr} of -190 mV for manganese, -162 for iron, and -185 for cobalt. The initial iron complex oxidation ($E_{pf} = 0$ mV at 10 mV/s) is more obviously positive than the manganese or cobalt complexes (-120 mV and -89 mV, respectively).

These oxidations and reductions are still quite close in potential. Clearly, the iron complex is slightly more difficult to oxidize in methanol than the manganese or cobalt analogs, but the potentials are all still quite close to each other. The reversible manganese complex couple at approximately -150 mV is only 27 mV away from the cobalt complex couple at -133 mV. This indicates that the redox couples observed for these complexes are truly ligand-based.

Methanol also shifts the potentials more positive for all of the couples. This information, combined with the narrowing of the potential range, indicates that there is interaction between the methanol and the complexes. Methanol is a small molecule and capable of hydrogen bonding. Considering that the narrowing of the potential range means that all the complexes have more charge localization, the methanol must inhibit electron transfer through the metal center either by interaction with the chelated oxygens, or by stabilizing charge on the electronegative chlorine substituents. Conversely, DMSO is a more polar solvent that encourages electron transfer between ligands, by allowing more charge delocalization over the quinone rings. The positive potential shift of the couples in MeOH is due to interaction between the solvent and the complex, which interferes with electron transport between the complex and the electrode surface.

The difference in electrochemical behavior between the transition metals hinges upon electron transfer between ligands, and between ligands and metal. One difference between the manganese complex and the iron and cobalt analogs is that, barring the most negative couple in MeOH, the manganese does not have reversible couples. Manganese is more susceptible to ligand dissociation,

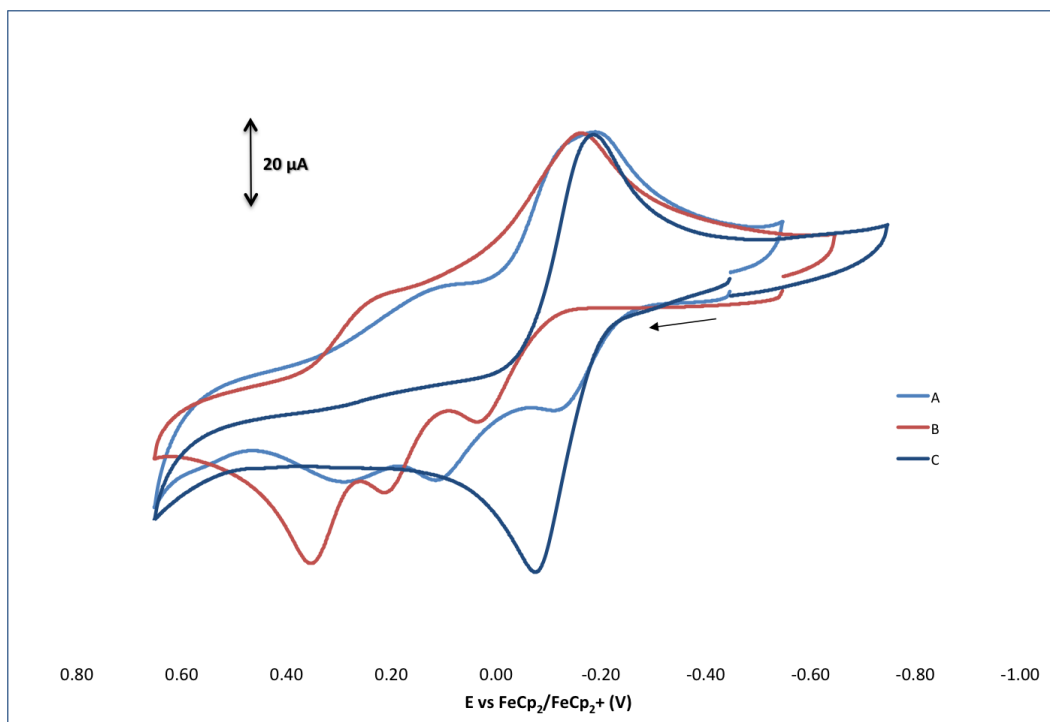


Figure 3.41: Cyclic voltammograms of 1 mM (A) $(\text{Pr}_4\text{N})_2[\text{Mn}(\text{Cl}_4\text{Cat})_3]$, (B) $(\text{Bu}_4\text{N})_3[\text{Fe}(\text{Cl}_4\text{Cat})_3]$, and (C) $(\text{Pr}_4\text{N})_2[\text{Co}(\text{Cl}_4\text{Cat})_2(\text{Cl}_4\text{SQ})]$ in MeOH at 100 mV/s.

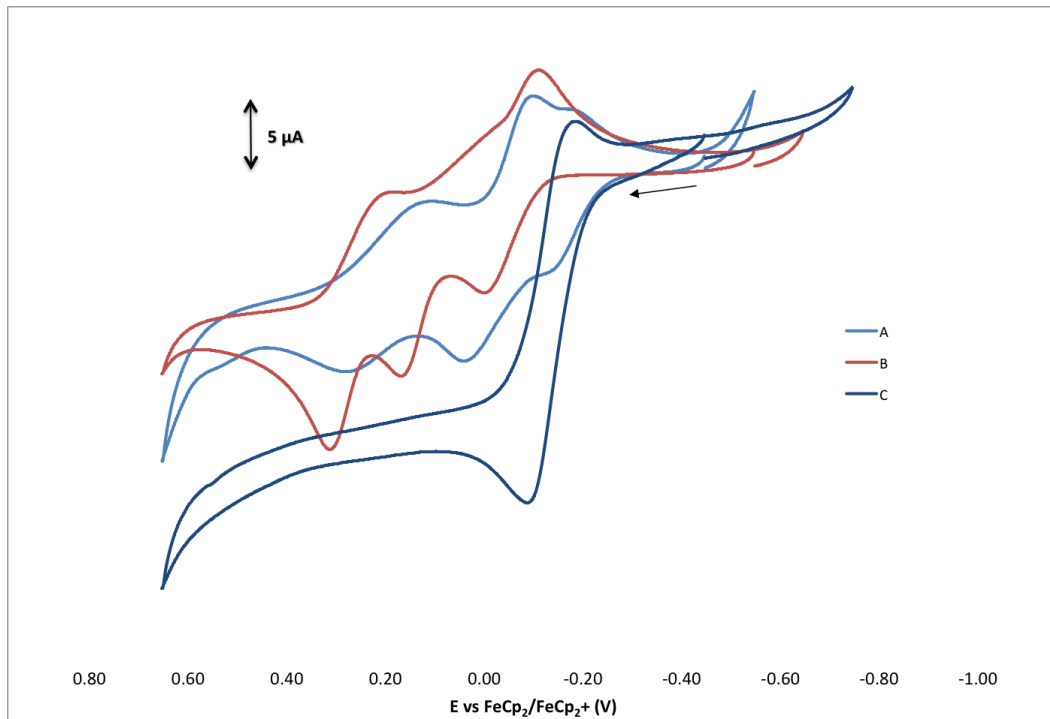


Figure 3.42: Cyclic voltammograms of 1 mM (A) $(\text{Pr}_4\text{N})_2[\text{Mn}(\text{Cl}_4\text{Cat})_3]$, (B) $(\text{Bu}_4\text{N})_3[\text{Fe}(\text{Cl}_4\text{Cat})_3]$, and (C) $(\text{Pr}_4\text{N})_2[\text{Co}(\text{Cl}_4\text{Cat})_2(\text{Cl}_4\text{SQ})]$ in MeOH at 10 mV/s.

which accounts for the irreversibility and quasireversibility of its couples. One property previously noted is valence tautomerism, which is not possible to determine with these experiments, but may contribute to quasireversibility of the manganese couples. In valence tautomerism, ligand-based orbitals and metal-based orbitals have the same energy. However, the shift between Mn^{IV} and $hs\text{-Mn}^{\text{III}}$ is accompanied by Jahn-Teller distortion. If the most oxidized form of the manganese complex has valence tautomerism between $\text{Mn}^{\text{IV}}(\text{Cl}_4\text{Cat})(\text{Cl}_4\text{SQ})_2$ and $\text{Mn}^{\text{III}}(\text{Cl}_4\text{SQ})_3$, with the latter as the more favorable isomer, this could account for the difference between reduction and oxidation kinetics.

The difference between the cobalt and iron analogs is mainly in that the cobalt has reversible couples at almost the same potential, while the iron exhibits reversible couples at scan rates less than 5 mV/s at distinct potentials. Because the iron is $hs\text{-Fe}^{\text{III}}$, and the cobalt is $ls\text{-Co}^{\text{III}}$, they have different orbital occupancies. Gordon and Fenske, in their theoretical treatment of $\text{Cr}^{\text{III}}(\text{Q})_3^{\text{n}}$ and $\text{Fe}^{\text{III}}(\text{Q})_3^{\text{n}}$ (where Q = Cat, SQ, or BQ) calculated that "the occupied [Molecular Orbitals] are considerably lower in energy for the iron complex than they are for the chromium complex."⁸³ While cyclic voltammetry of $\text{Cr}(\text{Cl}_4\text{Cat})_3^{3-}$ demonstrates that there is easier electron transfer between ligands than in the iron analog, this point can help explain the difference between the iron and cobalt complexes.

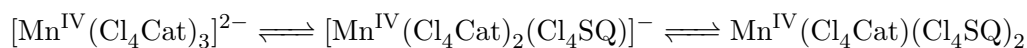
The occupied metal antibonding d-orbitals in a high spin octahedral iron complex lengthen the bond distance and inhibit electron transfer. The low spin octahedral cobalt complex, by contrast, has no electrons in the metal antibonding d-orbitals, but it is a Class I compound that has very slow electron transfer between ligands. The relative stability of the MOs explains this discrepancy. If the cobalt complex has MOs higher in energy and more ligand-based than metal-based, it would account for the Class I character. However, a theoretical treatment of tris(o-tetrachloroquinone) complexes has yet to be performed.

Chapter 4

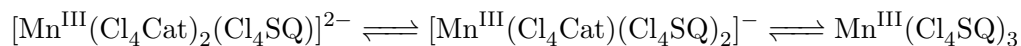
Conclusion

The synthesis and characterization of tris(tetrachloroquinone) complexes of manganese, iron, and cobalt has been presented, to complete the series of first row transition metal-tris(tetrachloroquinone) complexes. Their electrochemical properties were studied using cyclic voltammetry and differential pulse voltammetry in different solvents. In the same way that different bridging molecules have been used to investigate analogs of the mixed-valence Creutz-Taube ion, synthesizing quinone complexes using different transition metal centers was used to investigate electronic coupling between redox-active ligands. These complexes have multiple ligand-based redox couples in a narrow potential range, which is a property desirable in an electrocatalyst.

The manganese complex, tris(tetrachlorocatecholato)manganese(IV), proved difficult to characterize. It was previously synthesized by other researchers, but not characterized electrochemically. It behaves very differently in DMSO and MeOH, and may be susceptible to valence tautomerism. Experiments in cyclic voltammetry and differential pulse voltammetry indicate a three membered redox series:



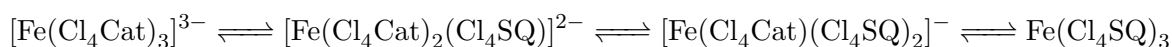
Or:



It is possible that all six redox isomers could exist, however it is not possible to determine with available technology. The manganese complex does not have reversible couples in DMSO, although

it does have two one-electron oxidations and two one-electron reductions. In MeOH, there is one reversible one-electron couple, and one quasireversible one-electron couple. There is also the possibility that a bis(tetrachloroquinone) complex was formed, especially in MeOH. Changing oxidation states of the manganese due to valence tautomerism may cause the quinone ligands to be more labile, which could account for some features of its cyclic voltammograms.

The iron complex is stable in multiple oxidation states, allowing synthesis as both neutral tris(tetrachlorosemiquinonato)iron(III) and trianion tris(tetrachlorocatecholato)iron(III) redox isomers. A four-membered redox series was characterized using spectroelectrochemistry:

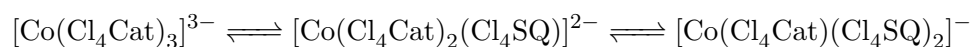


The iron complex had distinct λ_{max} shifts depending on whether a solvent was protic or aprotic, which was assigned to solvent-dependent shifts in excited states. The different redox isomers were investigated using spectroelectrochemistry, with a clear shift in λ_{max} between $[\text{Fe}(\text{Cl}_4\text{Cat})_3]^{3-}$, $[\text{Fe}(\text{Cl}_4\text{Cat})_2(\text{Cl}_4\text{SQ})]^{2-}$, and $[\text{Fe}(\text{Cl}_4\text{Cat})(\text{Cl}_4\text{SQ})_2]^{-}$. $[\text{Fe}(\text{Cl}_4\text{Cat})(\text{Cl}_4\text{SQ})_2]^{-}$ and $\text{Fe}(\text{Cl}_4\text{SQ})_3$ had very similar electronic spectra.

The iron complex has a unique electrochemical profile, with three clear one-electron oxidation peaks, but only one three-electron reduction peak in cyclic voltammograms. It is only at very slow scan rates, less than 5 mV/s, that three one-electron reduction peaks appear in the cyclic voltammogram. This property, which occurs in both DMSO and MeOH, has been clarified using differential pulse voltammetry. In DMSO, the iron complex behaves as a Class II compound (for $E_{-3/-1}$, $K_{com} = 2.97 \cdot 10^6$, and for $E_{-2/0}$, $K_{com} = 4.44 \cdot 10^4$), while in MeOH, the iron complex behaves as a Class I compound (for $E_{-3/-1}$, $K_{com} = 1.2 \cdot 10^3$, and for $E_{-2/0}$, $K_{com} = 4.5 \cdot 10^2$). The entire redox series occurs in a narrow potential window, of approximately 0.5 V. This can allow multiple electron transfer for electrochemical reactions at approximately the same potential. This makes the iron complex potentially useful as an electrocatalyst, as it can supply or accept three electrons without forming unstable intermediates. In fact, at faster scan rates, the reduction kinetics are equivalent to a three-electron peak, going from the oxidized neutral complex to the

reduced trianion complex at essentially the same potential. This could make the iron complex valuable as an electrocatalytic oxidizing agent.

The cobalt complex differs from the rest of the first-row transition metals in that it is synthesized in the mixed-valence state bis(tetrachlorocatecholato)(tetrachlorosemiquinonato)cobalt(III). In both cyclic voltammetry and differential pulse voltammetry, two one-electron couples are observed, which are very close in potential. These may be distinguished in DMSO, but appear as a single two-electron couple in MeOH. The cobalt complex does not appear to have a stable neutral redox isomer. The three-membered cobalt complex redox series is:



It is a Class I compound in both DMSO and MeOH, with very weakly coupled ligands ($K_{com} = 13$ in DMSO). In the solid state, the coupling occurs on the EPR timescale, as is shown by the lack of hyperfine splitting on the EPR spectrum. This is also supported by the very weak IVCT band in the Near-IR. As with the iron complex, having multiple couples close in potential could make the cobalt complex useful as an electrocatalyst, although it would supply or accept two electrons rather than three.

Synthetic methods for all of the complexes were similar. The iron and manganese analogs have both previously been synthesized, and a synthesis for the cobalt analog was described. Once synthesized, the catecholate complexes all showed good stability in air. The complexes are all octahedral, and various counter-ions were used to facilitate X-Ray crystallography.

The electrochemistry of these complexes is intriguing and unique. The reduction peaks of the manganese and iron analogs demonstrated a clear kinetic aspect, as the appearance of the reduction peaks changed significantly with different cyclic voltammetric scan rates. In both cases, reduction peaks appeared as one large peak at faster scan rates, which then resolved into one-electron reduction peaks at scan rates less than 5 mV/s. Even the cobalt complex, which has reversible couples, still had a kinetic aspect in the reduction peaks observed in DMSO, as scan rates of 200 mV/s appeared as one two-electron reduction, which then resolved into two one-electron

couples at slower scan rates. Experiments with ferrocene indicate that this property is possibly due to pi-stacking interactions between the species at the electrode and the bulk solution, as addition of ferrocene shifts reduction peaks when its couple overlaps with that of the complexes. This is also supported by the crystal structure of $(\text{CoCp}_2)_3[\text{Fe}(\text{Cl}_4\text{Cat})_3]$, which has the cyclopentadienyl rings of the cobaltocenium stacked on the tetrachlorocatecholate rings.

In methanol, all of the complexes had a narrower potential range for their redox couples, i.e. they had increased valence localization. This could be due to hydrogen bonding at the chelated oxygens, or some stabilization of the charge on the electronegative chlorines. Methanol is also an unavoidably wet solvent, so water may also have played a part in the electrochemistry.

These complexes have unique, ligand-based redox properties that have not been observed in other transition metal complexes. They behave differently than traditional mixed-valence compounds, whose redox active centers are metals bridged by nonmetal molecules. Ligand-based redox chemistry also avoids the constraints of oxidative addition and reductive elimination at the metal center, which opens up other possible reactive pathways. The iron and cobalt complexes both exhibit reversible electron couples in a narrow potential range, with a total of three and two electrons transferred, respectively. This makes them candidates for further investigation as electrocatalysts.

Bibliography

- ¹ Japp, F. R.; Turner, A. E. Journal of the Chemical Society, Transactions **1890**, 57, 4.
- ² Pierpont, C. G.; Buchanan, R. M. Coordination Chemistry Reviews **1981**, 38, 45 – 87.
- ³ Kaim, W.; Schwederski, B. Coordination Chemistry Reviews **2010**, 254, 1580–1588.
- ⁴ Jørgensen, C. K. Coordination Chemistry Reviews **1966**, 1, 164–178.
- ⁵ Creutz, C.; Taube, H. Journal of the American Chemical Society **1969**, 91, 3988–3989.
- ⁶ Robin, M. B.; Day, P.; Emeléus, H.; Sharpe, A., Eds.; Advances in Inorganic Chemistry and Radiochemistry, Vol. 10; Academic Press, 1968; pp 247 – 422.
- ⁷ Creutz, C. In Progress in Inorganic Chemistry; Lippard, S. J., Ed.; John Wiley & Sons, Inc., 1983; pp 1–73.
- ⁸ Brown, D. B. Mixed Valence Compounds; Springer, 1980.
- ⁹ Day, P.; Hush, N. S.; Clark, R. J. H. Philosophical Transactions of the Royal Society A: Mathematical, Physical and Engineering Sciences **2008**, 366, 5–14; PMID: 17827130.
- ¹⁰ Brunshwig, B. S.; Creutz, C.; Sutin, N. Chemical Society Reviews **2002**, 31, 168–184.
- ¹¹ Hush, N. S. Coordination Chemistry Reviews **1985**, 64, 135–157.
- ¹² Hush, N. S. In Progress in Inorganic Chemistry; Cotton, F. A., Ed.; John Wiley & Sons, Inc., 1967; pp 391–444.
- ¹³ D'Alessandro, D. M.; Keene, F. R. Chemical Society Reviews **2006**, 35, 424–440.
- ¹⁴ Kubiak, C. P. Inorganic Chemistry **2013**, 52, 5663–5676.
- ¹⁵ Zanello, P. Inorganic Electrochemistry: Theory, Practice, and Application, 1st ed.; Royal Society of Chemistry, 2003.
- ¹⁶ Zanello, P.; Opromolla, G.; Herberhold, M.; Brendel, H.-D. Journal of Organometallic Chemistry **1994**, 484, 67–70.
- ¹⁷ Attia; Pierpont, C. G. Inorganic Chemistry **1998**, 37, 3051–3056.
- ¹⁸ Attia; Pierpont, C. G. Inorganic Chemistry **1997**, 36, 6184–6187.

- ¹⁹ Attia, A. S.; Junga, O.-S.; Pierpont, C. G. Inorganica Chimica Acta **1994**, 226, 91 – 98.
- ²⁰ Attia, A. S.; Pierpont, C. G. Inorganic Chemistry **1995**, 34, 1172–1179.
- ²¹ Pierpont, C. G. Coordination Chemistry Reviews **2001**, 216-217, 99–125.
- ²² Shaikh, N.; Goswami, S.; Panja, A.; Wang, X.-Y.; Gao, S.; Butcher, R. J.; Banerjee, P. Inorganic Chemistry **2004**, 43, 5908–5918.
- ²³ Shiren, K.; Tanaka, K. Inorganic Chemistry **2002**, 41, 5912–5919.
- ²⁴ Jung, O.-S.; Pierpont, C. G. Inorganic Chemistry **1994**, 33, 2227–2235.
- ²⁵ Cass, M. E.; Gordon, N. R.; Pierpont, C. G. Inorganic Chemistry **1986**, 25, 3962–3967.
- ²⁶ Milsmann, C.; Levina, A.; Harris, H. H.; Foran, G. J.; Turner, P.; Lay, P. A. Inorganic Chemistry **2006**, 45, 4743–4754.
- ²⁷ Dei, A.; Sorace, L. Applied Magnetic Resonance **2010**, 38, 139–153.
- ²⁸ Simpson, C. L.; Pierpont, C. G. Inorganic Chemistry **1992**, 31, 4308–4313.
- ²⁹ Bianchini, C.; Masi, D.; Mealli, C.; Meli, A.; Martini, G.; Laschi, F.; Zanello, P. Inorganic Chemistry **1987**, 26, 3683–3693.
- ³⁰ Raymond, K. N.; Isied, S. S.; Brown, L. D.; Fronczek, F. R.; Nibert, J. H. Journal of the American Chemical Society **1976**, 98, 1767–1774.
- ³¹ Pierpont, C. G.; Downs, H. H. Journal of the American Chemical Society **1976**, 98, 4834–4838.
- ³² Ruiz, R.; Caneschi, A.; Gatteschi, D.; Sangregorio, C.; Sorace, L.; Vázquez, M. Inorganic Chemistry Communications **2000**, 3, 76 – 79.
- ³³ Hartman, J. R.; Foxman, B. M.; Cooper, S. R. Inorganic Chemistry **1984**, 23, 1381–1387.
- ³⁴ Zanello, P.; Corsini, M. Coordination Chemistry Reviews **2006**, 250, 2000–2022.
- ³⁵ Lynch, M. W.; Hendrickson, D. N.; Fitzgerald, B. J.; Pierpont, C. G. Journal of the American Chemical Society **1984**, 106, 2041–2049.
- ³⁶ Kessel, S. L.; Emberson, R. M.; Debrunner, P. G.; Hendrickson, D. N. Inorganic Chemistry **1980**, 19, 1170–1178.
- ³⁷ Carugo, O.; Castellani, C. B.; Djinovic, K.; Rizzi, M. Journal of the Chemical Society, Dalton Transactions **1992**, 837.
- ³⁸ Sheriff, T. S.; Carr, P.; Piggott, B. Inorganica Chimica Acta **2003**, 348, 115 – 122.
- ³⁹ Koikawa, M.; Ōkawa, H.; Kida, S. Journal of the Chemical Society, Dalton Transactions **1988**, 641–645.
- ⁴⁰ Reynolds, R. A.; Coucouvanis, D. Inorganic Chemistry **1998**, 37, 170–171.
- ⁴¹ Pierpont, C. G.; Downs, H. H.; Rukavina, T. G. Journal of the American Chemical Society **1974**, 96, 5573–5574.

- ⁴² Chang, H.-C.; Miyasaka, H.; Kitagawa, S. Inorganic Chemistry **2001**, 40, 146–156.
- ⁴³ Buchanan, R. M.; Kessel, S. L.; Downs, H. H.; Pierpont, C. G.; Hendrickson, D. N. Journal of the American Chemical Society **1978**, 100, 7894–7900.
- ⁴⁴ Chin, D. H.; Sawyer, D. T.; Schaefer, W. P.; Simmons, C. J. Inorganic Chemistry **1983**, 22, 752–758.
- ⁴⁵ Sofen, S. R.; Ware, D. C.; Cooper, S. R.; Raymond, K. N. Inorganic Chemistry **1979**, 18, 234–239.
- ⁴⁶ Sheriff, T. S.; Carr, P.; Coles, S. J.; Hursthouse, M. B.; Lesin, J.; Light, M. E. Inorganica Chimica Acta **2004**, 357, 2494 – 2502.
- ⁴⁷ Buchanan, R. M.; Claffin, J.; Pierpont, C. G. Inorganic Chemistry **1983**, 22, 2552–2556.
- ⁴⁸ Wicklund, P. A.; Brown, D. G. Inorganic Chemistry **1976**, 15, 396–400.
- ⁴⁹ Ren, T. Inorganica Chimica Acta **1995**, 229, 195–202.
- ⁵⁰ Verani, C. N.; Gallert, S.; Bill, E.; Weyhermüller, T.; Wieghardt, K.; Chaudhuri, P. Chemical Communications **1999**, 1747–1748.
- ⁵¹ Sheriff, T. S.; Watkinson, M.; Motevalli, M.; Lesin, J. F. Dalton Transactions **2010**, 39, 53.
- ⁵² Pierpont, C. G. Coordination Chemistry Reviews **2001**, 219-221, 415–433.
- ⁵³ Rohrscheid, F.; Balch, A. L.; Holm, R. H. Inorganic Chemistry **1966**, 5, 1542–1551.
- ⁵⁴ Patai, S. The Chemistry of the Quinoid Compounds; Wiley, 1974.
- ⁵⁵ Zhu, X.-Q.; Wang, C.-H. The Journal of Organic Chemistry **2010**, 75, 5037–5047.
- ⁵⁶ Jones, S. E.; Chin, D. H.; Sawyer, D. T. Inorganic Chemistry **1981**, 20, 4257–4262.
- ⁵⁷ Pierpont, C. G.; Lange, C. W. In Progress in Inorganic Chemistry; Karlin, K. D., Ed.; John Wiley & Sons, Inc., 2007; pp 331–442.
- ⁵⁸ Downs, H. H.; Buchanan, R. M.; Pierpont, C. G. Inorganic Chemistry **1979**, 18, 1736–1740.
- ⁵⁹ Pierpont, C. G. Inorganic Chemistry **2011**, 50, 9766–9772.
- ⁶⁰ Chang, H.-C.; Mochizuki, K.; Kitagawa, S. Inorganic Chemistry **2002**, 41, 4444–4452.
- ⁶¹ Chang, H.-C.; Ishii, T.; Kondo, M.; Kitagawa, S. Journal of the Chemical Society, Dalton Transactions **1999**, 2467–2476.
- ⁶² Chang, H.-C.; Susumukitagawa Molecular Crystals and Liquid Crystals **2002**, 376, 275–282.
- ⁶³ Gordon, D. J.; Fenske, R. F. Inorganic Chemistry **1982**, 21, 2907–2915.
- ⁶⁴ Caneschi, A.; Dei, A.; Gatteschi, D. Journal of the Chemical Society, Chemical Communications **1992**, 630.
- ⁶⁵ DellAmico, D. B.; Calderazzo, F.; Giurlani, U.; Pelizzi, G. Chemische Berichte **1987**, 120, 955–964.

- ⁶⁶ Bard, A.; Faulkner, L. Electrochemical Methods: Fundamentals and Applications, 2nd ed.; Wiley, 2000.
- ⁶⁷ Tsierkezos, N. G. Journal of Solution Chemistry **2007**, 36, 289–302.
- ⁶⁸ Bott, A. W.; D, P.; Practical Problems in Voltammetry: 4. Preparation of Working Electrodes; Tech. Rep.; CiteSeerX; 2008. <http://citeseerx.ist.psu.edu/viewdoc/summary?doi=10.1.1.123.997>.
- ⁶⁹ Bain, G. A.; Berry, J. F. Journal of Chemical Education **2008**, 85, 532.
- ⁷⁰ Trautwein, A. X.; Bill, E.; Bominaar, E. L.; Winkler, H. In Bioinorganic Chemistry; Structure and Bonding; Springer Berlin Heidelberg, 1991; pp 1–95.
- ⁷¹ Renner, G.; Hopfer, C. Chemosphere **1982**, 11, 363 – 366.
- ⁷² Remberger, M.; Hynning, P.-Å.; Neilson, A. Ecotoxicology and Environmental Safety **1991**, 22, 320 – 336.
- ⁷³ Braddon, S.; Dence, C. Tappi **1968**, 51, 249–256.
- ⁷⁴ Live, D. H.; Chan, S. I. Analytical Chemistry **1970**, 42, 791–792.
- ⁷⁵ Buysser, K. D.; Herman, G.; Bruneel, E.; Hoste, S.; Driessche, I. V. Chemical Physics **2005**, 315, 286 – 292.
- ⁷⁶ Buchanan, R. M.; Downs, H. H.; Shorthill, W. B.; Pierpont, C. G.; Kessel, S. L.; Hendrickson, D. N. Journal of the American Chemical Society **1978**, 100, 4318–4320.
- ⁷⁷ Cohn, M. J.; Xie, C. L.; Tuchagues, J. P. M.; Pierpont, C. G.; Hendrickson, D. N. Inorganic Chemistry **1992**, 31, 5028–5033.
- ⁷⁸ Karpishin, T. B.; Gebhard, M. S.; Solomon, E. I.; Raymond, K. N. Journal of the American Chemical Society **1991**, 113, 2977–2984.
- ⁷⁹ Graf, M.; Wolmershäuser, G.; Kelm, H.; Demeschko, S.; Meyer, F.; Krüger, H.-J. Angewandte Chemie International Edition **2010**, 49, 950–953.
- ⁸⁰ Kohlrausch, F. Ramanspektren: mit 146 figuren im text; Akademische verlagsgesellschaft Becker & Erler kom.-ges: Leipzig, 1943.
- ⁸¹ Jahn, H. A.; Teller, E. Proceedings of the Royal Society of London. Series A - Mathematical and Physical Sciences **1937**, 161, 220–235.
- ⁸² Richardson, D. E.; Taube, H. Inorganic Chemistry **1981**, 20, 1278–1285.
- ⁸³ Gordon, D. J.; Fenske, R. F. Inorganic Chemistry **1982**, 21, 2916–2923.